Observations and modeling of the impacts of ocean currents on surface waves with an emphasis on near-inertial currents

James Stadler

A dissertation
submitted in partial fulfillment of the
requirements for the degree of

Doctor of Philosophy

University of Washington

2026

Reading Committee:

Barry Ma, Chair

James Girton, Chair

Christie Hegermiller

Program Authorized to Offer Degree:
Oceanography

University of Washington

Abstract

Observations and modeling of the impacts of ocean currents on surface waves with an emphasis on near-inertial currents

James Stadler

Co-Chairs of the Supervisory Committee:
Barry Ma
UW Applied Physics Laboratory

James Girton
UW Applied Physics Laboratory

Surface gravity waves play an important role in mediating the exchange of momentum, heat, and gases between the ocean and the atmosphere. While surface wave properties in the open ocean are predominantly determined by atmospheric winds, surface currents have been shown to play a role in modifying surface wave properties. In the past few decades significant progress has been made towards a more complete understanding of the mechanisms and impacts of how surface currents modify surface waves, both through both observational and numerical modeling approaches. In certain conditions, currents have been found to play a significant role in modifying wave heights and wave slopes, however most of this analysis has been limited to considering tidal and steady currents, with little attention focused on how currents varying at the inertial frequency modify waves. This study is focused on addressing some of the gaps in understanding surrounding how inertial currents modify surface waves; expanding observational tools that could be used to study these processes, interrogating modeling experiments to investigate how these currents might modify waves, and analyzing observational records to see how these effects manifest in the real ocean. This work is structured in three primary chapters, focused on observational method development, idealized modeling, and observational analysis, respectively.

The first research chapter of this dissertation (Chapter 2) evaluates the ability of EM-

APEX profiling floats, instruments long used to measure ocean current profiles, to measure 1D surface wave spectra and bulk wave properties. A recently developed algorithm to measure surface waves from 1Hz measurements of ocean current variability by EM-APEX floats is applied to a deployment of 6 EM-APEX floats and compared against simultaneous measurements by two other wave measuring platforms deployed nearby. This work finds that measurements of both bulk wave properties and wave spectra by EM-APEX floats are in good agreement with measurements from more established wave measuring platforms, and that these floats are capable of measuring wave spectra over a range of swell to wind-wave frequencies, potentially making them a useful tool in future wave-current interaction studies.

The second research chapter of this dissertation (Chapter 3) targets improving understanding of how the time varying component of near-inertial currents impacts surface waves through a series of idealized models. This work demonstrates how the relationship between the spatial structure of inertial currents, the local inertial period, and wave group speeds plays a significant role in determining how inertial currents modify waves. By comparing the impacts on surface waves between simulations with currents varying inertially and steady currents with the same geometry, this work demonstrates that inertial currents can result in notably different patterns of spatial and temporal wave variability than steady currents.

Finally, the third research chapter (Chapter 4) investigates how near-inertial current impacts on surface waves manifest in historical observations from two locations in the North Pacific. By analyzing frequency spectra from time series of winds, waves and currents at these locations, this work demonstrates that inertial currents play an important role in modifying both significant wave heights and wave slopes. Additionally, this work demonstrates that the relationships between inertial currents and the modification of wave properties differs from what would be expected for steady currents, in a manner that is qualitatively consistent with the result from Chapter 3.

TABLE OF CONTENTS

LIST OF FIGURES

Figure Number Page

LIST OF TABLES

ACKNOWLEDGMENTS

The research in this work was funded by ONR awards #N00014-19-1-2626 and #N00014-24-1-2368 and supported by program manager Dr Bob Headrick. Additional support was provided by the UW Program on Climate Change (PCC) Graubard Fellowship, and UW Oceanography fellowships. Additionally, this work would not have been possible without the support of my advisors, Barry Ma and James Girton, encouraging and supporting me across numerous years of uncertain research directions. I would also like to thank my committee members, Christie Hegermilller, Eric D'Asaro, Mark Warner, and Steve Riser, for discussions that have provided necessary advice and encouragement along the way. Additional helpful feedback on interpreting the modeling results in Chapter 3 was provided by Dr. Han Wang. Finally I would like to thank my wife Amelia, my family, and my friends for providing crucial support and community throughout this journey.

Chapter 1
INTRODUCTION

1.1 Background

Waves are one of the most familiar features of the Earth's oceans and perhaps the most visible characteristic of the boundary between ocean, land, and atmosphere. Waves are of primary importance to human interactions with the ocean, impacting the safety and efficiency of economic and recreational activities that interface with the ocean. In addition, ocean waves play a significant role in the physics of the ocean surface boundary layer. Surface waves dominate the transfer of kinetic energy between the atmosphere and the ocean; of the 64TW of energy flux into the ocean from the atmosphere, approximately 60 TW are input into ocean surface waves (Wang and Huang, 2004). Most of this energy does not escape the wave-boundary layer and is dissipated locally in the upper few meters of the ocean through wave breaking and likely does not play a significant role in the general circulation of the ocean (Wunsch, 2004; Rascle et al., 2008).

While most surface wave energy may not escape the upper few meters of the ocean, there are numerous mechanisms through which surface waves significantly impact the makeup of subsurface ocean properties. Surface waves and the ocean sea-state play an important role in determining exchange of heat, momentum, and gasses at the sea surface. Surface waves modify the surface stress exerted by the wind, impacting the efficiency of momentum transfer from the winds to the ocean and the generation of wind driven currents (Janssen, 1989; Drennan et al., 2003; Ardhuin et al., 2004; Liu et al., 2017).

Additionally, waves induce a drift velocity near the surface of the ocean, known as the Stokes drift. This Stokes drift plays an important role in setting up cells of turbulent mixing, known as Langmuir turbulence, which can energize ocean mixing that extends deeper than the wave-boundary layer (Pollard and Thomas, 1989; Weller and Price, 1988; Polton and Belcher, 2007). While the implications and importance of Langmuir turbulence in the global ocean is still an area of active study, both observational and modeling analyses continue to demonstrate that surface waves play an important role in determining the depth of the ocean mixed layer, and therefore the vertical distribution of both energy and nutrients in the ocean (D'Asaro et al., 2014; Li et al., 2019; Zheng et al., 2025). Stokes drift and the near-surface mass transport driven by surface waves also has impacts on larger scale oceanic motions (Sullivan and McWilliams, 2010; Villas Bôas and Pizzo, 2021; Van Sebille et al., 2020). From changing the drift trajectories of near surface particles to influencing the force-balances of submesoscale fronts, these impacts have largely been investigated through theoretical and numerical studies due to the difficulty of studying these impacts observationally (Mcwilliams and Restrepo, 1999; Suzuki and Fox-Kemper, 2016; McWilliams and Fox-Kemper, 2013; Wagner et al., 2021).

Waves thus play an important role in the physics of the upper ocean. This dissertation seeks to contribute to better understanding what determines wave properties, specifically the role that near-inertial surface currents play in modifying wave properties. The next two sections outline the necessary background on current impacts on waves, and inertial currents in the global ocean, before the goals and outline of this study are provided.

1.2 Wave-Current Interactions Preliminaries

This section introduces some terminology and a mathematical framework for representing surface waves that will be used throughout the rest of this dissertation. Since the elevation of the sea-surface is a random, stochastic process, observing waves and the ocean sea-state is generally done in a statistical manner. This can be achieved either by characterizing the wave-field in terms of a few parameters that represent some feature of the surface waves, or by characterizing the random motion of the sea-surface in terms of a sum of a large (or infinite) number of harmonic waves (Phillips, 1966; Holthuijsen, 2007):

$$\eta(t) = \sum_{i=1}^{N} a_i \cos(2\pi f_i t + \alpha_i) \tag{1.1}$$

for some set of frequencies $f_1 \to f_n$. The amplitudes a_i and α_i are not unique, and so this sum is represented in terms of a variance density spectrum, where the variance density for a given frequency band is determined by the coefficients a_i:

$$E(f_i) = \frac{1}{\Delta f_i}\left[\overline{\eta_i^2}\right] = \frac{1}{\Delta f_i}\left[\overline{\frac{1}{2}a_i^2}\right] \tag{1.2}$$

In practice, $E(f)$ is found by taking a Fast Fourier Transform (FFT) of the timeseries of surface elevation $\eta(t)$. This can then be extended into a two dimensional directional spectrum $E(f, \theta)$, where

$$E(f) = \int_0^{2\pi} E(f, \theta) d\theta \tag{1.3}$$

From the wave spectrum, various bulk properties of the waves can then be calculated and used to characterize some aspect of the waves with a single parameter. For example, the significant wave height, Hs, a common measure used to characterize the height of waves (Munk, 1944), can be defined as:

$$Hs = 4\sqrt{\int E(f)df} \tag{1.4}$$

and wave-steepness is often characterized in terms of the mean-squared slope (mss) (Davis et al., 2023):

$$mss = \int \frac{(2\pi f)^4 E(f)}{g^2} df \tag{1.5}$$

Many other additional parameters are commonly derived from the wave spectra $E(f, \theta)$ to characterize surface waves, such as average wave period and average wave direction. Hs and mss are the two parameters used most throughout this work, so the definitions of others will not be reproduced here.

Linear wave theory has long been found to be a useful model for describing surface gravity waves (Kundu and Cohen, 2008; Phillips, 1966; Holthuijsen, 2007). In this theory, waves are modeled as a propagating harmonic wave of the form:

$$\eta(x, t) = a \sin(\sigma t - kx) \tag{1.6}$$

Where k is the wavenumber of the wave, and σ the angular frequency such that the frequency (f) and wavelength (λ) of waves are:

$$\sigma = 2\pi f,\ k = 2\pi/\lambda$$

A key result from linear wave-theory is the dispersion relationship, which relates σ and k given the water depth d:

$$\sigma^2 = gk \tanh(kd) \tag{1.7}$$

Throughout this work, we will mainly consider the case where surface waves are propagating in deep water, where $\lambda \ll d$, or $kd \to \infty$, which reduces this dispersion relation to:

$$\sigma^2 = gk \tag{1.8}$$

When linear surface waves travel through water that is moving, the motion of the water introduces a discrepancy between the frequency of the surface waves observed by an observer in a reference frame that is stationary relative to the motion of the water, and an observer in a reference frame moving with the current. The angular frequency in the reference frame moving with the ocean currents is called the *intrinsic* frequency σ, while the frequency in the stationary frame is called the *absolute* frequency ω. The effect of the currents is to change the relationship between σ and ω, such that:

$$\omega = \sigma + \mathbf{k} \cdot \mathbf{U} \tag{1.9}$$

However, when a group of waves passes across a change in $\mathbf{U}$, the number of crests is conserved, meaning that waves must modify their intrinsic frequency σ across the change in current (Ardhuin, 2024). Energy of the waves is not conserved as the waves propagate across the change in currents, since the waves are free to exchange energy with the surface currents, and this results in changes in wave height and steepness (Phillips, 1966; Ardhuin, 2024). Instead, what is conserved in this case is the Wave Action, N, defined as $N = \frac{E(f,\theta)}{\sigma}$ (Bretherton, 1969). The conservation of Wave Action can then be used to create a conservation equation for surface waves that is valid for waves propagating across changing currents (and changing water depths, although that is not considered here). This equation is defined as (Bretherton, 1969; Hegermiller et al., 2019):

$$\partial_t N + \nabla_x \cdot (\mathbf{U} + \mathbf{c_g})N + \partial_k \dot{k} N + \partial_\theta \dot{\theta} N = S_{tot} \tag{1.10}$$

Where c_g is the wave group velocity, $\mathbf{U}$ is the current speed, θ the wave direction, $\nabla_x = (\partial_x, \partial_y)$ is the horizontal gradient operator, $\dot{k}$ and $\dot{\theta}$ are the propagation speeds in k

and θ, and S_{tot} is the sum of all the sources and sinks of wave action (e.g. Wind input, whitecapping dissipation). Through this equation some of the effects of currents on surface waves can be characterized, including:

1. Modifying the advection of wave action in space through the $\nabla_x \cdot (\mathbf{U} + \mathbf{c_g})N$ term.

2. A change in wavenumber through the $\dot{k}$ term.

3. Refraction of waves through the $\dot{\theta}$ term,

4. A change in the relative wind speed, and therefore the wind energy input to the surface waves, which must be parameterized through a modification of wind stress in the S_{tot} term.

There is a long history of studying these effects of currents on waves in both numerical and observational studies (Longuet-Higgins and Stewart, 1964; Ardhuin et al., 2012; Gemmrich and Garrett, 2012; Hegermiller et al., 2019; Vrećica et al., 2022; Iyer et al., 2022; Ho et al., 2023; Bôas et al., 2025; Wang et al., 2025; Papandreou et al., 2026). Work in the last decade since (Ardhuin et al., 2017) has extensively shown that currents impart a rich spatial variability in surface wave fields at scales much finer than the large synoptic scale wind forcing that generates surface waves. Generally, many of these studies have focused observations (Marechal and Ardhuin, 2021; Quilfen and Chapron, 2019; Ardhuin et al., 2017; Iyer et al., 2022; Bôas et al., 2025) or modeling (Hegermiller et al., 2019; Villas Boas et al., 2020; Wang et al., 2025; Marechal and De Marez, 2022) of current impacts on waves which do not consider the time-dependence of the currents. Instead, the goal of many of these studies has been to investigate how different spatial patterns of surface currents impact surface waves. Few recent studies have considered the question of how more time-variable currents impact waves, and how that might differ from steady currents. These studies have largely been focused on tidal currents (Gemmrich and Garrett, 2012; Halsne et al., 2024; Ho et al., 2023), with a few focused on the impacts of currents generated by hurricanes (Wang and Sheng, 2016; Papandreou et al., 2026). Only one study, (Gemmrich and Garrett, 2012) has investigated the potential impacts of currents that vary at frequencies near the inertial-frequency, despite these currents being common throughout the global ocean (Flexas et al., 2019). This represents a gap in understanding of how these currents modify surface waves, and whether the mechanisms might be different than for the more commonly studied steady or tidal current cases.

1.3 Inertial Currents Background

Due to the rotation of the earth, changes in wind stress at the ocean surface can induce a resonant response in the surface layer near the local inertial frequency (Gill, 1982). The most simple model for these currents is the slab model of Pollard and Millard (1970):

$$\partial u/\partial t - fv = \frac{\tau_x}{\rho h} - ru \tag{1.11}$$

$$\partial v \partial t + fu = \frac{\tau_y}{\rho h} - rv \tag{1.12}$$

where $f = \Omega \sin(\phi)$ is the inertial frequency at latitude ϕ. These currents rotate anti-cyclonically, and have been long observed to be generated by the passage of storms D'Asaro (1985). While the initial response of the ocean to the change in wind-forcing in this model is confined to the mixed layer at large scales on the scale of the storm systems, over time the spatial scales of these inertial oscillations can decrease due to interactions with the mesoscale eddy field and the β-effect (D'Asaro, 1989; Alford et al., 2012). Additionally, traditional treatments of inertial oscillations have considered the adjustment of the ocean after the initial deposition of energy into the mixed layer, where convergence and divergence zones caused by the rotation of the inertial oscillations can drive pumping at the mixed layer base, resulting in the generation of downward propagating near-inertial internal waves (Gill, 1984; Alford et al., 2012). In this work we will primarily consider inertial motions within the mixed layer, which have been shown to be one of the largest pools of ageostrophic motions in the ocean, with most of that energy being located at the mid-latitudes (Flexas et al., 2019; Liu et al., 2017; Arbic et al., 2022). Recent observations, including those from global drifters, suggest that spatial scales of these currents tend to be smaller than the synoptic scale of the wind forcing, often having spatial scales of $O(100km)$ in the mid-latitude ocean (Etienne et al., 2025; Kim and Kosro, 2013).

These previous observations and modeling studies indicate that inertial oscillations are 1) A significant source of kinetic energy in the surface ocean and 2) often have spatial scales similar to the mesoscale currents that have been extensively shown to have significant impacts on surface waves. These two factors suggest that inertial currents therefore have the potential to be a significant source of wave-current interactions in the ocean, with the additional factor that the anti-cyclonic rotation of these currents presents an relatively unexplored question in the field of wave-current interactions. The goals of this dissertation are thus to explore the impacts of inertial currents on surface waves, and how these impacts may differ from more extensively investigated steady currents. This work takes a three pronged approach to adding to the understanding of how inertial currents modify surface waves. First, by attempting to expand the observational tools for measuring waves and currents simultaneously. Second, by using idealized models to investigate how inertial current impacts on waves may differ from steady currents. And third, by investigating the impact of inertial currents on waves in multi-year observational records from two locations in the North Pacific.

1.4 Outline

This dissertation is organized into 3 research chapters focused around investigating the impact of inertial currents on surface waves. The first is focused on adding and validating wave-measuring functionality to EM-APEX (Electro-Magnetic Autonomous Profiling Explorer) profiling floats, which have a long history of being used to observe near-inertial currents (Girton et al., 2024). The second chapter is targeted at investigating the theoretical impacts of idealized inertial currents on surface waves through a series of wave modeling experiments with the goal of identifying potential ways in which the inertial rotation of currents may modify the resulting impacts on surface waves. Finally, the third chapter is focused on analyzing observations of wave and inertial currents to identify the mechanisms behind and extent to which inertial currents modify waves in these observational records. The overall research questions motivating each chapter are presented below:

Chapter 2: Validation of Surface Wave Spectral Measurements from Velocity Profiling Floats.

Q2.1: How well can EM-APEX floats measure the surface wave energy density spectra and bulk wave parameters compared to the other well established wave-measuring platforms?

Q2.2: What are the limiting cases beyond which the EM-APEX float loses utility as a wave-measuring platform?

Chapter 3: An exploration of the influence of near-inertial currents on surface waves in idealized models.

Q3.1: In an idealized model of inertial currents, how does varying the inertial period, wave, and current properties impact the resulting wave-current interactions?

Q3.2: How do the resulting wave-current interactions differ from the case of steady currents? How can we best generalize the impacts of time-varying currents on waves?

Chapter 4: Observations of the impact of inertial currents on surface waves: Two case studies.

Q3.1: Do surface wave properties exhibit increase variability in the near-inertial band, and can this be attributed to surface currents?

Q3.2: What is the relationship between the wave-relative inertial current direction and Hs and mss modifications?

Chapter 2

VALIDATION OF SURFACE WAVE SPECTRAL MEASUREMENTS FROM VELOCITY PROFILING FLOATS

2.1 Abstract

EM-APEX floats have primarily been used to measure subsurface ocean velocities for the purpose of studying ocean dynamics and the vertical structure and shear of currents. However, the motionally-induced voltage sensed by the EM-APEX also contains signals from surface wave orbital velocities, and the time taken to pass through the top ∼100 m of the water column is sufficient to estimate a spectrum of surface wave amplitudes with periods from 5–20 seconds (*i.e.* including both wind seas and long swell) with each profile. Following procedures developed by Hsu (2021) and D'Asaro (2015) we analyzed the performance of EM-APEX float measurements of surface-wave spectra, as well as bulk wave parameters such as significant wave height and energy period, against other in-situ wave-measuring platforms during a 2017 field study off the coast of California (ONR's Langmuir Circulation Department Research Initiative, or LC-DRI). We discuss the limitations and uncertainties inherent in the EM-APEX wave measurements, and determine the uncertainty on each individual 1Hz velocity measurement to be on the order of 1.6 cm/s, resulting in a minimal detectable significant wave height of $Hs = 0.6$ m. Results indicate that the EM-APEX surface wave spectral measurements are in good agreement with the other in-situ wave measurements, with correlation coefficients of $R^2 = 0.76$ for significant wave height, and $R^2 = 0.65$ for energy period. This work demonstrates the potential for these floats to be used as a useful tool in future direct measurements of surface-wave driven mixing processes, Langmuir turbulence, and the interactions between surface waves and ocean currents.

2.2 Introduction

Surface waves are one of the most familiar and long-studied dynamical features of the ocean. Yet, many physics of surface waves remain incompletely understood, such as their role in Langmuir circulation (Li et al., 2019), generation of internal waves (Olbers and Eden, 2016; Wagner et al., 2021), turbulence driven by wave breaking (Melville, 1996; Banner and Peirson, 2007), and the interactions between surface waves and ocean currents (Ardhuin et al., 2017; Vrećica et al., 2022; Marechal and Ardhuin, 2021; Smeltzer et al., 2019). These processes are important in determining boundary layer depth, mediate the exchange of heat, momentum, and tracers between the atmosphere and ocean interior, and impact the accuracy of wave forecasts. However, since they occur over small spatial scales that are not resolved in current global climate models (GCMs), their physics are included in these models through sub-gridscale closure schemes and parameterizations, often informed by observational studies of these processes (D'Asaro et al., 2014). Many of these processes are dependent on the interplay between surface waves, wind forcing, ocean currents, and surface-layer properties such as stratification and mixed layer depth. Thus, performing experiments to understand these physics requires observation of all those properties.

Observation of surface waves is commonly done either by surface-following platforms that measure buoy motion via accelerometers (Longuet-Higgins et al., 1963; Antcil et al., 1993; Feddersen et al., 2024), GPS-based position and velocity measurements (Herbers et al., 2012; Thomson et al., 2018, 2019), or satellite altimeter measurements (Hayne, 1980; Hauser et al., 2017; Grigorieva et al., 2022). Expanding and developing new platforms to simultaneously observe subsurface currents, properties of the ocean surface boundary layer, and the surface wave field can allow for the investigation of some yet-unanswered questions regarding the role of surface waves in the physics of the surface-layer and the mechanisms of energy transfer from the atmosphere to the ocean (Ardhuin et al., 2019).

This paper seeks to demonstrate the capabilities of a long-used profiling float to simultaneously measure the ocean surface wave-field, subsurface currents, and temperature and salinity profiles. The EM-APEX (Electro-Magnetic Autonomous Profiling Explorer) is an Argo-like vertically profiling float that measures ocean currents via the electric potential induced by the motion of charged particles in the Earth's magnetic field (Sanford et al., 1978, 2007, 2011). Since surface gravity waves induce ocean velocities (Young, 1999), the EM-APEX could potentially be used to measure surface-wave spectra in addition to the vertical profiles of low-frequency ocean currents the instrument already records. Various methods have been proposed over the years for how to use the EM-APEX float as a measurement platform for surface waves, from the platform's initial development (Sanford et al., 2007) to the present (Hsu, 2021). Hsu (2021) presented the most complete method for surface wave measurement, demonstrating the potential value of wave measurements using the EM-APEX platform for studying drag coefficients in hurricane conditions. Hsu's method outlined the use of the float's 1-Hz sampling of the induced electric field for the determination of surface wave energy density spectra. However, that study was limited to the use of wave model output (WAVEWATCH III (WAVEWATCH III Development Group, 2016)) for validation of the EM-APEX surface wave measurements, and comparison against other in-situ wave-measuring platforms was not possible wiht the data available. Furthermore, the applicability of this platform for measuring surface waves in calmer, non-hurricane conditions was not able to be addressed in (Hsu, 2021).

This paper seeks to explicate the method development of Hsu (2021), validating it against simultaneous surface wave measurements from other wave-measuring platforms during a 2017 experiment off the coast of Southern California, known as the Langmuir Circulation Department Research Initiative (LC-DRI) experiment (Ma et al., 2020; Zeiden et al., 2024). The governing questions that this paper seeks to answer are: 1) How well can the EM-APEX float measure the surface wave energy density spectra and bulk wave parameters compared to the Datawell Waverider buoy and SWIFT buoys? 2) What are the limiting cases beyond which this instrument loses utility as a wave-measuring platform? The instrumentation and fieldwork during the LC-DRI campaign will be described in the section below, followed by a methods section discussing the data-processing techniques used to estimate surface wave spectrum from the EM-APEX floats deployed during this campaign. The EM-APEX measurements and comparisons with other platforms are presented in the results section, along with a discussion of the sources of error in these measurements and their implications for measurement accuracy.

2.3 Data and Field Campaign

Analysis was performed using data collected during the LC-DRI (Waves, Langmuir Cells and the Upper Ocean Boundary Layer Departmental Research Initiative) experiment off the coast of Southern California from March 21 - April 5 2017 (Ma et al., 2020). Over a two-week period, 6 EM-APEX floats were deployed, alongside 3 Mixed-Layer Lagrangian floats (D'Asaro, 2003), 8 SWIFT drifters (Thomson, 2012), a Datawell Waverider buoy, and the R/P Flip (Fig 2.1). Numerous other instruments and platforms were deployed during the LC-DRI experiment, such as wave-gliders (Grare et al., 2021), the R/V Sally Ride and and the R/V Sproul, but those data are not presented here. The Datawell Waverider buoy (referred to as the Waverider throughout), which was deployed in a fixed location for the duration of the experiment, reported a suite of bulk wave parameters, such as significant wave height (H_s) and energy period (T_e), as well as average surface wave energy density spectra, every 30min. Unlike the Waverider buoy, the SWIFT drifters do not maintain a fixed position, but drift freely at the surface while deployed. These drifters report the same suite of spectral and bulk wave measurements as the Waverider buoy.

The 6 EM-APEX floats were configured to make 2 profiles (1 down, 1 up) approximately every hour, descending to a depth of $\sim$200 meters. 1693 velocity and CTD profiles were recorded in total during the LC-DRI experiment. The EM-APEX floats only save full up-down profiles of 1Hz electric field measurements every tenth profile, and for the remainder of the profiles only processed velocity data over 50-second windows was saved, resulting in 174 total 1Hz profiles during this deployment that can be used for evaluation of the EM-APEX surface wave spectrum estimation method.

During the field campaign, winds and waves were primarily from the northwest and 10m winds ranged from approximately $2m/s$ to $20m/s$ (Fig 2.2b). Significant wave height as measured by the Waverider buoy ranged from $0.67m$ to $4.8m$ (Fig 2.2c). To characterize the mean spatial pattern of surface waves in the region during the experiment, we investigated significant wave heights from a climate reanalysis product (ERA5, run by European Centre for Medium-Range Weather Forecasts) over the LC-DRI experiment (Hersbach et al., 2023). Fig 2.2a shows the mean significant wave heights averaged in time over the deployment area.

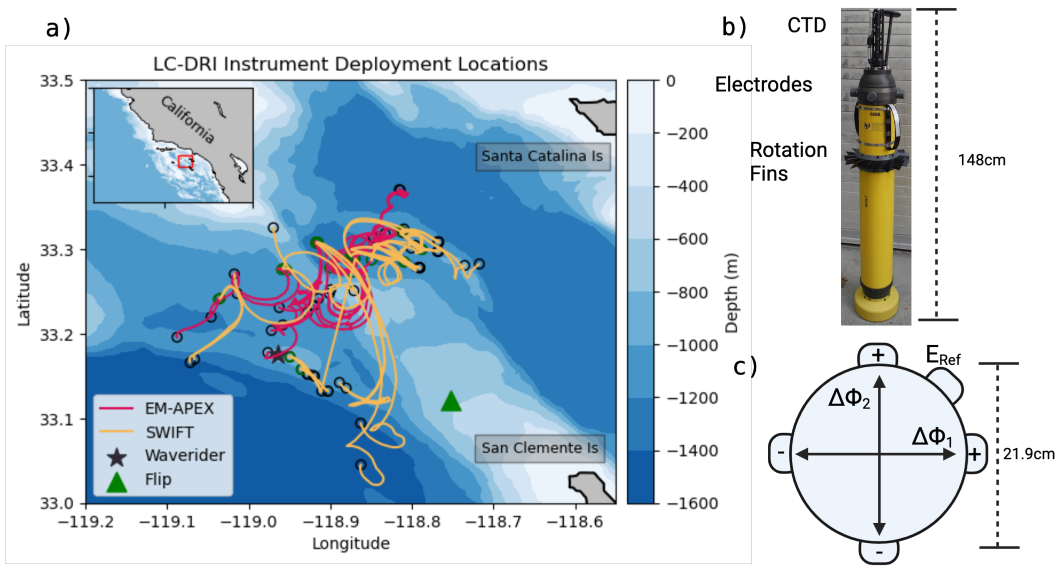

Figure 2.1: (a) Map of LC-DRI deployment region and instrument locations. Inset shows experiment location (red box). Orange lines show trajectory of all SWIFT buoys over the deployment, and red lines show EM-APEX float trajectories. Green circles indicate the deployment locations, and black circles the final positions of each instrument. Black star indicates Waverider buoy location, and green triangle the location of the R/P Flip. (b) EM-APEX float, with the CTD instrument package, electrodes, and rotation fins shown. The total length of the float is 148cm. (c) Cross section of the float showing electrode positions, with $\Delta\Phi_1$ and $\Delta\Phi_2$ indicating the voltage difference across each pair of electrodes (see eq. 2.1), separated by 21.9cm. E_{ref} labels the fifth electrode, which is used as a reference value for the other electrode measurements (Sanford et al., 2005)

This indicates that we might expect some spatial heterogeneity in the wave field over the study region due to the sheltering and refractive effects of the channel islands. Furthermore, the LC-DRI technical report from Ma et al. (2020) indicated some spatial variability in H_s measurements from the SWIFT and Waverider buoys. This heterogeneity may appear as discrepancies between bulk wave measurements recorded by instruments separated spatially during the field campaign, which should be kept in mind when considering the results below. Additionally, O'Reilly et al. (2016)'s swell model for the Southern California Bight region showed remotely generated swell significant wave heights ranging from approximately $0.3m$ to $2m$ in this region during the experiment. These environmental data suggest that the surface wave conditions during this experiment present a robust test-bed for analyzing EM-APEX surface wave measurements over a broad range of both swell and wind-wave conditions, with regard to both wave amplitudes and peak wave frequencies.

2.4 Methods

2.4.1 EM-APEX Wave Processing

This section overviews the methods of deriving surface wave spectra from the EM-APEX float, following a set of procedures first presented in Hsu (2021), and outlines the overarching principles. The EM-APEX float is a buoyancy-driven profiling float utilizing two pairs of orthogonal electrodes that record measurements of electric-field (Sanford et al., 2005). The float profiles in the vertical by adjusting it's buoyancy with a buoyancy pump, and can descend up to $2000m$ depth at a rate of $\sim 0.1m/s$. During ascent and descent, the float records conductivity, temperature and depth with $\sim 2m$ resolution with a Sea-Bird SBE-41CP CTD. A ring of fins positioned around the exterior of the float's hull cause the float to spin as it ascends and descends, with a rotational period of 8-15s depending on the vertical speed of the float. The angular orientation of the float while it profiles is recorded with an onboard magnetometer, and horizontal and vertical acceleration of the float is also measured by an IMU. Electrode voltages are recorded at a rate of 1Hz (sampled at 20Hz and then averaged over 1s onboard), and low-frequency currents are reported every 25s (Sanford et al., 2005).

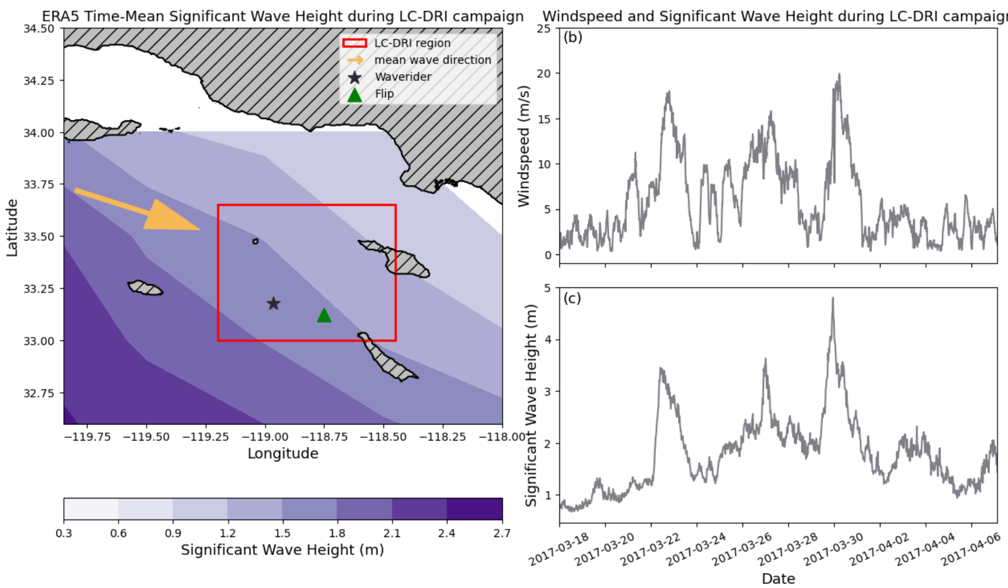

Figure 2.2: (a) Map of mean significant wave height from ERA5 reanalysis hourly data (Hersbach et al., 2023) over the LC-DRI deployment with the study region shown in red. Blank regions near the coast are areas where the ERA5 product does not report H_s values. Yellow arrow indicates mean wave direction during the LC-DRI experiment, and the location of the Waverider buoy (black star) and R/P Flip (green triangle) are shown as in figure 2.1 above, and the small circle in the northwest sector of the LC-DRI region is Santa Barbara Island. (b) Time-series of wind speed over experiment recorded by the R/P Flip. (c) Significant wave height recorded by the Waverider buoy.

Velocity measurements are made by utilizing the fact that horizontal motions of the charged particles in seawater through the z-component of the Earth's magnetic field induce an electric field proportional to the ocean current velocity (Sanford et al., 2005). This electric field is measured as a voltage drop across an electrode pair (Fig. 2.1). However, the voltage measured across the float's electrodes responds to other environmental factors in addition to velocity. Namely, fluctuations in temperature, salinity, and pressure induce low frequency variations in the voltage measured on each electrode. This non-velocity driven drift in the voltage can occur over similar spatial and temporal scales as changes in ocean currents. The float's rotation about its vertical axis during ascent/descent allows for the isolation of the velocity-driven signal from the non-velocity driven electrode drift. For each rotation of the float, the electrode registers a sinusoidal voltage with an amplitude proportional to the magnitude of the ocean current. Thus, as the float profiles, the measurements by each electrode pair appear as a low frequency drift modulated by a sinusoidal signal at the rotation period driven by voltage changes due to the principles of motional induction (Fig. 2.3). As in Sanford et al. (2005) and Hsu (2021), over short time windows the environmental influences on electrode voltage are assumed to be approximately linear, and the voltage drop across a given electrode pair can be modeled using equation 1.

$$\frac{\Delta\Phi_i}{L} = a_{1,i}\cos(\Omega t) + a_{2,i}\sin(\Omega t) + a_{3,i}t + a_{4,i} + \epsilon_i(t) \tag{2.1}$$

Where $\Delta\Phi_i$ is the voltage drop across an electrode pair, L is the distance separating the electrodes of each pair, Ω is the rotation rate of the EM-APEX float, and t is time. $a_1 \rightarrow a_4$ are fitting coefficients,[1] and ϵ is the residual left over after fitting, which varies in time. The subscript i distinguishes between each electrode pair, so $i = 1, 2$.

The typical EM-APEX method of deriving velocity from the electrode measurements involves taking a fit to the voltage time-series for each electrode (Sanford et al., 2005, 2007). The time-series of each profile is divided into 50s windows with a 25s overlap, and then following equation 1, a least squares fit of each measurement window is made, determining the constants $a_1, ..., a_4$, with residuals ϵ_i's. The basic underlying assumption is

[1] In practice, the cosine and sine basis functions are replaced by the de-meaned and normalized perpendicular horizontal magnetometer channels, which makes the fitting insensitive to any variations in the rotation frequency Ω over the 50-second window.

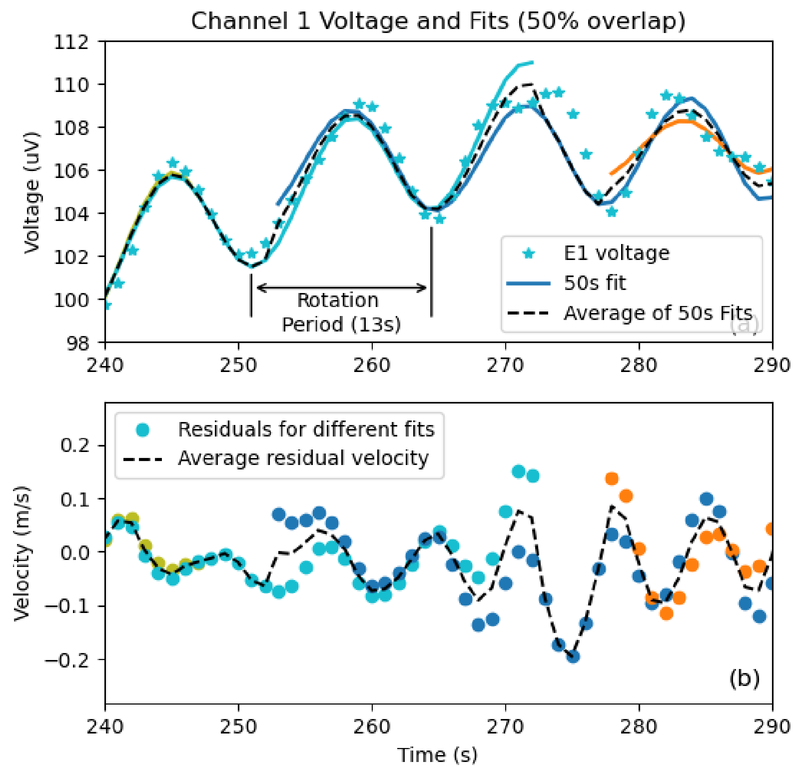

Figure 2.3: (a) An example of the voltage measured on an electrode channel during a single EM-APEX profile. Blue stars show each 1Hz voltage measurement, and solid colored lines show 50s fits from Eq. 2.1. Different colors show consecutive 50s fits (each offset by 25s). Dashed line shows average of these successive windows. A sample rotation period is also shown. (b) Demonstration of residual velocities and uncertainties due to the 50s fitting procedure. The resulting residual velocities are shown (dots, colors corresponding to which fit in (a) they are derived from). Significant spread in the velocities calculated from each of the fits demonstrates the uncertainty in the 1Hz velocity measurements introduced by the fitting procedure.

that 50s is a short enough time window that the electrode drift can be modeled with a linear fit. The extent to which this assumption holds contributes to the error on each 1-Hz velocity measurement. Following the EM derivations from Sanford et al. (1978), the low-frequency (frequencies $< 0.02Hz$) currents $(\bar{u}, \bar{v})$ are approximated by equations 2.2-2.3.

$$\bar{u} = \frac{a_2}{F_z(1 + C_1)L}, \tag{2.2}$$

$$\bar{v} = \frac{F_y(1 + C_2)w_{EM} - a_1}{F_z(1 + C_1)L} \tag{2.3}$$

where here a_1 and a_2 are the coefficients from equation 2.1. F_y and F_z are the y and z components of the Earth's magnetic field respectively, L is the separation between the electrodes, w_{EM} is the average vertical profiling speed of the float, and C_1 and C_2 are constants related to the distortion of electric current flow around the instrument and the electrical impact of flow around the vertically moving float, respectively (Sanford et al., 1978). These constants have been estimated for the EM-APEX shape, based on tank testing and data analysis minimizing down–up velocity differences as $C_1 = 0.5$ and $C_2 = -0.2$. The residuals ϵ_i in equation 2.1 can be used to observe the higher frequency currents (motions with periods shorter than the fitting window of 50s, or frequencies $> 0.02Hz$). These are given as:

$$u' = \frac{\epsilon_1 \sin\theta - \epsilon_2 \cos\theta}{F_z(1 + C_1)L} \tag{2.4}$$

$$v' = \frac{-\epsilon_1 \cos\theta - \epsilon_2 \sin\theta}{F_z(1 + C_1)L} \tag{2.5}$$

where θ is the orientation of electrode channel 1 (counterclockwise from geomagnetic east) determined using the float's horizontal magnetometer measurements, and channel 2 is oriented 90° clockwise from channel 1. The u' and v' represent the total high-frequency velocity from all processes but tend to be dominated by surface waves in the upper 100 m, as apparent from the exponential decay in amplitude away from the surface (Sanford et al., 2005, 2011).

From the resulting residual (high-passed) timeseries, surface wave spectra can be derived based on 1) the assumption that these high-frequency velocities are wave-driven velocities, and 2) the assumption that the surface waves are approximately linear and obey the linear deep-water wave dispersion relation. For linear deep water waves traveling in the x-direction, the resulting ocean velocities are given by:

$$u' = 2\pi a f \cos(kx - 2\pi f t + \phi)e^{kz} \tag{2.6}$$

where a is the wave surface amplitude, f is the wave frequency, and k is the wavenumber. For linear, deep water waves the dispersion relation is given by $k = (2\pi f)^2/g$, where here g is the gravitational constant (Young, 1999). For a surface wave at any given frequency, the amplitude of resulting ocean velocity decays exponentially with a decay scale of $\frac{1}{k}$. Each frequency component of a surface wave spectrum therefore contributes to the resulting surface-wave velocity profile with a different depth dependence. The velocities induced by low frequency, longer wavelength waves penetrate deeper below the surface, whereas the velocities produced by higher frequency waves are trapped within a very shallow band near the surface of the ocean.

Attempting to use an EM-APEX float to reconstruct a surface wave spectrum while profiling vertically is thus complicated by the differential depth-decay of each wave frequency. However, spectral processing techniques can be applied based on linear wave theory to correct for the profiling behavior of the float, which are discussed in section b. below. Additionally, the fitting procedure outlined in equation 2.1 is imperfect and introduces uncertainty into the surface-wave velocities that the wave-estimation technique relies upon. Fig 2.3b demonstrates an example of the noise due to a non-linear electrode drift, where spread in the estimated residual velocity values (dots) away from the mean (dashed line) indicates uncertainty in the residual velocity value. Section d. discusses the methods used to estimate the magnitude and importance of this uncertainty.

2.4.2 Spectral Processing

Spectral processing of the EM-APEX high-frequency u', v' velocity profiles were done following the methods of D'Asaro (2015) and Hsu (2021). For each profile, the resulting u', v' time-series are broken up into 120s spectral windows, with a 50% overlap. A Hann window taper is then applied to each window, and then a Fourier transform is computed over each tapered window. The Fourier Transform of the u' and v' variables is used to compute the autospectrum S_{uu}, S_{vv} following Thomson et al. (2018):

$$S_{uu} = \frac{F_u F_u^*}{t_s f_s},\ S_{vv} = \frac{F_v F_v^*}{t_s f_s} \tag{2.7}$$

where t_s is the length of the spectral windows in seconds, f_s is the sampling frequency, and F_u, F_u^* are the real and imaginary parts of the Fourier transform of the x-velocity respectively, with F_v, F_v^* the same for the y-velocity. These velocity autospectra are used to compute the wave energy density spectra:

$$E(f) = \frac{S_{uu} + S_{vv}}{(2\pi f)^2} \tag{2.8}$$

D'Asaro (2015) and Hsu (2021) developed methods for correcting the energy surface wave energy density spectra observed by a vertically profiling instrument. Using these corrections, the energy density spectra from the raw u', v' profiles are corrected to account for the depth decay of the wave-driven velocities, and the vertical motion of the float within each spectral window. Four corrections are applied to the raw spectrum $E(f)$, all derived in D'Asaro (2015). These corrections correct for the depth decay of the surface wave velocity signal (ZC), the vertical motion of the float during each spectral window (WC), the discrete temporal sampling of wave velocity (dTC), and spectral spreading that results from the windowing (SC). The depth correction is most significant of these, and is described here. The description of the other three corrections are provided in detail in D'Asaro (2015). For a given raw spectrum $E(f)$, the depth correction is given by:

$$E(f)_{zc} = E(f)e^{2kz} \tag{2.9}$$

where $k = (2\pi f)^2/g$ for linear, deep-water waves, and z is the median depth of the float for the spectral window used to generate $E(f)$. At higher frequencies/wavenumbers, the wave-driven velocity signal decays more rapidly, and thus may be below the noise floor of the instrument. For frequencies below this noise floor, this depth correction simply amplifies the instrument noise, instead of correcting for the depth-decay of a real signal. D'Asaro

(2015) and Hsu (2021) account for this by imposing a maximum depth correction, termed C_{max}, above which $E(f)$ is set as undefined. Therefore, for frequencies/wavenumbers where $e^{2kz} > C_{max}$ the values of the spectrum $E(f)$ are left undefined.

Both Hsu (2021) and D'Asaro (2015) use values of $C_{max} = 100$, and in keeping with this we have chosen the same convention throughout, as the wave-heights observed here were not found to be very sensitive to this value. This maximum depth correction limits the maximum surface-wave frequency that can be resolved from a given spectral window. Since the EM-APEX float descends and ascends at a rate of approximately $0.1m/s$, for a 120s spectral window, $6m$ is roughly the minimum median depth possible for a spectral window, and so $0.31Hz$ is approximately the highest possible resolved surface-wave frequency from this instrument. In this experiment, ascending profiles had an average median depth of their first spectral window of 12.78m, while descending profiles had an average median depth of 18.5m. This results in a maximum resolved frequency of about 0.21 Hz for ascending profiles, and about 0.18 Hz for descending profiles. Variation in the minimum depth at which data was recorded across profiles results in some variation in the maximum frequency resolved by this algorithm. It's worth noting here that the 1Hz sampling rate of the EM measurements should be fast enough to exclude any aliasing in the range of surface-wave frequencies ($f < 0.3Hz$).

2.4.3 Bulk Wave Parameter Estimation

After spectra are computed, these spectra are used to calculate bulk wave parameters, such as Significant Wave Height (H_s), and Weighted Energy Period (T_e). These are standard wave parameters reported by traditional wave measurement platforms, and can be used to represent certain characteristics of the wave-field with a single value. The most often reported of these bulk wave parameters is H_s, which represents the average height of the largest $1/3^{rd}$ of of the surface waves. From a wave spectrum $E(f)$ it can be estimated from equation 1.4 above (Munk, 1944):

$$H_s = 4\sqrt{\int E(f)df}$$

In addition to significant wave height, bulk measurements of wave period are often used

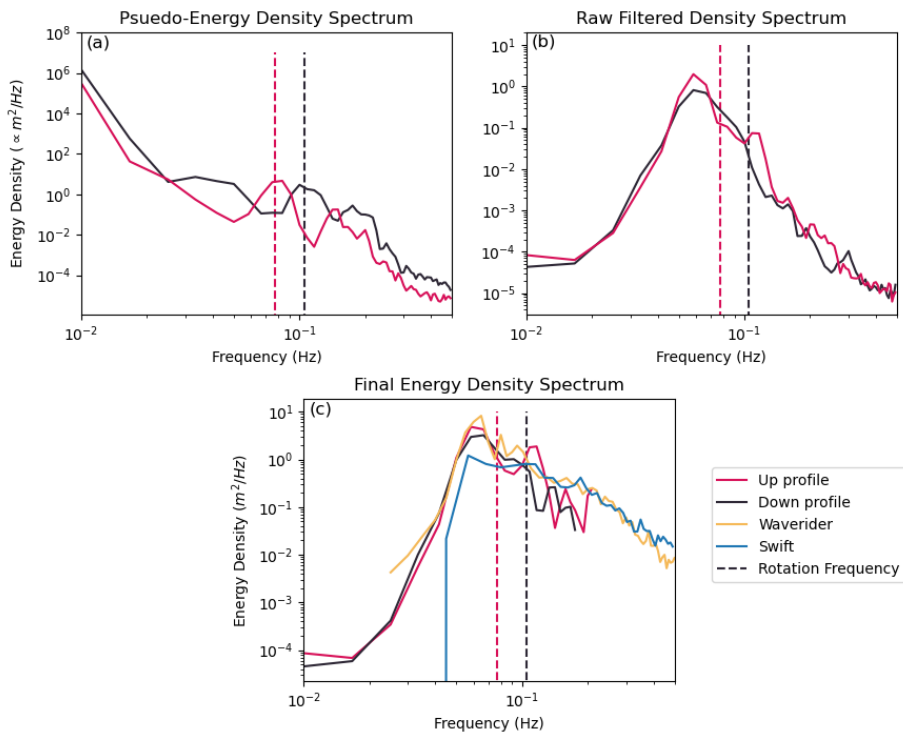

Figure 2.4: Overview of spectral processing steps. (a) shows a "pseudo"-Energy density by taking the spectra of the raw voltage measurements for an up (red) and down (gray) profile. Note the spectral peak at the mean rotation frequency of the float is the dominant feature in each spectrum and differs between up and down profiles. (b) shows the spectra of the residual velocities after the fitting procedure has been applied, as well as a high-pass filter to filter out the low-frequency noise below $0.04 Hz$ that aligns with the high-pass filter used in the Waverider spectral processing. Note that the rotation frequency peaks from (a) have been removed by the fitting procedure. (c) Final spectra after the application of corrections from D'Asaro (2015), compared with the Waverider (orange) and Swift (blue) spectra taken at the same time.

as a metric for assessing wave measurements. One bulk parameter that captures information about the wave period is the weighted energy period, T_e, which is defined as

$$T_e = \frac{\int E(f)df}{\int fE(f)df} \tag{2.10}$$

While other bulk metrics for period have been used in previous literature (Ardhuin et al., 2019; Antcil et al., 1993; Young, 1995), recents surface wave measurement comparison literature has used this expression for T_e (Collins et al., 2024; Thomson et al., 2018), so we have chosen to use it here. For calculations of both Hs and T_e we integrated spectra over the frequency range of $0.05 - 0.3Hz$ for all instruments. For the EM-APEX derived spectra, which have variable maximum frequencies, each spectra was extrapolated out to $0.3Hz$ by assuming an f^{-4} equilibrium range spectral slope (Phillips, 1985) before H_s and T_e calculations were performed. From the EM-APEX spectrum calculated for each EM-APEX profile, each of these two bulk wave parameters are calculated and compared against measurements from both the Waverider and SWIFT buoys.

Hsu (2021) indicated that it is possible to measure both bulk wave direction properties as well as directional spectra with this EM-APEX float by incorporating the time-series of vertical acceleration recorded by the onboard IMU. However, further work is still required to test and validate this method of directional estimation derived in Hsu, 2021. In this dataset, we observed contamination of the vertical acceleration measurements on the EM-APEX float that are necessary for the estimation of the directional wave spectra following the methods from Hsu (2021). Without the vertical acceleration data it is possible to use the auto-spectra and cross-spectra of the u and v wave velocities to determine the axis of wave propagation (Herbers et al., 2012; Thomson et al., 2018), but this method can not determine which direction along that axis the waves are propagating. We plan to continue to investigate the behavior of the accelerometers used on the EM-APEX float and their ability measure vertical acceleration spectra, and as such have left the validation of the float's wave-directional measuring properties out of the results presented here and will include this analysis in future work.

2.4.4 Surface-Wave Velocity Uncertainty Simulations

In order to better understand the impact of uncertainties of the 1Hz residual velocity measurements calculated using equations 1-3, a numerical model was constructed to simulate the EM-APEX 1Hz sampling under different wave and current conditions. The model functions by simulating the descent/ascent of the EM-APEX float and the electric field measurements it would make while profiling, given a specified surface-wave spectrum and 1Hz velocity noise level. The details of this model are discussed in Appendix A. Using this model, we were able to estimate the magnitude of the uncertainty of each 1Hz velocity measurement caused by the fitting procedure used to derive the velocities. This uncertainty due to fitting adds a white noise into the 1Hz velocity measurements, the magnitude of which determines the minimum significant wave-height detectable by the EM-APEX float. By varying the surface wave height and 1Hz velocity noise level, the model enabled us to test the relationship between the noise on the 1Hz velocity measurements and the resulting minimum detectable wave height. The results of these simulations are presented below.

2.5 Results

2.5.1 Wave Spectrum

Fig 2.4c shows a sample EM-APEX spectrum from a single profile (both up and down) compared to the Waverider and SWIFT spectra collected at the same time. While the EM-APEX float measurements have lower highest resolved frequencies than either of the other two platforms, in this case the peak and overall magnitude of the EM-APEX derived surface wave spectra match the other instruments well.

Comparing spectral measurements between the EM-APEX float and Waverider buoy on the whole, Fig 2.5 shows a time-series of EM-APEX derived surface-wave energy density spectra alongside the same time-series from the Waverider buoy. While both the temporal and frequency resolution of the EM-APEX time-series are lower than in the Waverider timeseries, the same main spectral features stand out in both records. Namely, large spectral peaks of approximately the same magnitude at around $f = 0.1 - 0.15Hz$ around March 22nd and March 30th, as well as low frequency swell peaks that appear on March 28th and April

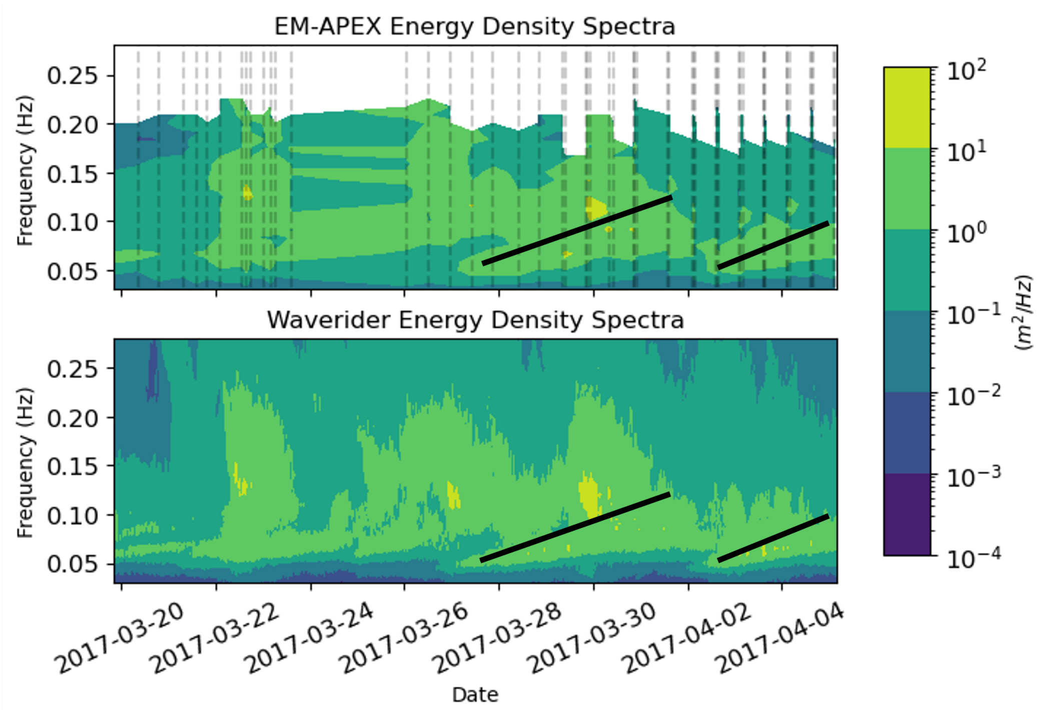

Figure 2.5: Timeseries of energy density spectra from the EM-APEX float measurements and Waverider measurements. Dashed vertical lines in the top panel indicate sampling times from the EM-APEX floats, and the colorbar is linearly interpolated between these measurements. Solid black lines indicate similar structure of development of higher-frequency waves over time captured by both instruments.

2nd and then develop into higher-frequency waves over the ensuing days (marked with the solid black lines in this figure). While some of the features of the wave-rider spectra are missed by the EM-APEX float, primarily the higher detail features smoothed over by the EM-APEX float's lower resolution in frequency space, the major large scale features between 0.04 and $0.2 Hz$ are captured.

2.5.2 Bulk Wave Parameters

In order to analyze the fidelity of the EM-APEX measurements as an ensemble, Fig 2.6 shows a time series of significant wave heights as calculated from the EM-APEX floats and

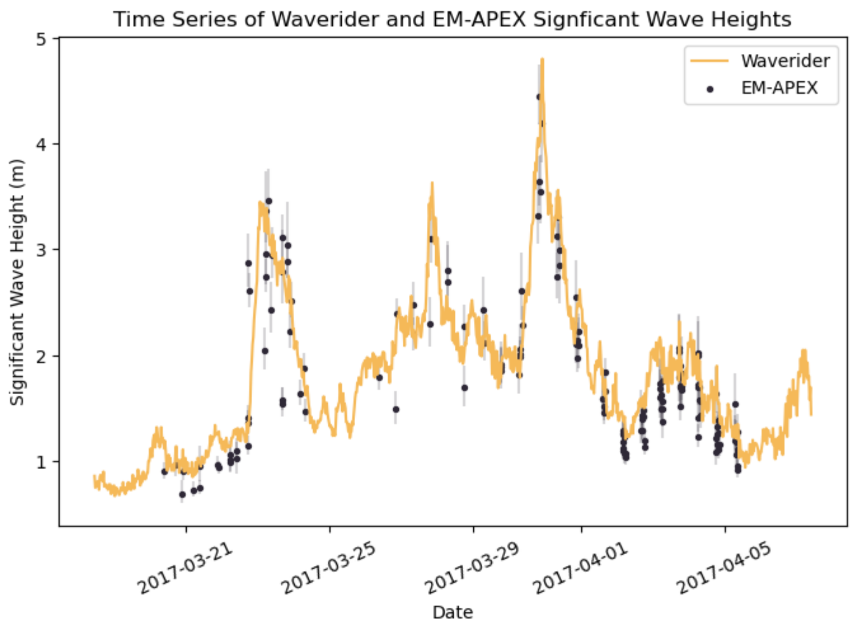

Figure 2.6: (a) Time series of EM-APEX estimated H_s, compared with Waverider measurements. EM-APEX measurements are shown as black dots, with 95% confidence intervals shown.

Waverider buoys. Qualitatively, this figure demonstrates the EM-APEX float significant wave-height measurements accurately replicate the changes of the surface wave-field over the course of the experiment. There are a few EM-APEX measurements with particularly large error during the first large peak in wave height around March 24th. Investigation into these measurements revealed that this error is likely due to a combination of a significant wind-wave peak with a frequency closer to $0.2Hz$ and these particular profiles having minimum depths below $20m$. This results in a reduced signal at frequencies closer to 0.2Hz for these profiles, and therefore more sporadic H_s values.

A more quantitative comparison is shown in Fig 2.7 shows the significant wave height measurements from the EM-APEX float plotted against the corresponding measurements from the Waverider (a) and SWIFT (b) buoys. Perfect agreement between measurements would lead to points lying perfectly along the shown 1:1 line. These scatter plots show that for significant wave-height the EM-APEX measurements agree well with the other nearby platforms. Linear regressions of EM-APEX Hs measurements against Waverider and Swift measurements have R^2 values (proportion of variance explained) of $R^2 = 0.76$ between the EM-APEX float and the Waverider buoy, and $R^2 = 0.71$ between the EM-APEX float and the SWIFT buoys. Since distances between the EM-APEX floats, the Waverider buoy, and SWIFT buoys vary significantly over the course of the experiment, SWIFT comparisons in Fig 2.7 were done only for measurements where the SWIFT and EM-APEX floats were within 10km of each other. Given some spatial heterogeneity of the wave-field due to refraction and sheltering from the nearby Channel Islands, it is expected that there be some spread of measurements away from the 1:1 line shown in these figures. Fig 2.7c combines the wave measurement comparisons, plotting the EM-APEX significant wave height measurements against the nearest measurement, whether from a SWIFT drifter or the Waverider buoy. Together, figures 2.6 and 2.7 show that the EM-APEX significant wave height measurements are in good agreement with the other two platforms used during the LC-DRI experiment, and capture the dominant characteristics of the wave field during the same period. Table 4.1 shows the corresponding correlation coefficients, biases and error from each of these comparisons of the EM-APEX float measurements. The root mean square error is between 30 and 40cm, with a bias ranging from $-20cm$ to $10cm$. These biases, errors and correlations are of similar magnitude as for some other wave-measuring platforms, such as the Wave-Glider platform discussed in Thomson et al. (2018), although this is worse performance than found in many other recent comparisons between in-situ wave-measuring sensors, such as the various GPS-based instruments tested in Collins et al. (2024), or the wave-glider observations during the LC-DRI experiment reported in Grare et al. (2021), which found higher correlation coefficients ($R > 0.9$), lower biases ($< 10cm$), and lower RMSE's ($< 15cm$) than shown in table 4.1 here.

It is worth noting that at surface wave frequencies, the vertical profiler may not perfectly follow the water's horizontal motion. A quadratic drag model for an inertial float suggests a time delay for lateral accelerations of only a second or two, and thus negligible impact on the 50-second averages used in constructing the velocity profile. However, at the 5–15 second periods of surface waves, such a delay attenuates the wave orbital velocities by up to 2–15%. The impact of the float's inertia the wave measurements (combined with the impact of the compensating electric currents driven by the relative flow around the instrument body) is discussed in more depth in Appendix B below. Results suggest that the inertia of the float may result in between a $2 - 6\%$ error in measured wave-height (or about 5-10cm). Given the uncertainties in these estimates, it is possible that a sizable portion of the bias and error in the best-fit slopes in Table 4.1 are due to this effect.

Fig 2.8 shows the results of the calculations of T_e, calculated over the frequency range $0-0.3$Hz, from the EM-APEX dataset compared to the Waverider, Swift, and spatially nearest measurements, and the statistics for this comparison are shown in table 4.2. Agreement between the EM-APEX float and the other sensors is slightly worse for T_e than H_s, with $R^2 = 0.65$ for the comparison with the Waverider, and $R^2 = 0.60$ for the comparison with the SWIFTs. The EM-APEX showed very low bias compared to the Waverider ($0.1s$), with an RMSE of $0.8s$. Bias ($0.7s$) and RMSE ($1.0s$) was slightly larger when compared to the SWIFTs. This is also slightly worse performance than what is found for other instruments in Collins et al. (2024), which generally reported biases $< 0.3s$, RMSEs $< 0.6s$, and correlation coefficients $R > 0.79$. On the whole these results show relatively good agreement with the the baseline measurements, and indicate that the EM-APEX float accurately measures bulk period parameters during this experiment as well.

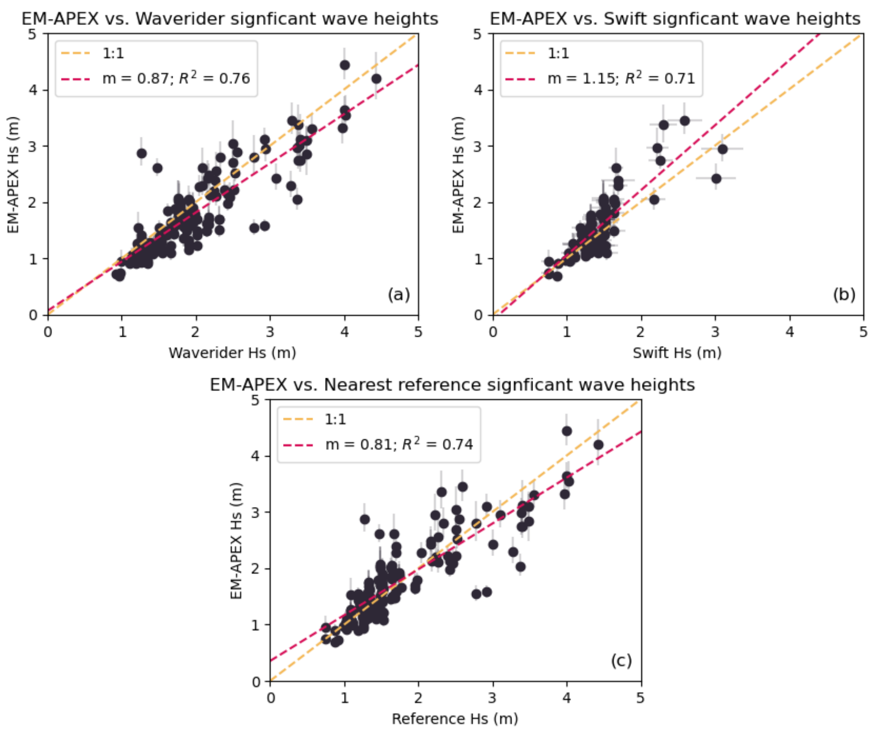

Figure 2.7: Significant wave height from EM-APEX float vs. corresponding Waverider (a) and SWIFT (b) measurements. Swift measurements in (b) are reported as the mean of all swift significant wave height measurements taken within a 1 hour window around the corresponding EM-APEX measurement. These are also restricted to those within 10km of the corresponding EM-APEX measurement to limit overestimation of the error due to real spatial heterogeneity of the wave-field. (c) shows a combined comparison of the EM-APEX measurement against the closest nearby reference significant wave height measurement. Orange dashed line in each figure shows 1:1 line, blue dashed line shows linear best fit. R^2 value and slope of the best fit line is shown in the legend.

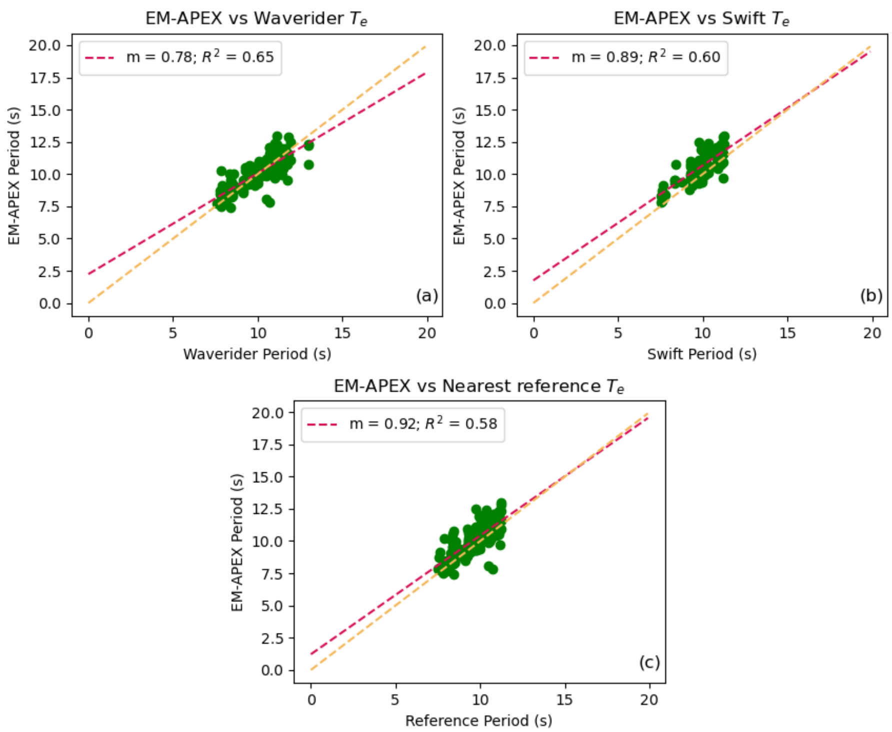

Figure 2.8: Weighted Energy Periods T_e (green) measured by the EM-APEX float plotted against the corresponding (a) Waverider, (b) SWIFT, and (c) closest nearby measurements. 1:1 and best fit lines are shown, with the slope and R^2 of the fit shown in the legend.

Table 2.1: Significant wave height (H_s) correlation coefficients, biases, and errors

Comparison	R	*Bias*	*Error*	R^2	*Slope*	*Intercept*
Waverider	0.87	-0.2m	0.4m	0.76	0.87	0.1m
SWIFT	0.84	0.1m	0.3m	0.71	1.15	-0.1m
Combined	0.86	0.02m	0.4m	0.75	0.81	0.4m

Table 2.2: Wave Period correlation (T_e) coefficients, biases, and errors

Comparison	*R*	*Bias*	*Error*	R^2	*Slope*	*Intercept*
Waverider	0.81	0.1s	0.8s	0.65	0.78	2.3s
SWIFT	0.77	0.7s	1.0s	0.60	0.89	1.8s
Combined	0.76	0.5s	0.9s	0.58	0.92	1.2s

2.5.3 Minimum Detectable Waveheight

In order to characterize the uncertainty on each 1Hz measurement Fig 2.9a shows the distribution of differences between each residual velocity value and the average residual velocity at each point in time (see Fig 2.3b). The distribution of all these differences indicates the distribution of uncertainties in each 1Hz measurement due to errors in the 50s fitting procedure used to isolate the wave-driven velocities. The standard deviation of these measurements given by $\sigma = 0.016 m/s$.

This mean standard-deviation of each individual velocity measurement was then used to calculate the theoretical lower limit of the EM-APEX float's significant wave height measuring capabilities. Following the EM-APEX float simulation procedure outlined in the methods, EM-APEX float profiles were simulated under a range of significant wave heights and a range of 1Hz noise levels. Fig 2.9b shows the modeled relationship between the significant wave height of the wave-field input into the simulation, and the simulated measured significant wave height. 5 different example noise levels are shown out of the 10 levels modeled. This figure demonstrates that the 1-Hz residual velocity noise results in a H_s noise floor which limits the minimum H_s which the float can reliably measure. Here the minimum detectable H_s is defined as the smallest H_s for which the H_s of the input wave-field is within the 95% confidence interval of the simulated float H_s measurement. Fig 2.9c shows the relationship between the 1Hz noise level and minimum detectable H_s, along with a linear fit to the simulated data points. Based on this fit ($R^2 = 0.95$), given the observed 1Hz noise level of $\sigma = 0.016$ m/s, shown in Fig 2.9a, the minimum measurable H_s

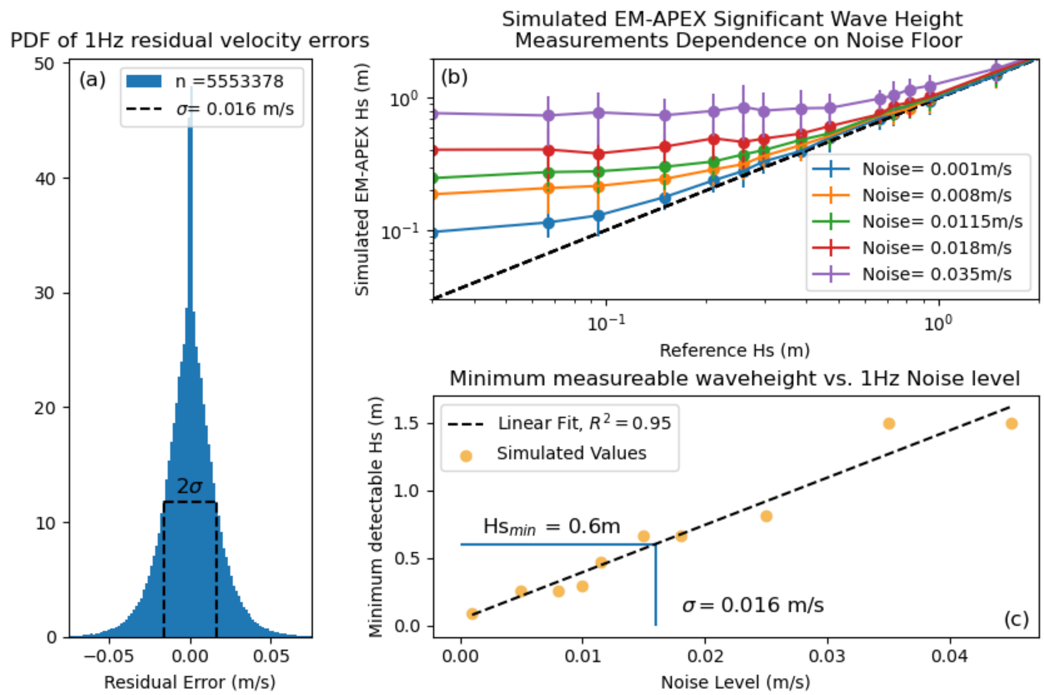

Figure 2.9: (a) Distribution of 1Hz residual velocity uncertainties from all EM-APEX 1Hz profiles during the EM-APEX deployment. (b) Simulation of measured H_s as a function of input H_s and noise level. Each cure shows simulated EM-APEX significant wave height measurements over a range of surface wave fields with different significant wave heights for a given 1Hz noise level. 95% C.I. bars are shown for each measurement. For each noise level the lowest input significant wave height for which the input H_s is within the error bars of the simulated value is identified as the lower limit of detection for that noise level. (c.) Scatter plot of the lower detection limit as a function of noise level. This data closely follows a linear relationship, with the linear fit shown. Given the observed noise level of $\sigma = 0.016m/s$, the fit line indicates a minimum detectable wave height for the EM-APEX surface wave routine of $0.6m$ (indicated by the blue lines).

was found to be $Hs = 0.6m$. Thus, this EM-APEX wave-measuring algorithm is unlikely to be able to reliably measure values of H_s below $0.6m$, although these conditions were not observed in the LC-DRI dataset.

2.6 Discussion

The results of this paper indicate that the EM-APEX float is capable of capturing the dynamics of ocean surface waves during the LC-DRI experiment up to approximately $0.2Hz$. This study expanded the processing method derived in Hsu, 2021 and validated the results of this method against other nearby in-situ measurements across a range of significant wave heights and wave-fields. This work suggests that this data processing method renders the EM-APEX float a potentially useful tool for observing subsurface dynamics driven by ocean-surface waves. In the dataset used there are some limitations to the EM-APEX surface wave measurements due to sampling parameters that were chosen without surface wave measurements in mind, thus some improvements could be made for an experiment focused on leveraging the EM-APEX's surface wave measuring ability. Namely, adjusting the minimum depth at which data is recorded would better standardize the maximum resolved surface wave frequency and allow for measurements closer to the maximum theoretically resolved frequency of $0.3Hz$. Furthermore, for a wave focused study, recording the electrode data on every profile rather than just every ten profiles, would vastly increase the temporal and spatial density of these surface wave measurements. The roadblocks to recording $1Hz$ data every profile are largely the float's limited on-board memory and satellite bandwidth. However, an inclusion of this wave-processing algorithm on board would allow for significantly improved time-resolution and statistics of the EM-APEX wave measurements. It would be possible to design a modified version of this algorithm to compute the mean surface wave spectra at the end of each profile, and then only relay bulk wave parameters via satellite. Continuing to report the full $1Hz$ data every 10th profile would then allow the full spectral information to be retained with the same frequency as the current setup, while drastically increasing the number of bulk parameter measurements.

Additional improvement of the quality of the EM-APEX float could potentially be achieved via the reduction in noise from the electrode voltage fitting procedure. This procedure currently sets a noise-floor on the significant wave height measurements of about $0.6m$, and the only way to be able to measure smaller waves would be through improvement of this fitting algorithm. Future work improving the fitting algorithm and validating directional wave estimates would be extremely valuable to this instrument's use as a wave-measuring platform.

2.7 Conclusion

Overall, this study validates the use of EM-APEX floats for wave-measurements, with good agreement of reported bulk parameters with other in-situ wave measuring platforms across a range of ocean conditions, as well as accurate measurement of 1D energy-density spectra in the band from approximately $0.05 - 0.2Hz$. This demonstrates that these floats are capable of measuring swell and distinguishing swell energy-density peaks from wind-wave peaks. Future improvements in sampling parameters could both increasing the spectral range up to $0.3Hz$, and inclusion of this wave-measuring algorithm on-board during future deployments could drastically increase the temporal resolution from what is presented here. Bulk wave measurements are in good agreement with other in-situ wave measurements, with $R^2 = 0.76$ and $R^2 = 0.65$ for H_s and T_e respectively, and we find that the EM-APEX float is capable of accurately measuring $H_s > 0.6$ m. On the whole this work suggests that EM-APEX floats are thus a potentially useful tool for future studies investigating interactions between surface waves and ocean currents and sub-surface turbulence and mixing, and their wave-measuring capabilities should be considered when planning future campaigns studying surface-wave physics, especially surrounding currents varying near the inertial frequency, which EM-APEX waves have a long history of being used to study.

Chapter 3

AN EXPLORATION OF THE INFLUENCE OF NEAR-INERTIAL CURRENTS ON SURFACE WAVES

3.1 Abstract

Fluctuations in wind forcing at the ocean surface generate a resonant response in the ocean mixed layer, producing currents oscillating at close to the local inertial frequency. These near-inertial currents are a ubiquitous feature of the mid- and high- latitude oceans, but detailed studies of their impacts on surface-wave field properties are limited. This work presents results from a series of idealized modeling experiments to quantify the impact of inertial currents on surface wave properties. By varying the properties of surface waves and currents over a realistic parameter space, the differences between the impacts of steady vs. inertial currents can largely be explained by the non-dimensional parameter c_gT/L, where c_g is the wave group speed, and L and T are characteristic length and timescales of the rate of change of currents. As c_gT/L approaches infinity, the magnitude and spatial patterns of the anomalies induced by inertially varying currents approach the steady current case. For values of c_gT/L on the scale $O(5-50)$ the amplitude of the wave anomalies decreases, and spatial variability of the wave anomalies increase. Additionally the time variability of the currents induces a phase lag between the current orientation and wave anomalies. These results together suggest that 1) Impacts of inertial currents on surface waves are highly dependent on inertial period, wave properties, and current spatial scales, and 2) The resulting patterns of spatial variability in the wave field can be notably different than for steady currents of the same magnitude and spatial structure.

3.2 Introduction

Ocean currents have long been known to modify surface gravity waves, with both observational and theoretical research dating back to the mid 20th-century (Longuet-Higgins and

Stewart, 1964; Bretherton, 1969). However, recent research has revealed a previously unexpected level of spatial variability in the surface wave field at mesoscales $O(\sim 100km)$ and smaller, driven by the variability in the surface currents modifying surface waves Ardhuin et al. (2017). Subsequent modeling and observational analyses have indicated that a high degree of variability in surface wave heights and slopes exists at meso- and submeso-scales due to the influence of surface currents on surface waves (Villas Boas et al., 2020; Quilfen and Chapron, 2019; Vrećica et al., 2022; Iyer et al., 2022). Observational and modeling studies of this surface-wave modulation have largely been limited to steady or slowly varying (sub-inertial) currents, with some work considering how tidal currents modify surface waves (Gemmrich and Garrett, 2012; Ardhuin et al., 2012; Ho et al., 2023; Halsne et al., 2024).

Ocean surface currents contain significant energy in the frequency band surrounding the local inertial frequency (Arbic et al., 2022; Flexas et al., 2019). This kinetic energy is driven by changes in wind forcing which induce a resonant response in the mixed layer, with currents rotating at the inertial frequency to the right (clockwise) in the Northern Hemisphere and to the left (counterclockwise) in the Southern Hemisphere. As a significant pool of kinetic energy in the ocean, inertially varying currents are potentially an important source of variability in the surface wave field. While Gemmrich and Garrett (2012) demonstrated evidence of inertial currents impacting significant wave heights in buoys in the North Pacific, a lack of current measurements prevented a detailed analysis of the mechanisms of the influence of inertial currents on surface waves, or the extent to which these current may influence surface waves outside of that region. A gap in understanding exists surrounding the mechanisms and impacts of currents varying on timescales comparable to the inertial frequency on the surface wave field. One approach to addressing this gap could be to use observations of both waves and inertial currents, such as from instruments measuring both quantities, for example EM-APEX floats (Stadler et al., 2025) or SWIFT buoys (Thomson et al., 2019). Another, complementary method, is to take a modeling approach to investigate how varying inertial-current and surface-wave properties impacts wave-current interactions. This chapter takes the latter approach, seeking to explore through wave models how inertial currents may modify surface waves, and if the time-varying nature of these currents results in different behavior than would be expected if the currents were assumed to be steady.

3.2.1 Theory of wave-current interactions

The propagation of surface waves can be modeled with the wave action equation, as presented in equation 1.10 in Chapter 1 above Bretherton (1969):

$$\partial_t N + (\mathbf{U} + \mathbf{c_g}) \cdot \nabla N + \dot{k}\partial_k N + \dot{\theta}\partial_\theta N = S_{in} + S_{diss} + S_{nl}$$

$N(\mathbf{x}, t, k, \theta)$ is the wave-action of the surface wave field, defined as:

$$N(\mathbf{x}, t, k, \theta) = \frac{E(k, \theta)}{\sigma} \tag{3.1}$$

Where $E(k, \theta)$ is the energy density spectrum of the surface wave field, and σ is the intrinsic frequency of the surface waves. For deep water waves, $\sigma = \sqrt{gk}$ and $c_g = \frac{\sigma}{2k} = \frac{g}{2\sigma}$. For waves propagating over a surface current $\mathbf{U}$, the frequency observed by in a stationary reference frame is $\omega = \sigma + \mathbf{k} \cdot \mathbf{U}$. The wave action equation holds under the assumptions that $U \ll c_g$, $\frac{dU}{dt} \ll \sigma$, or when currents are much slower than the wave group speed and the time rate of change of currents is much smaller than the wave frequencies.

Ocean currents can modify surface waves through four main mechanisms: (1) Advection of Wave Action, (2) Wavenumber Shift, (3) Refraction, (4) Relative wind effect. The first three effects are a result of the 2nd, 3rd, and 4th terms on the left hand side of equation 1.10 respectively. These are intrinsic impacts of the currents on the surface waves themselves. The fourth effect (relative wind) is caused by the change in relative speed between the ocean surface and the wind, which enters into the equation by modifying the S_{in} source term. Extensive previous literature has investigated the impacts of slow-varying or steady currents on surface waves and found that refraction and the wavenumber shift are the dominant sources of current effects on waves (Ardhuin et al., 2017; Quilfen and Chapron, 2019; Villas Boas et al., 2020; Wang et al., 2025; Bôas et al., 2025). Conversely, recent work on the effects of currents on the wave field under hurricanes found that the advection term in the wave action equation was a dominant source of the impact on surface waves due to ocean currents (Papandreou et al., 2026). This work hypothesized that the main mechanism for this was the effect of advection by currents causing the waves to be transported out of the region of high-winds more quickly, reducing the ability of the hurricane wind field to input energy into the surface wave field. This does not contradict the previous work showing a higher importance of refraction, as those works largely considered wave-current interactions separate from the question of wind energy input.

These mechanisms are not in any way inherently different for currents that vary in time. However, for a wave packet passing through a region of temporally varying currents, the currents and current gradients that the wave packet encounters over its trajectory are dependent on the time variability of the currents. A common assumption is that given the group speed characteristic of deep water swell O(10m/s) and the timescale of meso- or submeso-scale current variability $O(days-weeks)$, that the impact of the real, time varying, surface currents in the ocean on surface waves is approximately the same as if any snapshot of currents was stationary in time (Villas Boas et al., 2020; Gemmrich and Garrett, 2012).

The relative change in ocean currents relative to the trajectory of ocean surface waves can be quantified with a non-dimensional parameter relating the wave speed (c_g), timescale of current variability (T_U), and characteristic length scale of the currents (L_U). I propose that the non-dimensional parameter:

$$c_g T_U / L_U = \frac{T_u}{(L_u/c_g)} = \frac{\text{Time it takes currents to rotate}}{\text{Time it takes waves to pass through currents}} \tag{3.2}$$

will characterize much of the deviation in differential impacts on surface waves between inertially varying currents and steady currents. There are many ways in which one can define a characteristic length and timescale, throughout this dissertation I will use the convention that L is defined as the e-folding scale of the surface current U, such that if a current is at a maximum at $U(\mathbf{x_0}, t_0) = U_{max}$, then $U(\mathbf{x_0} \pm L_U, t_0) = (1/e)U_{max}$. The timescale of current variability will be defined as the inertial period, T_i, of the rotating currents. Throughout this work this quantity will be referred to simply as $c_g T/L$. This can be thought of as the ratio of spatial to temporal changes in currents along a wave's path. Or, effectively, how far through the patch of currents a wave packet travels before the time rate of change of currents causes the currents to change significantly.

This parameter is not one that has been investigated with respect to surface wave - current interactions previously, but is similar to the parameter $\alpha = U_{rms} T_E / L_E$ that has previously been used for characterizing the differences between Lagrangian and Eulerian measurements of velocity spectra (Yu et al., 2019; Middleton, 1985). In this case, as c_gT/L becomes large the currents experienced by a wave packet increasingly approximate steady currents, and when c_gT/L approaches 0 a wave packet experiences increasingly variable currents as it crosses a region of inertially varying currents.

This research seeks to investigate the theoretical mechanisms by which near-inertial surface currents modify the surface wave field. This paper investigates the impact of inertially rotating currents on wave properties in a series of idealized wave models and attempts to answer the following questions:

1. How does varying inertial period, wave, and current properties impact the resulting wave-current interactions?

2. How do the resulting wave-current interactions differ from the case of steady currents? How the impacts of time-varying currents on waves best be generalized?

I hypothesize that there exists a parameter space of c_gT/L values where the amplitude and spatial structure of the resulting Hs anomalies differ significantly from what would be expected for steady currents. As c_gT/L increases towards infinity, I expect the Hs anomalies produced by inertial currents to approximate those produced by steady currents.

3.3 Methods

3.3.1 Idealized Model

in order to answer these questions, I implement a series of idealized WaveWatchIII (WW3) (WAVEWATCH III Development Group, 2019) models inspired by those in Villas Boas et al. (2020). To isolate the impacts of surface currents on surface waves and simplify the analysis, the source terms on the right hand side of equation 1.10 are neglected, removing the effects of wind-generation of waves, dissipation, and non-linear wave-wave interactions. The models are run over a $600km \times 600km$ domain in deep water, and waves are incident into the model domain from the western boundary and travel to the east. Waves are prescribed using an idealized Pierson-Moscowitz spectral form (Ewing and Laing, 1987):

$$E(f) = \frac{5}{16} H_s^2 f_p^4 f^{-5} \exp\left(-\frac{5}{4}\left(\frac{f}{f_p}\right)^{-4}\right) \tag{3.3}$$

And a 2D spectrum with the form

$$E(f,\theta) = E(f)D(\theta)d\theta \tag{3.4}$$

where $D(\theta)$ is a directional spreading function such that $\int_0^{2\pi} D(\theta) = 1$. Directional spreading is prescribed following a $D(\theta) \propto \cos^{2s}((\theta - \theta_p)/2)$ distribution. Here, s determines the directional spread of the waves, with large s corresponding to a very narrow directional spread and small s a very broad spectrum, and θ_p is the peak direction of the surface waves. Three different peak wave periods T_p were investigated, $T_p = [5s, 10s, 15s]$, and values of $s = 5$ and $s = 20$, corresponding to a directional spread of $\sigma_\theta \approx 33°$ and $\sigma_\theta \approx 18°$ respectively. The significant wave height Hs of the input waves can be chosen arbitrarily, but in order to simplify the analysis a constant value of $Hs = 2.5m$ is used throughout. Additionally, only waves propagating from west to east are considered, with $\theta_p = 270°$ (meteorological directional convention).

The models are run with and without a series of idealized current forcings (Fig. 3.1):

$$u(x,y,t) = -Ue^{-\frac{x^2+y^2}{L^2}} \cos(2\pi t/T_i) \tag{3.5}$$
$$v(x,y,t) = Ue^{-\frac{x^2+y^2}{L^2}} \sin(2\pi t/T_i) \tag{3.6}$$

Currents are prescribed a Gaussian structure in the x and y dimensions centered at the middle of the model domain, with the e-folding scale taken to be the characteristic length scale L of the currents. These currents are defined such that the phase of the inertial currents $\phi = 2\pi t/T_i$ corresponds with the following directions:

$$\{(\phi = 0 : \text{West}); (\phi = \pi/2 : \text{North}); (\phi = \pi : \text{East}); (\phi = 3\pi/2 : \text{South})\}$$

These currents are characterized in terms of a few parameters, the length scale L, the maximum current amplitude U, and inertial period T_i, and can be tuned to test how waves respond to each of these characteristics. The model takes approximately 4 days to spin-up to a steady significant wave height, which is to say that after 4 days the waves input from

Table 3.1: Parameter space of WW3 model runs. Each model run uses one value from the list of options for each parameter. Additionally, for each wave period a control model-run with no-currents to calculate the anomalies.

Parameter	Modeled Options
Inertial Period (T_i)[hrs]:	[4, 8, 12, 24, 36, 48, 96, 288, 576]
Wave Current Interaction Terms:	[advection, k-shift, refraction, all]
Peak Wave Period (T_p)[s]:	[5, 10, 15]
Corresponding Wave Group Speed (c_g)[m/s]:	[3.9, 7.8, 11.7]
Wave Directional Spreading (°):	[33, 18]
Max Current Amplitude (U)[m/s]:	[0.2, 0.5]

the western boundary have propagated across the domain. The model is then run for 17 days for all model runs expect for the $T_i = 576hr$ run, which is run for 30 days, in order to ensure greater than one full inertial period for each model run.

3.3.2 Model evaluation metrics

The analysis in this work is restricted to the significant wave height (Hs) of the wave field. This bulk wave parameter is defined as in equation 1.4:

$$Hs = 4\sqrt{\int E(f)df}$$

In order to characterize the effects of the currents on the surface waves, at each grid cell the anomaly between any given run with currents and a model run with the same wave forcing but without currents, is calculated. For example, the significant wave height (Hs) anomaly for a given run is defined as the difference between the current and no-current runs:

$$Hs' = Hs_{cur} - Hs_{nc} \tag{3.7}$$

and the percent change in Hs caused by the wave-current interactions:

$$Hs'(\%) = 100 \times \frac{Hs'}{Hs_{nc}} \tag{3.8}$$

Here, Hs_{cur} is the output field from a given model run with currents, and Hs_{nc} is the corresponding control run without current forcing. The anomalies for other wave parameters (e.g. mss, T_m, etc) can be calculated in the same manner.

The spatial variance of the wave field is then defined as

$$Var = \frac{\sum_{i,j}(Hs'(x_i, y_j) - \langle Hs' \rangle)^2}{N} \tag{3.9}$$

Thus for each model run this variance is a function of time, and can be used as a bulk metric to quantify the overall impact of currents on the spatial variability the surface wave field.

Additionally, the WaveWatchIII modeling framework allows for the terms in the left-hand side of equation 1.10 to be selectively turned on/off (WAVEWATCH III Development Group, 2019). Since the Advection term must always be on in order for the waves to propagate across the model domain, separate models are run with the terms 1.) Advection, 2) Advection + wavenumber-shift, 3) Advection + Refraction, 4) All terms. Anomalies for each are then defined as:

$$\begin{aligned}
Anom_{advec} &= Hs_{advec} - Hs_{nc} \\
Anom_{k} &= Hs_{advec+k} - Hs_{advec} \\
Anom_{ref} &= Hs_{advec+ref} - Hs_{advec} \\
Anom_{all} &= Hs_{all} - Hs_{nc}
\end{aligned}$$

Where $Anom_{advec} + Anom_k + Anom_{ref} = Anom_{all}$.

The relative contribution of each term in the wave action equation is quantified by comparing the covariance of each term and the overall anomaly:

$$Contribution(\%) = 100 \times \frac{\mathrm{Cov}(Anom_i, Anom_{all})}{\mathrm{Var}(Anom_{all})} \tag{3.10}$$

In order to characterize the relative isotropy/anisotropy of the wave anomaly driven by inertial currents, the aspect ratio of characteristic x and y length scales of the resulting wave field. Here I make use of the definition of the aspect ratio λ_x/λ_y used in (Wang et al., 2026):

$$\left(\frac{\lambda_x}{\lambda_y}\right)^2 = \frac{\langle(\partial_y Hs)^2\rangle}{\langle(\partial_x Hs)^2\rangle} \tag{3.11}$$

Where $\langle\cdot\rangle$ is the spatial average over the whole model domain. Values of $\lambda_x/\lambda_y > 1$ correspond to an anisotropic wave-field that has longer wavelengths in the x-direction than in the y-direction. While this is not the only way to characterize the relative isotropy of the Hs', it is chosen here for easy comparison with (Wang et al., 2026).

3.4 Results

3.4.1 Qualitative impacts of rotating currents on Hs anomalies

After the initial transient spin-up period, the wave field during the inertial current model runs oscillates infinitely between a set of recurring states at the same frequency as the currents driving the wave-current interactions. However, at any given point in time in the inertial run model output, the properties of the modified Hs field in the inertial-current runs differ from when a model is run with steady-currents in the same direction. Some of the main differences are (1) the amplitude of Hs modification by the surface currents generally increases as T_i increases, (2) the spatial pattern of Hs includes both a “local” response confined to the region of the currents and a “remote” response, which change in structure as T_i increases, (3) the relationship between current direction and Hs amplification/reduction at any given point in space and time changes with T_i, and (4) the remote wake includes an oscillatory component with radial wavelength $c_g T_i$ in the wave propagation direction (east–west). These results can be seen in figure 3.2, where each column corresponds to a snapshot of a different phase of the inertially rotating current. This figure can provide a strong qualitative understanding of the impact of the time-varying nature of the inertial currents when compared to the steady current case. Additionally, as may be expected, the response to currents during the East-West and North-South phases of the inertial currents are largely symmetric, with $H_{s,east} \approx -\Delta H_{s,west}$. As T_i increases towards infinity, the spatial pattern of the ΔHs response converges toward the steady case. This figure is shown for a spreading coefficient of $s = 5$, but similar qualitative results are found for the higher spreading function $s = 20$.

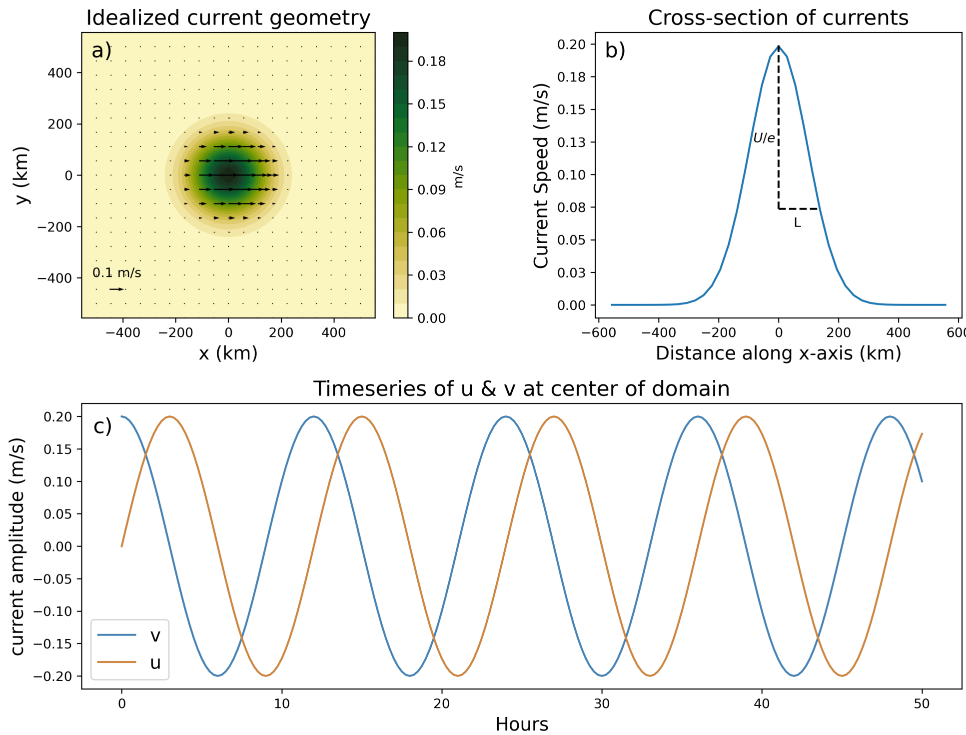

Figure 3.1: Overview of an example of the inertial currents used to force wave models. a) Shows a map of current amplitude and direction during the phase of the inertial currents when the currents are to the east. b) Shows the Gaussian spatial structure of the current amplitude along the x-axis. c) Timeseries of velocities (u, v) at the center of the domain, showing the rightward rotation the inertial currents. In this case the inertial period T_i is set to $12hrs$, the maximum amplitude of the currents is $0.2m/s$, and the characteristic length scale L of the currents is $100km$.

The differences in amplitude and spatial pattern of the Hs' field between a steady and inertial run can be more directly observed by comparing a model run with $T_i = 24hrs$ and a model with steady run. Comparing Hs' along cross sections of the the x and y axes during different current directions (e.g. west, north, east, south) reveals the impact of changing T_i on the amplitude, spatial pattern, and the phase relationship between the current direction and Hs'. This comparison is shown in figure 3.3, where comparing panels (a) to (b) and (c) to (d), the maximum change in Hs decreases from 4% to 3% as the currents transition from steady to oscillating. Additionally, the oscillation of the currents results in a shorter wavelength of the response compared to the steady case, or in other words a greater number of peaks and troughs of the Hs' signal in the model domain. The difference in phasing between Hs' and the current direction can also be observed by comparing panel (a) and (b). In the steady case, when currents are to the west, $Hs' > 0$ everywhere along the x-axis. However, when T_i = 24hrs and currents are to the west, $Hs' < 0$ over a large portion of the center of the domain. This suggests that the time-rotation of the inertial currents changes the expected instantaneous relationship between Hs' and the surface current direction relative to wave direction. A final observation is that there is a relative change in how isotropic the Hs' field is between the steady and inertial current cases. In figure 3.3 the steady run here demonstrates with a longer wavelength in the Hs' response along the x-axis than the y-axis, while in the inertially varying case the wavelengths of the response are similar along the x and y axes, and the resulting variability in the wave field is more isotropic than in the steady current case.

3.4.2 Amplitude and phase of the Hs response

When each model run is characterized in terms of the parameter $c_g T/L$, the relationship between this characteristic parameter and the amplitude and spatial patterns of the resulting wave field can be investigated. Our model runs span this parameter space from $0.6 \rightarrow 300$.

One way to characterize the overall impact of the currents on the wave field is the maximum Hs anomaly induced by the currents. The model results indicate that for a fixed directional spreading (say $s = 5$), the maximum Hs' induced by the currents is a function

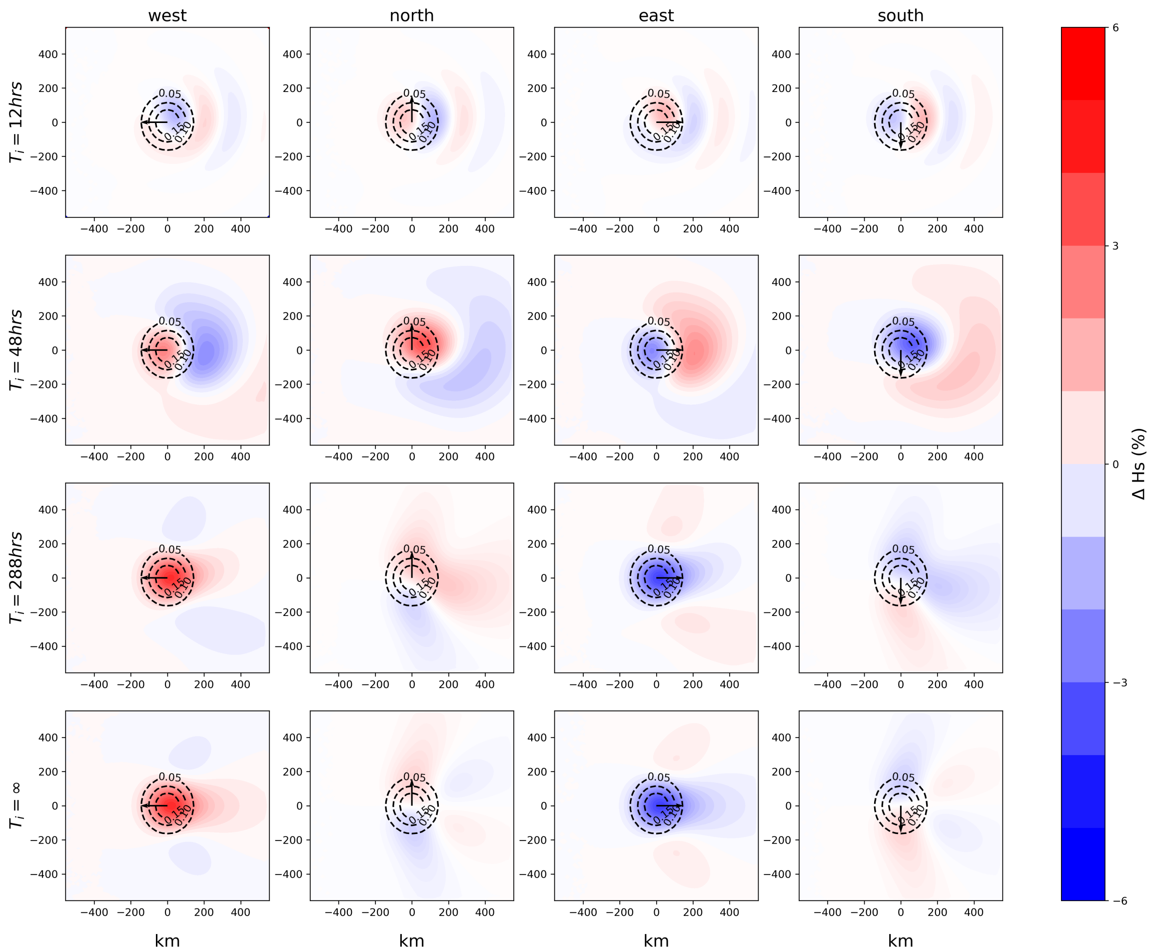

Figure 3.2: Impact of inertially rotating surface currents for three different inertial frequencies, and steady currents. Here all model runs use a current length scale $L = 100km$, magnitude $U = 0.2m/s$, and peak wave frequency $T_p = 10s$, and directional spreading coefficient $s = 5$. Top row, $T_i = 24hrs$, second $T_i = 48hrs$, third $T_i = 288hrs$, and last row steady currents ($T_i = \infty$). Each column corresponds to a different phase of the inertially rotating currents, labeled by the direction of currents. Contour lines indicate current speed, and black arrow the current direction. For steady currents, each column corresponds to an independent model run with the currents held constant in the orientation shown. Thus the anomaly shown for the steady current runs is a steady state. Note as the inertial period increases, the magnitude of ΔHs

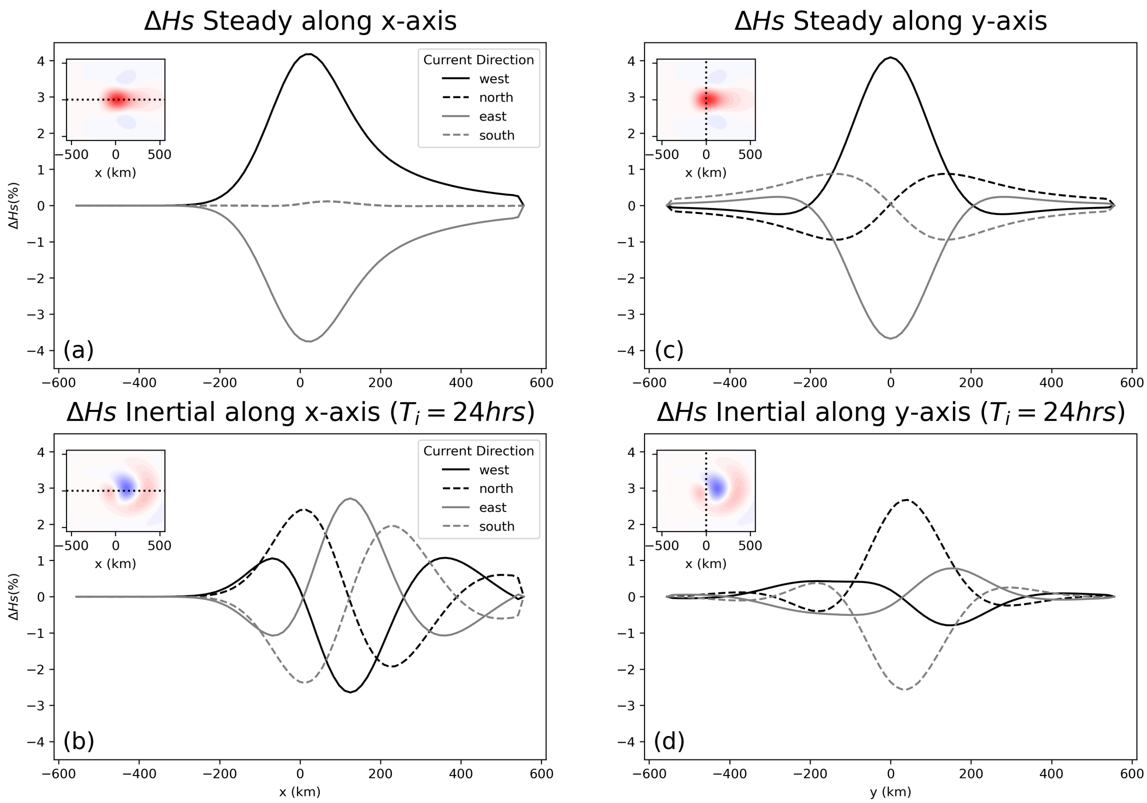

Figure 3.3: Cross sections of ΔHs across the x (a, b) and y (c, d) axes. Panels (a) and (c) show cross sections for steady current runs and (b) and (d) for an inertially rotating current run with $T_i = 24hrs$. Different lines correspond to different current directions. For the inertial current run (b,d) these are different phases of the inertial current as it rotates clockwise. For the steady run (a,c), each line corresponds to a different model run with the current held constant at the given direction throughout. Note that panel (c) exhibits symmetry along the y-axis around $y = 0$ due to the symmetry of the currents. However, panel (d) is not symmetric around $y = 0$, due to the clockwise rotation of the currents in time.

of U/c_g and c_gT/L. Larger values of both U/c_g and c_gT/L result in larger wave height anomalies. Since U/c_g is not impacted by the inertial rotation of the currents, its effect can be removed by normalizing inertial model output by steady current runs with the same value of U/c_g. For low values of c_gT/L, this ratio ($Max[Hs'_i]/Max[Hs'_s]$) approaches zero, and as c_gT/L increases towards infinity asymptotes to 1. Both these effects are highlighted in figure 3.4. Panel 3.4(a) shows the maximum anomaly for different inertial current runs with $U = 0.2$ m/s and $s = 5$, with larger values of both U/c_g and c_gT/L resulting in larger Hs anomalies. The dashed horizontal lines corresponding maximum Hs' for steady runs for a given value of U/c_g, and for each value of U/c_g the inertial current runs approach the maximum value of the steady runs as c_gT/L increases. This can be seen more clearly in 3.4(b), where normalization of $Max[Hs'_i]$ by the corresponding steady current run results in all the inertial current runs collapsing onto the same curve that asymptotes to 1. Isolating out just the model runs with a higher spreading function $s = 20$ (more narrow banded swell) shows a similar trend, as shown in figure 3.5. The tighter directional spread of these model runs increases the overall magnitude of the Hs' response, but does so equally as much in the inertially varying and steady runs, resulting in the collapse of all model runs onto one curve in figure 3.5 (b).

While the $Max[Hs']$ metric captures the maximum impact of currents on waves at a single point in space, it does not capture any information about the overall variability of the wave field in both time and space caused by the inertial currents. In order to make a more holistic assessment of the impact of inertial surface currents, the variance of Hs' anomaly is investigated. For currents that are steady, Hs' variance over the entire domain is maximized when currents are opposing or following the wave direction, with the variance minimized when currents are perpendicular to the wave-direction (figure 3.6(a), gray stars). However, as c_gT/L changes, the relationship between the Hs' variance and inertial-current direction changes. The variance across all model runs exhibits a periodic response at the inertial frequency, but the current phase at peak variance shifts with c_gT/L. For some small values of c_gT/L, the variance is maximized when current directions are approximately perpendicular to the wave direction. For a fixed c_g and L, as inertial period increases, the timing of maximum variance in the inertial period becomes increasingly aligned with when the currents oppose the waves. This is demonstrated in figure 3.6 (a), showing the variance for a set of model runs as a function of the inertial current phase (direction), where 0 corresponds with currents to the west, $\pi/2$ to the north, and so on. The currents corresponding to each phase are shown in 3.6 (b). Each color in panel (a) corresponds to a different inertial period for runs with $c_g = 15m/s$ and $L = 100km$, and the gray stars correspond to the variance from model runs with steady currents. Across all model runs, this phase difference between the direction of currents at maximum variance is largely a single function of c_gT/L (fig. 3.6(c)), maximizing around a value of $c_gT/L \sim 5$, and decreasing as $c_gT/L \rightarrow \infty$.

In addition to change in the direction of currents at peak variance, the magnitude of the peak variance and the amplitude of the variance response (half of the peak-to-peak of the variance response in figure 3.6(a)) also change with c_gT/L. Additionally, both the peak variance and the amplitude of the oscillation of the variance in time respond to changes in c_gT/L, appearing to have a similar sigmoidal structure as the peak Hs' in figure 3.4, although exhibiting different rates of approaching the expected values from the steady current case. The maximum variance more quickly approaches the steady value as c_gT/L increases, while the amplitude approaches the steady current amplitude much more slowly. This means that for values of c_gT/L in the range of approximately $1 - 10$ the average variance of Hs' over a full inertial current phase is higher in the inertial current runs than the average variance over a full inertial cycle of steady current runs.

3.4.3 Spatial Structure of Hs response

In addition to modifying the overall variance of the Hs field, the inertial currents modify the spatial patterns of the resulting Hs. This can be observed qualitatively in figures 3.2 and 3.3. The spatial structure and variability of Hs' is assessed through three primary methods. The first is to quantify this spatial variability is through the magnitude of the gradient of Hs', $\|\nabla Hs'\|_{rms}$. This method has been used in previous wave-current interaction studies as a method for quantifying spatial variability (Villas Boas et al., 2020; Marechal and Ardhuin, 2021). Figure 3.7(a) presents $\|\nabla Hs'\|_{rms}$ normalized by the gradient from the corresponding

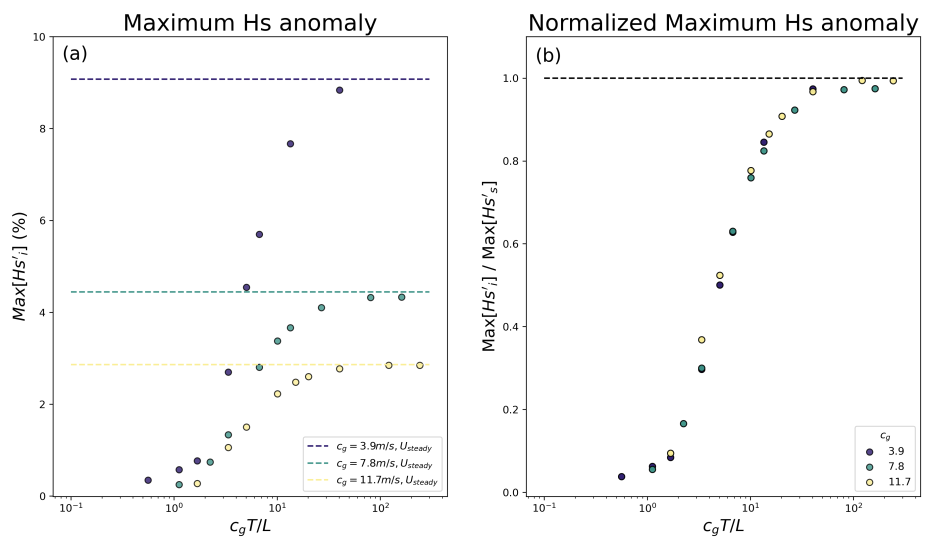

Figure 3.4: (a) Maximum Hs' for each run as a function of c_gT/L for model runs with $U = 0.2m/s$. Points are colored by the peak wave frequency of each run. Maximum anomaly increases as wave speed decreases, or as U/c_g increases. Horizontal dashed lines are maximum Hs' for corresponding steady current runs. Note that the inertial runs approach the steady maximum as c_gT/L increases. (b) Maximum Hs' normalized by the maximum from the corresponding steady run, thus controlling for the U/c_g dependence.

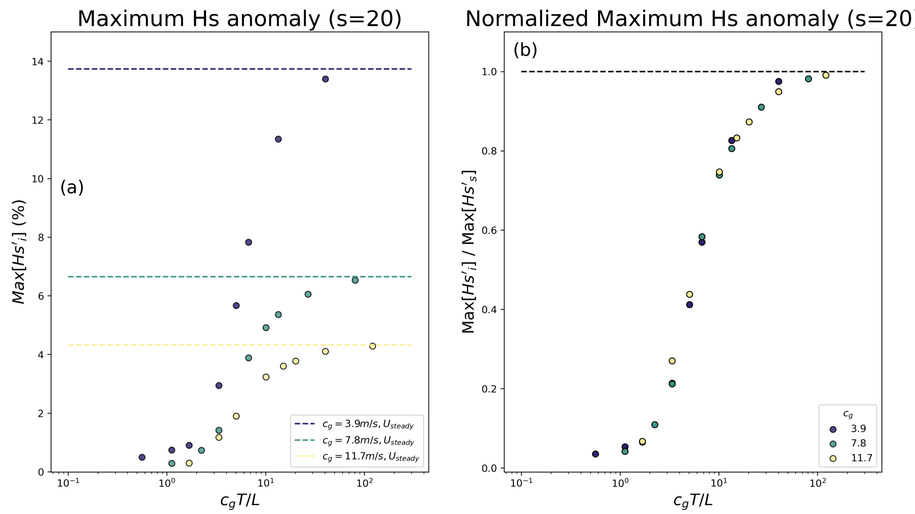

Figure 3.5: (Same as figure 3.4 above, except for a more narrow banded wave spectrum, with $s = 20$ spreading coefficient. Note the increase in overall magnitude of the response in panel (a) relative to spreading coefficient $s = 5$.

steady run across all model runs as a function of c_gT/L. For values of c_gT/L on the order of $1 - 10$, the model runs forced with inertial currents demonstrate elevated wave-height gradients, and therefore spatial variability, when compared to the steady run cases. This corresponds with the observation that patches of increased and decreased Hs in figure 3.3 appear to greater spatial variability in the inertial runs than the steady runs.

Figure 3.7(b) presents another viewpoint of the spatial variability of the wave field, comparing the aspect ratio of Hs' in the x and y directions, as defined in equation 10. Steady currents have been known to tend to produce patterns in Hs anomalies elongated along the axis of wave propagation, or the x-axis in this case. However, in figure 3.7(b), a large parameter space of c_gT/L demonstrates maximum aspect ratios well below the expected values from the steady current runs, and aspect ratios < 1 for values of $c_gT/L \sim 1$. This suggests that inertial currents can result in Hs' structures that are more elongated in the cross-wave direction than steady currents. It's worth noting as well that around $c_gT/L = 10$ the inertial-current runs have larger aspect ratios, and exhibit structures with

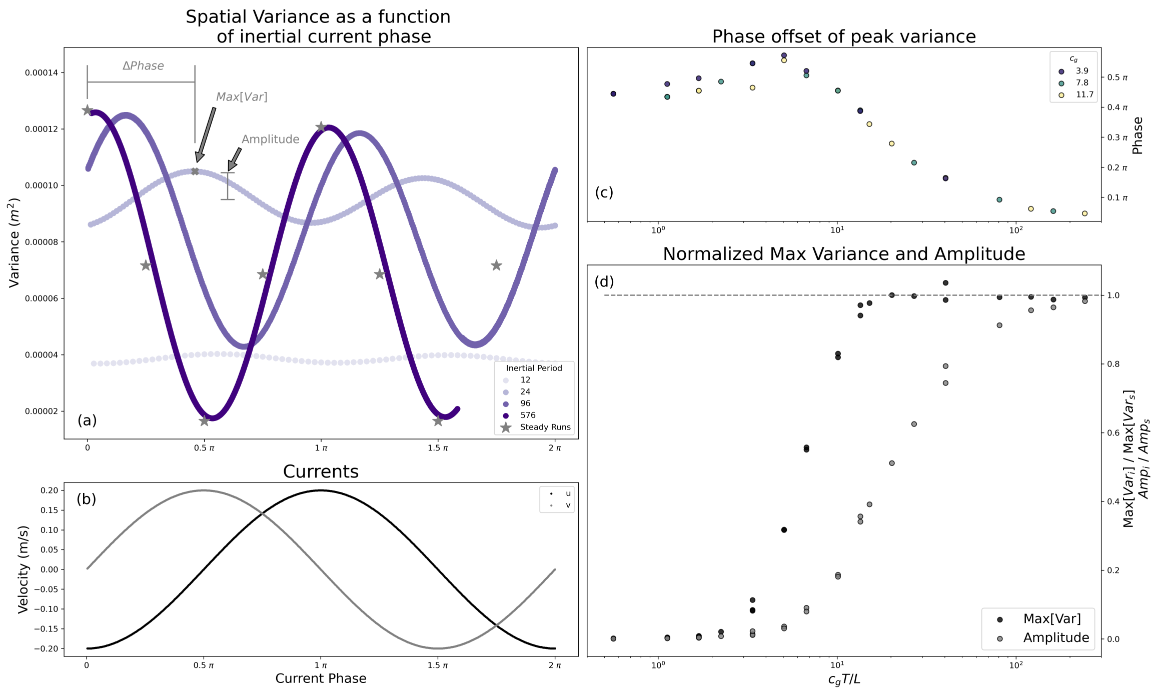

Figure 3.6: (a) Spatial variance of Hs' as a function of inertial current phase for a series of inertial current runs with varying T_i. For the runs shown here, $c_g = 15m/s$ and $L = 100km$. Definitions of metrics used for analyzing this variance response, the phase shift between peaks, maximum variance, and amplitude of the response, are indicated. (b) Magnitude of currents as function of inertial phase, defined as clockwise rotating with phase=0 corresponding to currents to the west. (c) Impact of c_gT/L on shift between current phase at maximum variance for inertial runs and steady runs. (d) Impact of c_gT/L on both normalized maximum variance (black circles) and normalized amplitude (gray circles). Each model run is normalized by the value from steady runs with the same c_g, L, and U.

longer wavelengths in the along-wave direction than the steady cases. Altogether, this suggests that the aspect ratio of the resulting Hs' structures is highly dependent on c_gT/L.

A third method of assessing the spatial patterns of the Hs' response to inertial currents is to compare the Hs' variance in different regions of the model domain. Figure 3.8 does this by comparing the variance between steady and inertial runs in two regions. The first, dubbed the "local" region is defined as the area of the model domain with currents $> 5\%$ of the current maximum. The second, the "remote" region, is everywhere with currents below that threshold. Figure 3.8(b) shows the normalized maximum variances for each of these regions. The local (inside black contour) region exhibits behavior similar to what was observed in figure 3.6(d) for the overall domain. However, in the "remote" region where currents are weak, the inertial show much greater Hs' variance than the steady runs between $c_gT/L \approx 1$ and $c_gT/ \approx 10$. Therefore, for runs within this range of c_gT/L, the inertial currents increase the variance in the wave-field down-stream of the currents interacting the waves.

3.4.4 *Impact of different wave-current interaction terms*

To investigate further the differences between the Hs response to inertial currents vs. steady currents, the relative contributions to the overall anomaly of the different terms in the wave action equation are interrogated. In figure 3.9 we show a few sample anomaly maps for a range of different values of c_gT/L when currents are to the west. Qualitatively, as c_gT/L increases the wave-current interaction term which dominates the overall anomaly shifts. While the advection and k-shift terms dominate for small values of c_gT/L (first two rows), at larger values the importance of the refraction term increases.

Figure 3.10 shows the relative importance of each term to the overall variance as a function of c_gT/L. At low values of c_gT/L, the advection term dominates the wave current interaction effect at all phases of the inertial currents, whereas refraction makes up either either a small or negative contribution to the overall Hs anomaly. This dominant component shifts around $c_gT/L = 5$ for the westward/eastward velocities and $c_gT/L = 3$ for the northward/southward velocities. The k-shift term never dominates the overall anomaly, but makes up a significant contribution $O(50\%)$ when c_gT/L is of order 1. At high c_gT/L

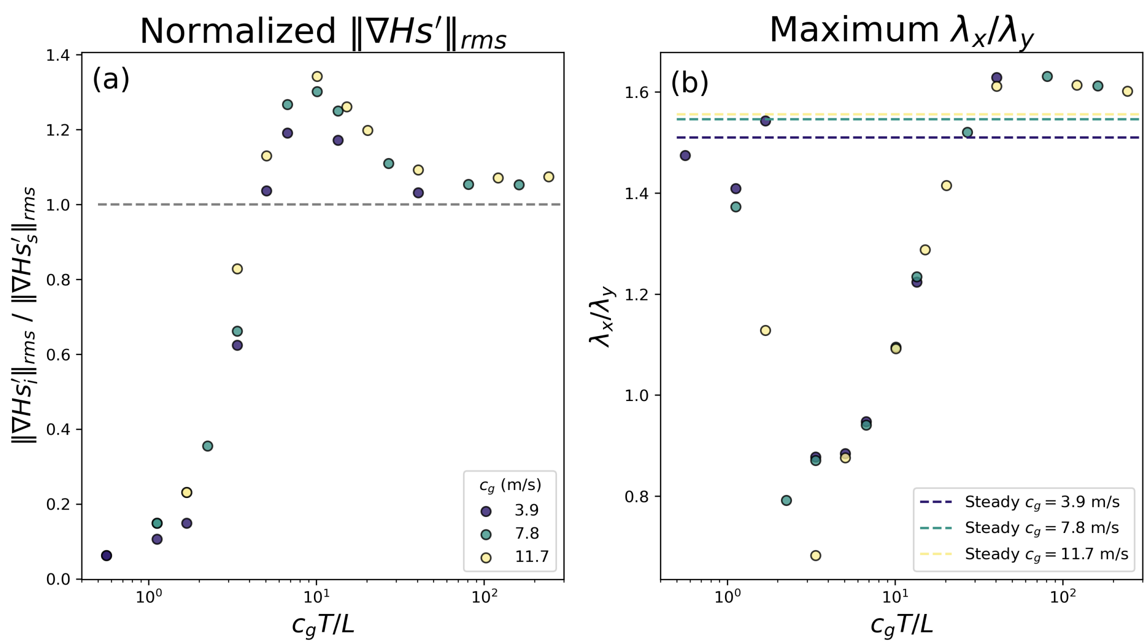

Figure 3.7: (a) Root-mean squared (RMS) Hs_i' gradients normalized by the RMS Hs_s' gradients from steady runs. Horizontal dashed line indicates when the magnitude of RMS gradients from the inertial and steady runs match. (b) Maximum aspect ratio of Hs' from each inertial run. Horizontal dashed lines indicates the maximum value obtained for steady runs with different peak wave group speeds.

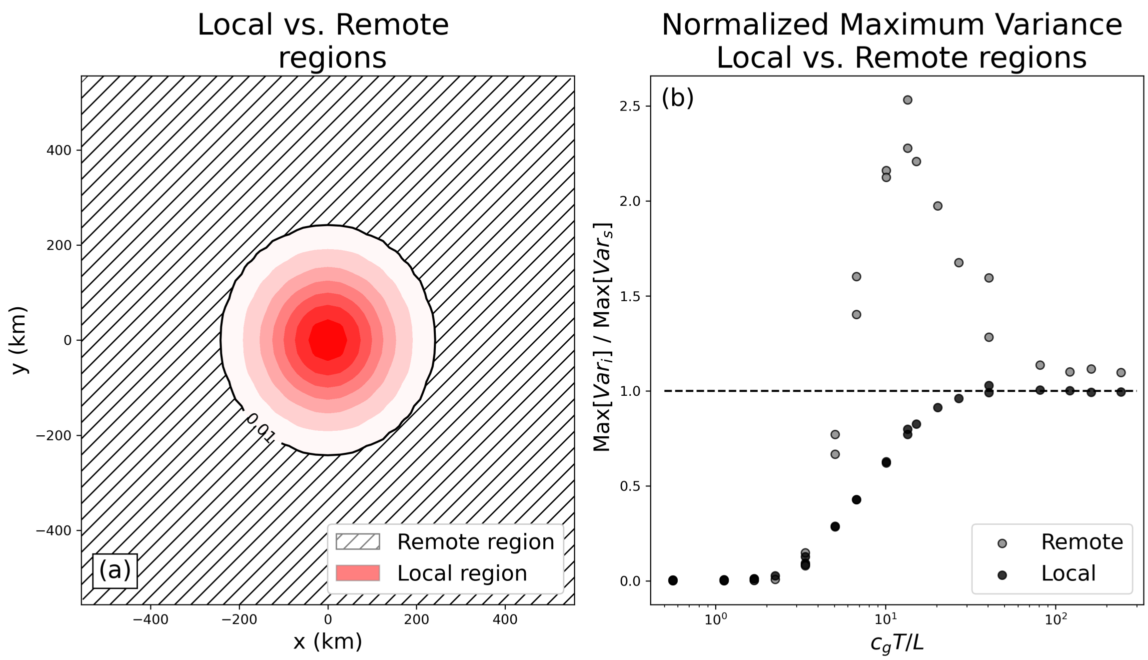

Figure 3.8: Comparison of the local and remote impacts of currents on Hs variance. (a) Definitions of local and remote regions in our modeling setup. Inside the black $0.01m/s$ contour is defined as the region where current effects may be considered to be local. Outside the contour in the hatched region, there are no significant currents (<5% the maximum value), and variance of surface waves in this region may be considered to be generated remotely by currents upstream of a given location. (b) normalized peak variance for all model runs in the local (black) and remote (gray) regions.

the refractive term dominates, and the relative contributions of each term to the overall variance approach the steady case. The snapshots of Hs during phases of inertial currents that are perpendicular to the wave direction do not approach the steady case values as quickly in c_gT/L space as when the currents are following/opposing the waves.

3.5 Discussion

This work shows that the time variance of inertial currents can result in modifications to the mechanisms and resulting features of current-driven wave anomalies when compared with steady currents of the same magnitude, spatial structure, and orientation. When wave a wave packet passes through a current patch, if the currents are changing in time then the greater the rate of change of the currents the larger the difference in currents experienced by the wave packet along it's Lagrangian trajectory from what it would experience if the currents were invariant in time. The resulting patterns of advection, refraction, and changes in wavenumber that cause the currents to modify the waves in equation 2.1 are thus modified once the currents are allowed to vary in time. As currents change more slowly the currents that waves experience become increasingly similar to what they would experience if the currents were steady in time. This results in the patterns of wave-current interaction approaching what might be expected from steady currents as the inertial period increases towards infinity.

Our results show that the time variance of currents influences many aspects of the wave response to currents, including diminishing the maximum magnitude of wave-current interactions (figure 3.4), changing the relative direction between waves and currents during maximum Hs' variance (figure 3.6), and modifying the spatial variability and aspect ratio of the Hs field (figure 3.7). Importantly, the differences between the anomalies driven by inertial and steady currents often appear the most significant in the parameter range $5 < c_gT/L < 50$. This parameter range happens to correspond to realistic values of c_g, T and L for inertial motions, suggesting that these effects may be important in the real ocean. For example, in the mid-latitude ocean near $40 - 50°$, Etienne et al. (2025) showed that decorrelation length scales of inertial motions, defined similarly to our definition of L here, are on the order of $100km - 200km$. Previous work estimating the magnitude of inertial

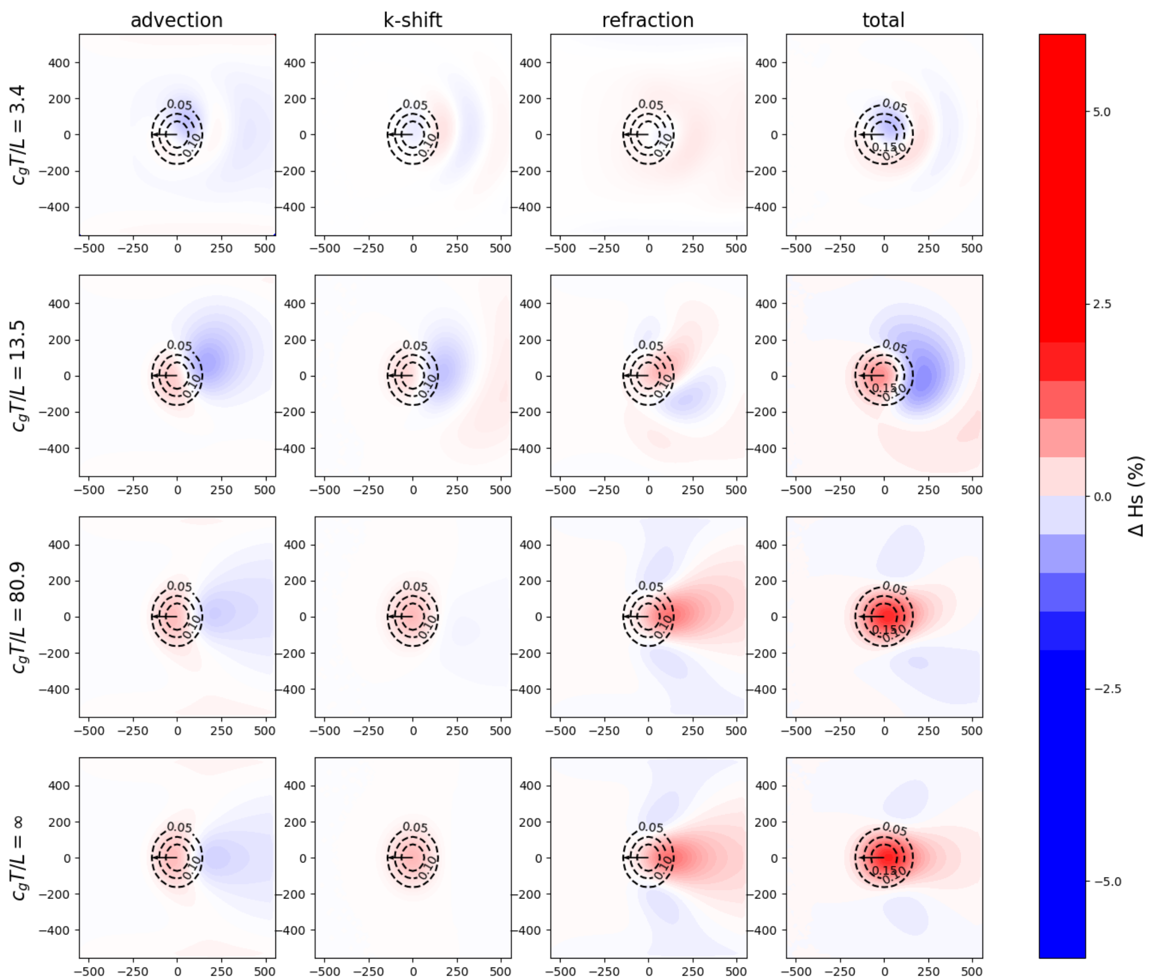

Figure 3.9: Hs anomaly (%) due to each term in equation 2.1 (columns 1-3), and with all terms (column 4). Each row represents a model run with a different inertial period f. These models are all forced by waves with $T_p = 10s$ and currents with $L = 100km$.

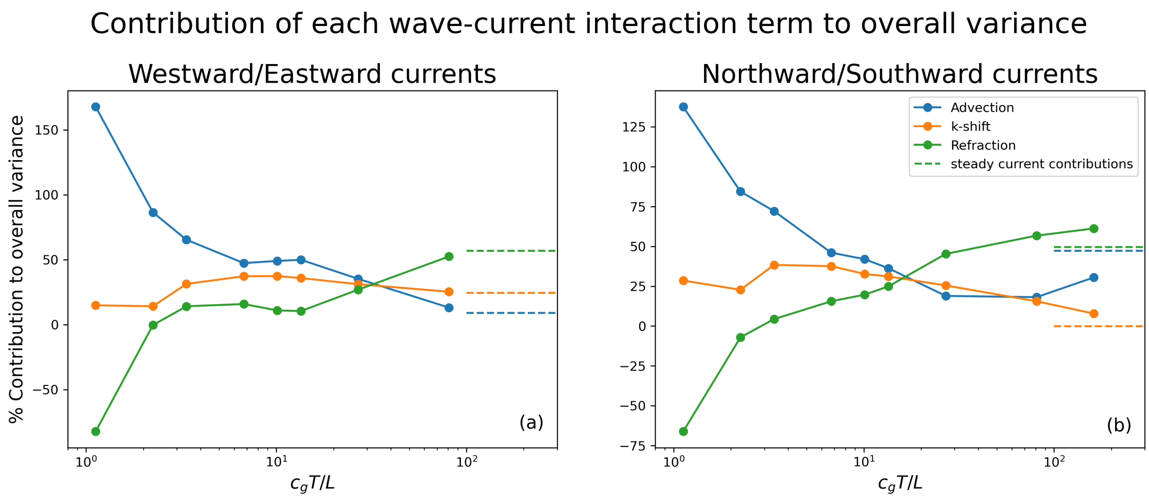

Figure 3.10: Relative contribution of each term in the wave-action equation to the overall variance. (a) For snapshots of the model output when currents are to the West and East, and (b) for when currents are to the North and South. Dashed lines show the relative contribution of each term for a model run forced by currents that are steady.

currents has shown that globally at mid-latitudes near inertial motions can make up to 30% of overall surface kinetic energy (Flexas et al., 2019). For a common wave period of $10s$ at $45°N$ with inertial motions having a length scale of $100km$, this would correspond roughly to a value of $c_gT/L \approx 5$. Thus, based on the results presented here one might expect the impacts of inertial currents on waves to be significantly different from the impact of steady currents, both in terms of the spatial patterns of the response and the instantaneous phase relationship between wave enhancement and current direction. While some previous work has found relationships between instantaneous velocities opposing waves and increases in wave height and wave slopes in conditions where currents are slower varying (Iyer et al., 2022; Marechal and Ardhuin, 2021), the runs shown here with c_gT/L values on the order of 5 often show large regions where instantaneous velocity is opposing the waves but Hs decreases (figure 3.6c). This suggests that instantaneous relationships between inertial current and wave directions should not necessarily be assumed to be uniformly correlated with wave enhancement, and that this relationship changes with c_gT/L—as well as the sum of variable currents along a wave group trajectory.

Previous work has shown that an important result in wave-current interactions is the anisotropic Hs field that results from refraction, with the current driven variability having longer wavelengths in the along wave direction (Wang et al., 2025; Bôas et al., 2025). This has been shown both in idealized models as well as in observations from the SWOT satellite. Our work suggests that in regions and times of the year with frequent inertial surface currents these currents may result in a less isotropic wave field, or even an Hs field with longer wavelengths of Hs anomalies in the cross-wave direction. The contrast arises from the ratio of the local current effect to the radiating impact pattern, as well as the shortened spatial scale of the radiating Hs' pattern in the down-wave direction for smaller values of c_gT/L, which can be observed in figure 3.2.

Additionally, due to the lower importance of the refraction at values of approximately $c_gT/L < 50$, it's likely that ray-tracing approaches to investigating wave-current interactions would not correctly predict spatial patterns or magnitudes of Hs variability from inertial currents. Due to typical spatial decay scales of inertial currents and the sensitivity of the Hs variability to both the spatial structure of the currents and the wave frequencies, making accurate predictions of the impact of more realistic inertial currents likely will require forcing a full third generation wave model, such as WaveWatchIII or SWAN, with currents with high resolution in both space and time. This presents a challenge to including the potential effects of inertial currents in operational forecast models, as existing satellite altimeter based current products do not resolve inertial currents. One option is to use an operational ocean circulation model, such as HYCOM, to provide forcing to an wave model. However, models such as HYCOM have been shown to have a varying degree of accuracy in correctly estimating the surface ocean kinetic energy at the inertial frequency Arbic et al. (2022). Future study investigating the ability of wave models forced by currents from operational ocean models to accurately capture wave variability driven by inertial currents is warranted.

One limitation of this study is that all model runs presented here have the dissipation terms on the right hand side of 1.10 turned off. The choice has been made in previous modeling studies on current impacts on Hs, but means that in these model runs wave breaking and dissipation does not removing energy from the wave-field in a realistic way.

A few test runs were performed with these terms turned on, and results appeared largely unmodified by turning on the dissipation terms in the wave action equation. However, it may be beneficial for future analyses to include the impacts of wave-breaking and dissipation, as this would allow the analysis to be extended to wave properties more dependent on the higher-frequency end of the wave spectrum than Hs, such as how these inertial currents may impact wave slopes.

3.6 Conclusion

This work has sought to investigate how the time variability of inertially rotating currents, a common feature of the global ocean, might impact ocean surface waves. By interrogating a series of idealized wave models with varying inertial frequency, current spatial scales, and wave spectral properties, the differences in wave-current impacts between steady and inertially varying currents are found to be largely characterized by the parameter $c_g T/L$. On the whole, increasing the time variability of currents decreases the amplitude of the Hs response of waves to surface currents, increases the spatial variability of the wave field, and changes the physical terms in the wave action equation that dominate the wave-current interactions.

Chapter 4

OBSERVATIONS OF THE IMPACT OF INERTIAL CURRENTS ON SURFACE WAVES: TWO CASE STUDIES.

4.1 Abstract

Inertial currents are one of the most common forms of ageostrophic motion in the ocean surface layer. This work investigates the impact of these currents on surface wave significant wave heights and mean squared slopes at two locations, Ocean Station Papa in the Gulf of Alaska and Astoria Canyon off the Oregon Coast, with concurrent wave and current measurements. Over 5 and 4 years of data at each location respectively, inertial currents drive on average $\sim 2-3\%$ modulations in Hs and $\sim 3-4\%$ modulations in mss, with frequent occurrences of modulations 2-3 times that in magnitude. Additionally, investigating the phase relationship between wave-relative inertial current directions and Hs and mss modifications, reveals that following currents tend to correspond with increases in Hs but decreases mss at both locations, while opposing currents decrease Hs and increase mss. These results for Hs are counter to classic examples of waves propagating into an opposing/following current, and although this result has been previously observed in some cases of tidal currents, this is the first observational evidence of the relationship between the relative direction between inertial currents and surface waves and the resulting wave modulation.

4.2 Introduction

Changes in wind stress at the ocean surface can generate a resonant current response in the upper ocean (Pollard and Millard, 1970; Pollard, 1970; Gill, 1982). The resulting currents, known as inertial currents or inertial oscillations, tend to rotate clockwise in the northern hemisphere and counter clockwise in the southern hemisphere (Gold, 1908). These currents have been found to be one of the largest pools of ageostrophic motions in the ocean surface layer, making up approximately 10% of total mixed layer kinetic energy when analyzed in both global observational drifter networks and numerical models (Arbic et al., 2022; Flexas et al., 2019; Yu et al., 2019). Two important characteristics that distinguish near-inertial motions from other forms of ocean current variability are 1) their relatively short timescales, varying from 12 hours at the north pole to 35 hours at 20°, and 2) their anticyclonic rotation in time Gill (1982).

While there has been significant observational evidence and analysis of the impact of surface currents on surface waves, limited previous research has focused on inertial currents, despite their common occurrence and importance to surface kinetic energy. This is due in part to the inability of satellite-based current products to resolve the time variability of the inertial-band, making studies using the tools of (Ardhuin et al., 2017; Marechal and Ardhuin, 2021; Quilfen and Chapron, 2019) ill-suited to applying to inertial currents. Instead, simultaneous measurements of waves and currents with fine enough temporal resolution to resolve inertial frequencies are required.

This chapter focuses on extending the idealized modeling in chapter 3 by identifying the impacts of inertial currents on surface waves from observational records of wave buoys. Gemmrich and Garrett (2012) identified that the impacts of both inertial and tidal currents could be identified in the timeseries of Hs records in the northeast Pacific. Additionally, these authors found that for a wave-buoy located in the Dixon Entrance in British Colombia, wave heights tended to be increased when tidal-currents were following the wave direction, and decreased when currents were following the waves. This contradicts traditional expectations of the relationship between surface currents and wave height modifications (Phillips, 1966), but no direct explanation for this observation was provided in Gemmrich and Garrett (2012). However, more recent work has found that in locations where tidal currents can be modeled as a traveling shallow water wave, this result emerges when the relationship between the group speed of the tidal wave is similar to that of the surface waves (Ho et al., 2023).

A lack of observations of surface currents co-located with the wave buoys in Gemmrich and Garrett (2012) study prevented a complete analysis of the impact of inertial currents on wave properties. To date, to my knowledge no other observations of the impact of inertial currents on surface waves have been published. This work seek to address this paucity of observations by considering two case studies where wave and current measurements are made simultaneously in regions with significant inertial kinetic energy. This research is focused on analyzing historical waves, current, and wind data from Ocean Station Papa in the Gulf of Alaska and Astoria Canyon off the coast of Oregon in order to answer the following questions:

1. Do surface wave properties exhibit increase variability in the near-inertial band, and can this be attributed to surface currents?
2. What is the relationship between the wave-relative inertial current direction and Hs and mss modifications?

4.3 Methods

This study utilizes measurements from two Waverider wave buoys operated by the Coastal Data Information Program (CDIP) with co-located current measurements. Specifically, data is used from station 166 located at Ocean Station Papa in the Northeast Pacific (Thomson et al., 2013), and station 179 located in Astoria Canyon off the coast of Oregon (Coastal Data Information Program, 2013). These buoys were selected due to being located in regions with a well documented history of inertial currents being an important component of velocity variance, with the expectation that therefore the effect of these currents on surface waves may be most visible (Alford et al., 2012; Kim and Kosro, 2013).

Current measurements are available at each of these two locations, allowing for the analysis of inertial currents and wave properties. Station 179 at Astoria Canyon is co-located with coastal High-frequency radar measurements operated by NOAA's Integratred Ocean Observing System (IOOS) (Program and Center, 2015). In addition to the Waverider at Station Papa, a nearby surface mooring operated by NOAA provides upper ocean velocity measurements with a down-looking Acoustic Doppler Current Profiler (ADCP) (NOAA PMEL et al., 2023). Current measurements from 10m depth bin from the ADCP measurements at Station Papa are used as the surface current. Details of each deployment location are provided in table 4.1, including the dates of the data used in this study.

Table 4.1: Overview of CDIP wave buoys and associated current measurements used in this study.

Location	Latitude	Longitude	Inertial Period	Dates used	Current Measurements
Station Papa	49.9 N	145.2 W	15.67 hrs	2012-2017	Downward-looking 300kHz Sentinel ADCP used for 2011-2017, upward-looking 400kHz Aquadopp profiler from 2017-Present
Astoria Canyon	46.1 N	124.6 W	16.6 hrs	2020-2024	Coastal HF-Radar velocities provided by IOOS

Waverider buoys report surface wave energy density spectra, $E(f)$ in 64 frequency bins every 30 minutes. Additionally, these buoys report a suite of other measurements, including the mean wave direction of the waves in each frequency bin and significant wave height (Hs). Two parameters that will be used throughout this work to characterize the current impacts on waves are the significant wave height (Hs) and the mean-squared slope (mss) of the waves. These parameters are defined as in equations 1.4 and 1.5 above:

$$Hs = 4\sqrt{\int E(f)df}$$

and

$$mss = \int \frac{(2\pi f)^4 E(f)}{g^2} df$$

which are standard definitions of these two parameters (Munk, 1944; Davis et al., 2023).

4.3.1 Doppler Correction

Since the Waverider wave buoys measure surface wave properties in a Eulerian reference frame, a Doppler shift correction of the wave frequencies due to the ocean currents is applied Herman et al. (2026). The observed frequency of ocean surface waves by a stationary platform, or the absolute frequency ω, is defined as:

$$\omega = \sigma + \mathbf{k} \cdot \mathbf{U} \tag{4.1}$$

Where $\mathbf{k}$ is the wavenumber of the surface waves, σ is the intrinsic frequency of the waves, and U is the surface current vector. For waves in deep water, the dispersion relationship gives that $\sigma^2 = gk$, where g is the acceleration due to gravity. Substituting this into equation 4.1 produces a quadratic equation for σ that can be solved using the measured surface currents at the NOAA surface mooring and wave directions measured by the Waverider buoy. The Waverider buoy reports a mean wave direction for each of the 64 measured frequency bins, $MWD(f)$, in the meteorological directional convention of degrees from north. In order to take the dot-product of $\mathbf{k}$ and $\mathbf{U}$, these two vectors need to be represented in the same coordinate system. Currents are defined as $\mathbf{U} = u\hat{\imath} + v\hat{\jmath}$, where the $\hat{\imath}, \hat{\jmath}$ unit vectors are to the east and north respectively. Mean wave direction is then calculated in terms of same coordinates as the currents:

$$\theta_w(f) = -1 * (MWD(f) + 90^\circ)\%360^\circ$$

where here % is the modulo operator. Then, $\mathbf{k} = \sigma\left[cos(\theta_w)\hat{\imath} + \sin(\theta_w)\hat{\jmath}\right]$. The dispersion relationship in equation 4.1 then becomes:

$$\left[\frac{u\cos(\theta_w) + v\sin(\theta_w)}{g}\right]\sigma^2 + \sigma - \omega = 0 \tag{4.2}$$

This quadratic equation is then solved to find the intrinsic frequency σ corresponding to each observed frequency ω. The relationship between all the measured ω's and calculated σ's at Ocean Station Papa are shown in figure 4.1 where each point represents a measurement of a frequency, direction, and surface currents, with 64 points for each 30 minute sampling window in the record. The coloring of points represents the mangitude of the projection of the surface current vector onto the wavenumber vector, with strong following currents in purple, and strong opposing currents in orange. Following currents cause the frequency of waves observed at the stationary platform to increase relative to their intrinsic frequency, while opposing currents cause the observed frequency to decrease for the same intrinsic frequency. Once the measured wave frequencies have been transformed to their intrinsic frequencies, wave parameters are calculated from the doppler shifted wave energy density spectrum $E(\sigma)$. Doppler shifting has no impact on Hs measurements, as it does not impact the overall magnitude of $E(\sigma)$, just shifts how wave energy is distributed in frequency space (figure 4.1(c)). However, since the mean squared slope is a function of $f^4E(f)$, shifting the distribution of $E(f)$ over frequency space can result in significant impacts on the mss measurements depending on the reference frame the measurements are made in. This can be seen in the large dependence of $mss_{observed}$ on current speed in figure 4.1 (b), while $Hs_{observed}$ and $Hs_{intrinsic}$ are almost identical in panel (c).

One caveat is the difference in the location of the current measurements relative to the wave measurements at Ocean Station Papa and Astoria Canyon. At Ocean Station Papa, the NOAA surface mooring (measuring winds and surface currents) is located approximately 25km away from the Waverider buoy. This potentially introduces error into the Doppler shift correction, as the currents are likely not uniform across those 25km. At Astoria Canyon, HF-Radar current measurements are reported on a 6km grid around the Waverider buoy, so this is less of a potential source of error.

4.3.2 Inertial Frequency Analysis

In order to isolate inertial current signals in the observed data, a bandpass filter is applied around the inertial frequency, from $\{0.9-1.1\}f$. For Station Papa this corresponds to a pass-band of $\{14.0-17.2\}$hrs, and for Astoria a pass-band of $\{15.0-18.3\}$hrs, so there should be negligible impact from tidal frequencies. Throughout this work the subscript i (e.g. Hs_i, mss_i) is used to indicate inertially band-passed quantities. Power spectra of timeseries are calculated by splitting the timeseries into 512 point windows overlapped by 50%, a Hann window is applied to each segment, and then the resulting power spectrum are averaged.

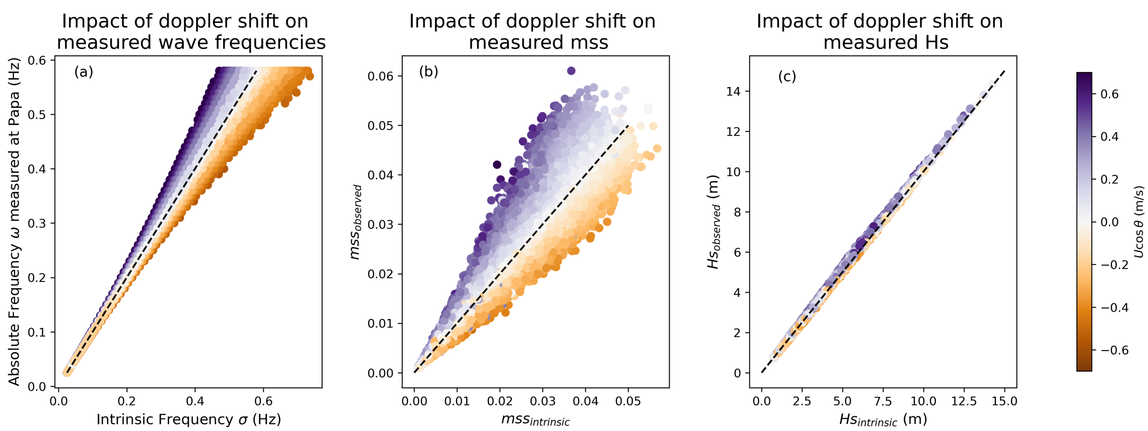

Figure 4.1: Demonstration of impact of surface currents on observed frequencies and wave measurements in Ocean Station Papa data. Impact on (a) measured wave frequencies, (b) measured mss, and (c) Hs. Dashed black line indicates a 1:1 relationship between the intrinsic and observed quantities, corresponding to stationary water. Points are colored by $U\cos(\theta)$, the magnitude of the currents projected onto the wave direction. When $U\cos(\theta)$ is positive, the waves and the currents are in the same direction, and when $U\cos(\theta)$ is negative the currents are opposing the waves.

95% confidence intervals of spectral levels are calculated based on chi-square distribution where the equivalent degrees of freedom for each spectrum is determined following the procedure first outlined in (Welch, 1967).

For comparisons of the inertial current and wave directions, two different methods of bandpassing can be performed. First, the currents can be projected onto the wave direction, and then a bandpass filter applied, which will be denoted as $[U\cos(\Theta)]_i$. Second, a bandpass filter can first be applied to the measured currents before projecting onto the wave direction, which will be denoted as $U_i\cos(\Theta)$. Here, Θ is the angle between the waves and the currents such that $\mathbf{U}\cdot\hat{k} = \|\mathbf{U}\|\cos(\Theta) = u\cos(\theta) + v\sin(\theta)$, where θ is the direction of the waves in a right-handed coordinate system with $\theta = 0$ corresponding to a travel towards the east. For comparing the effect of inertial currents on Hs and mss, various choices for the definition of wave direction are possible. Three definitions that will be considered here are (1) the direction of the peak wave frequency (θ_{peak}), (2) the energy weighted mean wave direction of the whole spectrum (θ_{mwd}), and (3) the energy-weighed mean wave direction over the equilibrium range, (θ_{eq}), where the equilibrium range defined to be $0.2 - 0.4Hz$, following Thomson et al. (2013). For considerations of the impact of inertial currents on Hs, the most relevant wave directions are the peak direction Θ_{peak} and the energy-weighted mean wave direction $\Theta_{weighted}$, as these are more representative of the direction of waves contributing most of the significant wave height. The results here will be presented for $\Theta_{weighted}$, although results are similar for Θ_{peak}, as energy weighted mean wave direction and peak wave period are highly correlated at both locations ($R > 0.7$ at both sites). For considerations of the impact of currents on mss the direction of waves in the equilibrium range is primarily considered, Θ_{eq}, as these waves play a larger role in determining the mss.

4.4 Results

4.4.1 Background Conditions

At Ocean Station Papa, Hs and T_a demonstrate a clear seasonal patter, with Hs peaking during the winter months when winter storms are common, and the waves more swell dominated with longer periods (figure 4.2). The 4-years of data from the Astoria buoy show

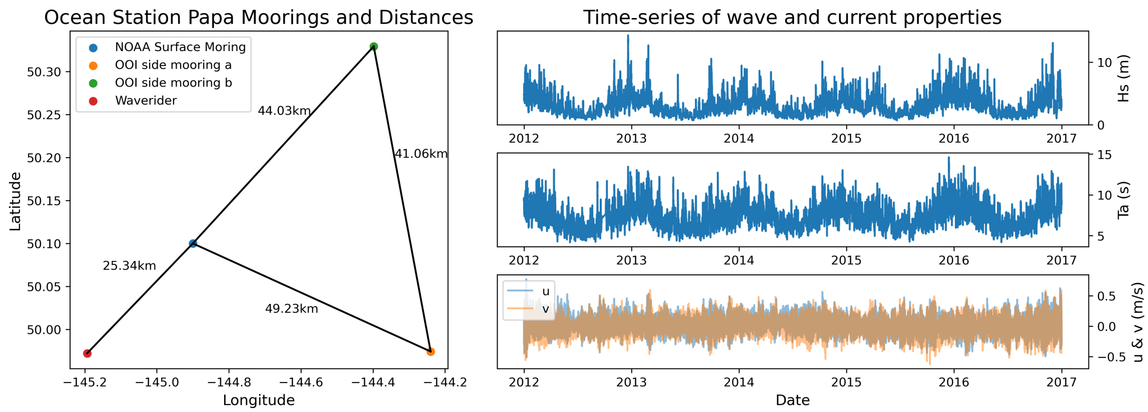

Figure 4.2: Location of moorings at Ocean Station Papa. Wave measurements are from the Waverider buoy, and near-surface (10m depth) current measurements are from the NOAA surface mooring's ADCP profiler. Timeseries show values of Hs, T_a, and u and v currents.

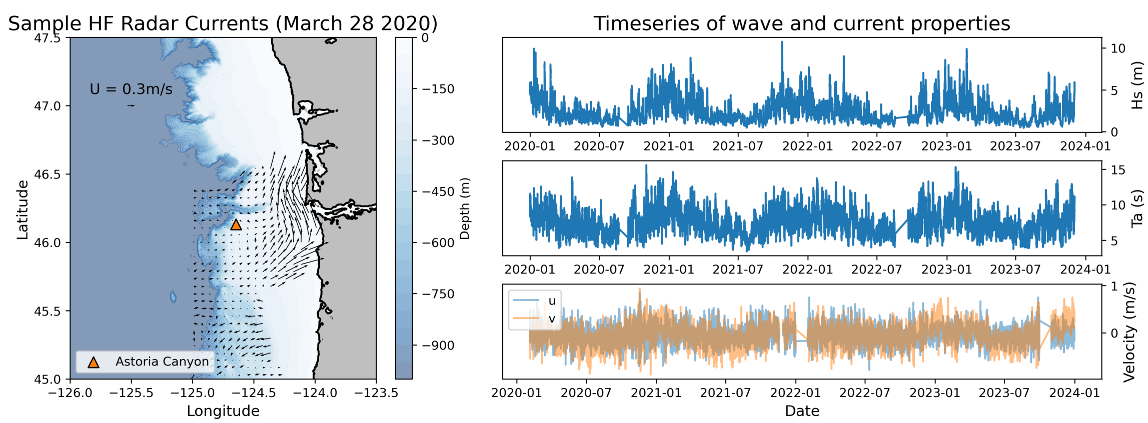

Figure 4.3: Location of Astoria Canyon Buoy off the Oregon Coast. Overlaid vectors are a sample snapshot of surface velocities measured by high-frequency radars located on the coast. Timeseries show values of Hs, T_a, and u and v currents over the 4 year period considered.

a somewhat similar pattern, with the largest wave heights and wave periods tending to occur during the winter months (figure 4.3). There is no obvious seasonal pattern of mean currents at Ocean Station Papa, with currents varying primarily at higher frequencies between -0.5 and 0.5m/s. At Astoria Canyon, currents show variability on a range of timescales, with a seasonal pattern of northward currents during the late fall and winter and southward currents during the late spring and summer. This is an expected pattern, with a long history of observations of southerly, upwelling-favorable winds driving southward currents during the summer months, and northerly downwelling-favorable winds driving northward currents in the winter months along the Washington and Oregon coasts(Huyer, 1977).

4.4.2 Frequency Analysis

At Ocean Station Papa, most of the surface current variability is contained within the inertial frequency and semi-diurnal tidal bands. The peak variance in the spectra of u and v variability at Papa occurs at the inertial frequency of 15.67 hours, with the second largest peak occurring at the semidiurnal tidal frequency (figure 4.4(b)). These two peaks emerge in the spectra of both the Hs and mss timeseries, and the lack of additional variability at these frequencies in the wind spectrum in figure 4.4(a) suggests that the current variability is likely the source of the wave variability at these frequencies. Similar patterns are present in the Astoria Canyon data, with u and v showing a clear peak a the inertial and semi-diurnal tidal frequencies, although these frequencies do not carry as much of the overall variance in the current timeseries as at Ocean Station Papa (figure 4.5(b)). Additionally, Hs and mss again show clear peaks at the inertial and tidal periods, with no evidence of an inertial peak in wind speeds that could drive the wave variability near the inertial frequency. These results suggest that at both locations, inertial currents are driving wave-variability, as there is no other mechanism which could be generating the observed increased variability in wave properties in the inertial band. The same can be said for tidal currents at the Ocean Station Papa location, although at the Astoria Canyon site there are peaks in the frequency spectrum of 10m East-West winds (U_{10}) at both the semi-diurnal and diurnal tidal frequencies, but less of a peak in V_{10} (figure 4.5 (a)). This is likely an effect of a diurnal

Table 4.2: Overview of modification of Hs and mss in near-inertial band $(0.9 - 1.1)f$ at each location. The % of variance in the near inertial band is calculated by calculating the variance of the near-inertial band and dividing by the total variance of the time-series.

Location	Parameter [$*$]	% of Variance in NI-band	$(100 \times [*]_i/[*]_{total})_{0.50}$	$(100 \times [*]_i/[*]_{total})_{0.95}$
Station Papa	Hs	0.4%	2%	6%
	mss	1.6 %	4%	16%
Astoria Canyon	Hs	0.6%	2%	8%
	mss	2.0 %	5%	24%

sea breeze on and off the Oregon coast Frye et al. (1972). Due to these diurnal/semi-diurnal winds it would likely be more difficult to disentangle the effects of tidal currents on Hs and mss from the effects of wind forcing at this location.

While these peaks are present in the spectra of wave properties, they are small relative to the overall variance of the timeseries. At Ocean Station Papa, the near-inertial band $(0.9-1.1f)$ carries only 0.4% of the overall variance in Hs and 1.6% of the variance in mss, while at Astoria Canyon the near-inertial band carries 0.6% of the Hs variance and 2.1% of the mss variance. The typical contribution of overall Hs and mss from the inertial band is calculated by band-passing the timeseries of each quantity with a pass-band of $0.9 - 1.1f$. Across these timeseries, at Ocean Station Papa, the magnitude of the inertially bandpassed Hs is typically $\sim$ 2% of the total Hs, and the bandpassed mss is typically $\sim$ 4% of the total mss. At Astoria, these quantities are quite similar, with inertially bandpassed Hs is typically $\sim$ 2% of the total Hs, and bandpassed mss is typically $\sim$ 3% of the total (see table 4.2). The 95th percentiles of the Hs_i and mss_i distributions are shown on the right hand side of this table, and these values are 3-4 times the 50th percentile values.

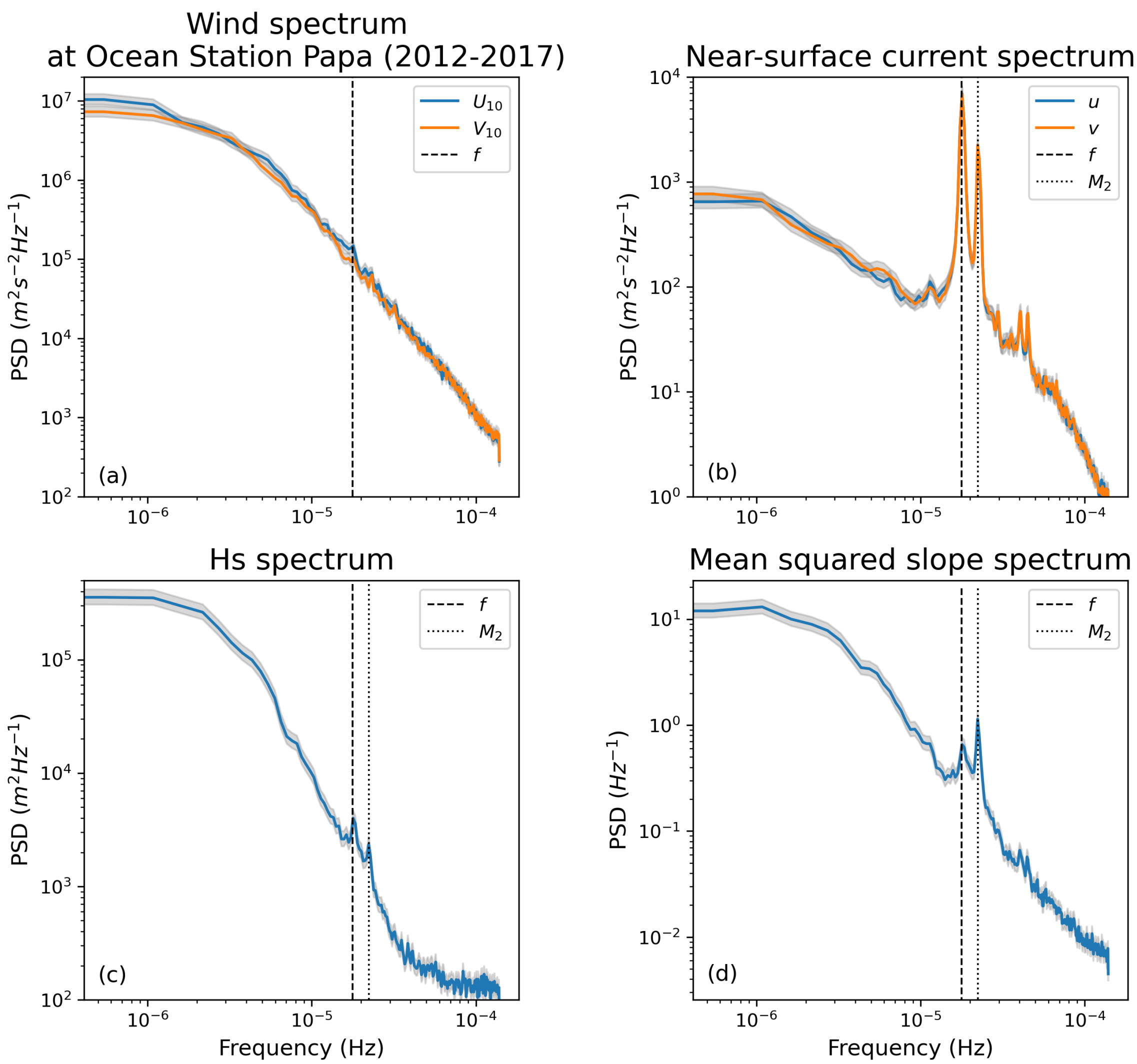

Figure 4.4: Power spectrum of timeseries of (a) winds, (b) surface currents, (c) Hs and (d) mss measured at Ocean Station Papa from 2012-2017. Dashed vertical lines indicate the local inertial frequency (15.6hrs), and the dotted vertical line indicates the semidiurnal M_2 tidal frequency (12.4hrs). Filled regions represent 95% confidence intervals of the spectrum.

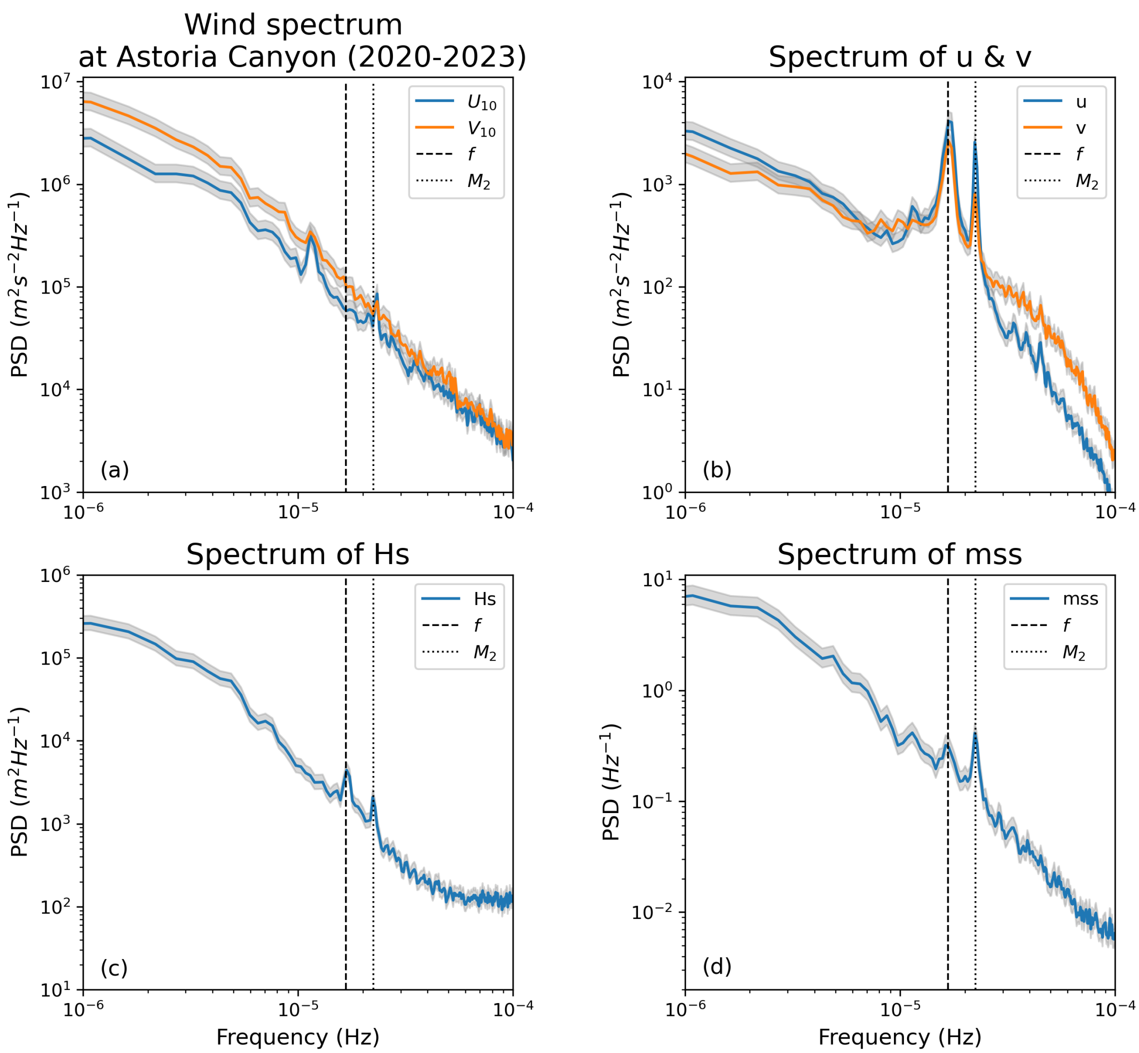

Figure 4.5: Power spectrum of timeseries of (a) winds, (b) surface currents, (c) Hs and (d) mss measured at Astoria Canyon from 2020-2023. Dashed vertical lines indicate the local inertial frequency (16.6hrs), and the dotted vertical line indicates the semidiurnal M_2 tidal frequency (12.4hrs). Filled regions represent 95% confidence intervals of the spectrum.

4.4.3 Inertial Current Phasing

While these results suggest that inertial currents are a source of wave modification, they do not indicate at all how the direction of inertial currents impacts surface waves; that is, what direction of waves and inertial currents correspond to elevated wave heights. By bandpassing Hs' and $[U\cos(\Theta)]$ around the inertial frequency, the relationship between inertial current - wave direction and Hs' can be investigated. At both locations, currents following surface waves, or $[U\cos(\Theta)]_i > 0$, is correlated with increased in Hs'_i, while opposing currents ($[U\cos(\Theta)]_i > 0$) are correlated with decreased Hs'_i (figure 4.6(a,c)). In figure 4.6 the distribution of measurements in $U\cos(\Theta)_i$ and Hs_i/Hs space is presented. At both locations, looking at the overall distribution is not particularly enlightening, so data is binned into $0.05m/s$ bins and calculate the mean Hs_i/Hs and mss_i/mss anomalies for each bin. The means are plotted as the black dots over the distribution. Each point has error bars of ±2 times the standard error of the mean in each bin. Additionally, ±1 standard deviation from the mean is plotted as a gray dashed line. To the right hand side of each 2d histogram we plot the distribution of the bandpassed quantity for strong following or opposing inertial currents. Here we define "strong" opposing or following currents as the 5th and 95th percentiles of the $U\cos(\Theta)_i$ timeseries for each location. For Ocean Station Papa, the 5th/95th percentile is $\pm0.13m/s$, and for Astoria Canyon this is $\pm0.1m/s$.

This analysis at both locations indicates the same slightly surprising result. First, we find that the Hs anomaly driven by the inertial currents is positively correlated with the magnitude of inertial currents in the wave direction. This suggests that when inertial currents are following surface waves this tends to correlate with an increase in Hs, and when the currents are opposing the surface waves this tends to correspond to a decrease in Hs. This can be observed by the positive slope of the binned means, as well as the differences in the distribution of Hs_i/Hs between strongly following and opposing currents in the histograms in panel (b). This trend in Hs_i/Hs is weaker at Astoria Canyon than Ocean Station Papa.

In contrast, the data suggests a negative relationship between mss_i/mss and $U\cos(\Theta)_i$. This implies when inertial currents oppose waves that wave slopes are elevated, and when

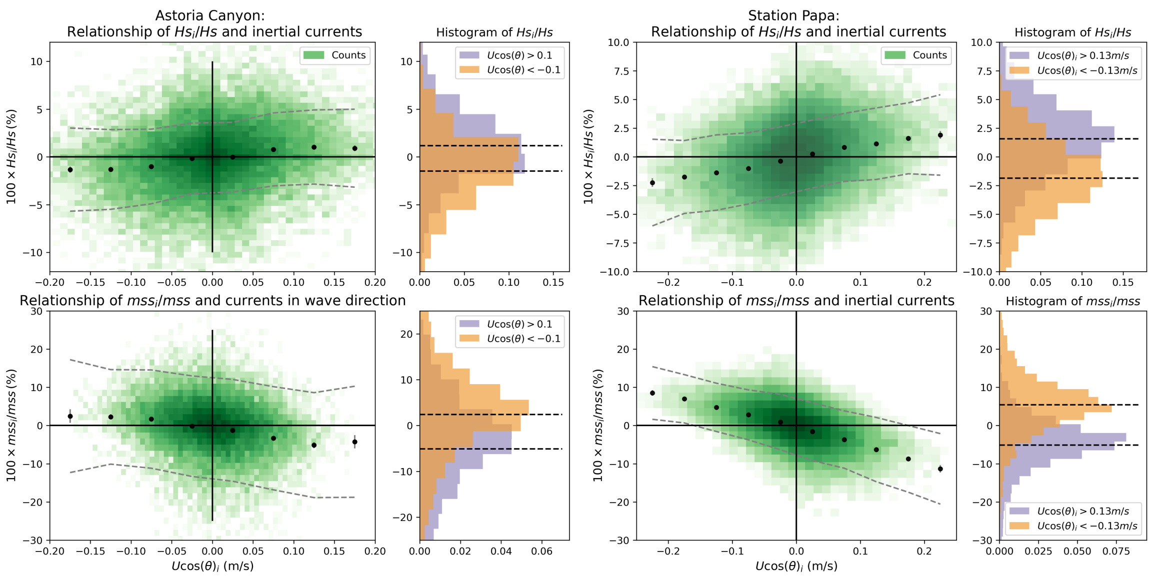

Figure 4.6: (a) Histogram of Hs_i/Hs and $U\cos(\Theta)_i$ measurements at Astoria. Black marks indicate bin averaged values, with gray error bars indicating ± 2 standard error, ad dashed lines 1 standard deviation, of the bin mean. (c) Histogram of $100 * Hs_i/Hs$ for currents faster the 95th percentile of all measured currents (purple) and slower than the 5th percentile (orange). Black dashed lines indicate the mean of these distributions. (b) and (d) are the same as (a) and (b) but for mss. Panels (e)-(h) are the same, except for the Ocean Station Papa data.

currents follow waves they are flattened. The magnitude of the change is larger for mss than Hs, by approximately a factor of 2. This implies is that on average, while following currents increase the overall energy of the waves $\int E(\sigma)d\sigma$, the energy at higher frequencies, more heavily weighted by the σ^4 dependence of mss, increases.

4.5 Discussion

The observations from wave and current measurements at Ocean Station Papa and Astoria Canyon both demonstrate that inertial-currents contribute a small, but measurable, modification of surface wave properties Hs and mss. The magnitudes of of Hs_i/Hs variability observed at Ocean Station Papa and Astoria Canyon largely agree with the observations from Gemmrich and Garrett (2012) in the Northeast Pacific, where the authors found Hs modulation in the inertial band of $\sim 2-3\%$ over a period of approximately 20 years. Note that in this work here, as in Gemmrich and Garrett (2012), the background level of variability that might be expected without inertial currents has not been removed from the estimates of the wave variability in the inertial-band. It is not expected that this would make a large difference in the results presented here, but this should be verified in future work.

A classic textbook example of wave current interactions considers the case where waves are assumed to have propagated from a region of no-currents into the region with currents either following or opposing the waves (Phillips, 1966). Under these assumptions, currents opposing waves will cause the wave height to increase and the waves to steepen, and waves following the current will cause the wave heights to decrease and waves more shallowly sloped. While this framework can be a useful tool for developing intuition for how currents may impact waves, the results presented here suggest that for inertial currents the relationship between wave heights, slopes and inertial currents are more complicated. To start, the tendency towards an increase in Hs with following inertial currents is opposite of what would be expected. This result is in-line with the observations of wave - tidal current interactions from both Gemmrich and Garrett (2012) and Ho et al. (2023), however it is not immediately clear that the same dynamical reason posited by Ho et al. (2023) would apply here. Namely, the rotation of the inertial currents differs from the tidal currents considered there, and additionally, the increase in Hs with following currents in those observations relied on the group speed of the propagating tidal wave c_t to exceed that of $(c_g + U)$, which is significantly faster than typical group speeds of near-inertial waves in the North Pacific (Gemmrich and Garrett, 2012; Chelton et al., 1998; Yuan et al., 2024).

Comparison with idealized model results from Chapter 3 potentially may be able shed some light on the Hs observations here. Typical peak wave periods at Astoria Canyon and Ocean Station Papa are $10 - 11s$, and typical decorrelation length scales of inertial motions in these regions have been estimated to be $\sim$ 60km near Astoria Canyon and $\sim$ 100km near Station Papa (Etienne et al., 2025; Kim and Kosro, 2013). In the framework of the idealized modeling in chapter 3, this would correspond to a value of $c_g T/L \approx 4$. A version of figure 4.6 for an idealized model run from Chapter 3 with these parameters is shown in figure 4.7. Qualitatively, the distribution of Hs_i/Hs from the idealized model looks quite similar to the observations from both Ocean Station Papa and Astoria Canyon. The histogram of Hs_i'/Hs from the idealized model shows significantly more structure than the observed histograms from Astoria and Station Papa, with a few different "arms" of higher occurrence relationships between Hs' and $[U\cos(\theta)]_i$. These features in the histogram correspond to specific regions of the model domain across the inertial-cycle, and are highly specific to geometry of the model run. Given that the observations from both Station Papa and Astoria Canyon likely span a wide range of wave and current parameters, while the idealized model only represents a single set of parameter values, so it is expected that the observations would exhibit a wider, and more smoothed out, spread of Hs_i responses to $U\cos(\Theta)_i$ than the model output in figure 4.7.

One reason the results for mss may differ than for Hs is the relatively larger importance of relative wind to mss compared to Hs. Under the assumption of wave breaking balancing dissipation over the equilibrium range of the surface wave spectra, $u_{star} = C_D^{1/2}(U_{10} - U\cos\Theta)$, and $mss \propto u_*$, where here $(U_{10} - U\cos\Theta)$ is the wind relative to the ocean surface current (Thomson et al., 2013; Iyer et al., 2022). Following a drag coefficient parameterization from Large and Pond (1981), we can estimate the effect of relative wind on the mss_i, following what as was done in (Iyer et al., 2022). The impacts of this relative wind effect compared with the overall mss_i/mss trend are shown in figure 4.8. Here we can

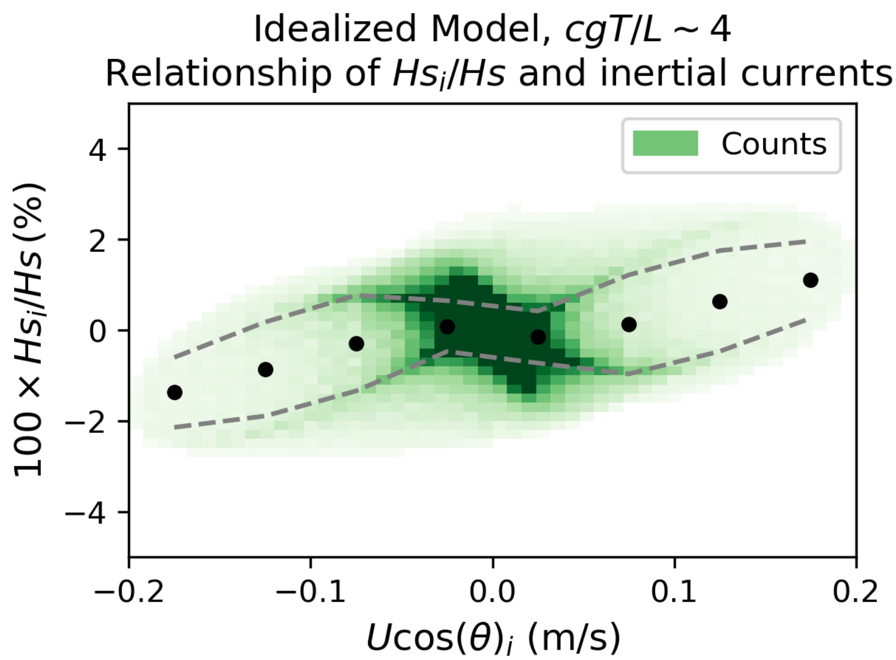

Figure 4.7: Same as figure 4.6, but for the idealized model from Chapter 3, with $cgT/L \sim 4$, a value that appears typical based on average properties at Ocean Station Papa and Astoria Canyon. Dashed lines indicate mean $100 * Hs_i/Hs$ for currents faster than the 95th percentile of modeled currents (purple) and slower than the 5th percentile (orange).

see that the estimated impact of relative wind on mss is too small to account for the steepening and flattening of waves in opposing and following waves respectively. Additionally, it is worth noting that there is an asymmetry in the mss_i/mss response in following vs. opposing current conditions, one that is not expected from relative-wind effects alone. For example, at following currents of $0.1m/s$ the inertially bandpassed mss is approximately 5% of the total, while for opposing currents of the same magnitude mss_i is only $2-3\%$ of the overall value at both locations (figure 4.8. Thus, further work is needed to better understand the reason for this opposite response in mss compared to Hs. Additionally, since mss plays an important role in modulating surface wind stress (τ) at the ocean surface, understanding these frequent 5-10% fluctuations is potentially important to improving predictions of upper ocean processes.

While the framework used in this study allows for a characterization of the average or bulk relationship between $[U\cos(\theta)]_i$ and Hs' or mss', it obscures the specific dynamics of the wave-current interactions at any point in time. Thus, an important limitation of this study is the inability to explain why the observed relationships exist. Future studies making more detailed investigations of a discrete set of specific instances of inertial current modification of surface waves could lend explanation to what mechanisms are generating the trends observed in this work. Additional limitations of this study include the assumption that the equilibrium range of the surface waves is well represented by the frequency band $0.2-0.4$ Hz across 4 years of data at Astoria Canyon and 5 years of data at Ocean Station Papa. This appears to be a reasonable assumption on average, as investigation of surface wave spectra across all data at both locations suggests that spectra follow an f^{-4} slope, with spectral height largely a function of windspeed (not shown here). Finally, in this work we assume that surface currents at the Astoria and Ocean Station Papa buoy locations are well represented by the nearby current measurements. At any given point in time the actual currents at the wave buoy may differ slightly in both magnitude and direction from the location where the current measurements are made. However, it is reasonable to assume that these differences are both small and random and will be averaged out over many years of data.

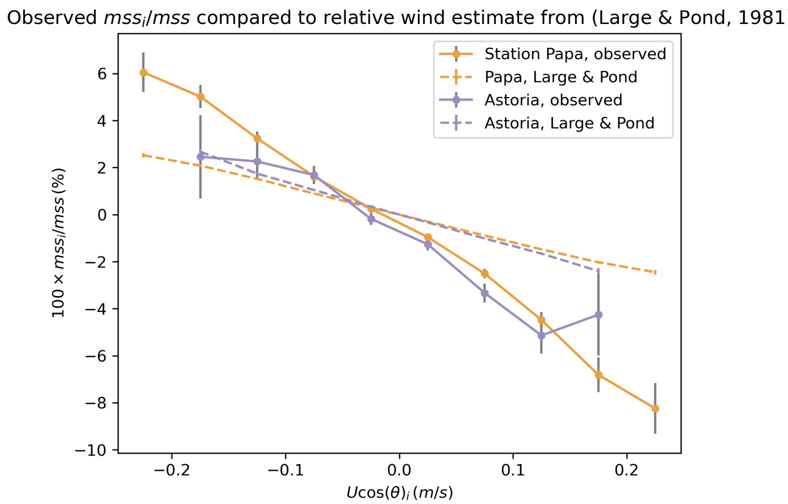

Figure 4.8: Impact of $U\cos(\Theta)_i$ on mss_i/mss as measured at Station Papa (Orange) and Astoria (Purple), the same curves shown in figure 4.6 (b) & (f). Dashed lines are the predicted response only due to then relative wind effect only at each location.

4.6 Conclusion

This work analyzes observations of waves and currents from NOAA's Ocean Station Papa moorings and Astoria Canyon, provided by CDIP and PACIOOS. At both locations wave properties (Hs and mss) exhibit increased variability in the near-inertial band. Neither location exhibits increased wind variability in this frequency band, indicating that these variations in wave properties are being driven by wave-current interactions. Phase relationships between bandpassed Hs' and inertial-currents indicate that currents following waves at both these locations are correlated with increases in Hs, while opposing currents correlate with decreases in Hs. This observation is largely consistent with modeling results from Chapter 3, and presents first observation of this kind suggesting that the relationship between instantaneous current relative wave direction. These effects are small on average, with mean variability in the inertial band reaching $\sim 2\%$ of the background value of Hs and $\sim 4\%$ of mss, although extreme values can reach up to 10% and 20% of background values for Hs and mss respectively.

Chapter 5

CONCLUSION

The work in this study contributes both new tools and results to the study of surface wave and current interactions, validating a new wave-measurement methodology for a current-measuring profiling float in Chapter 2, and presenting new results on the theoretical and observational impact of near-inertial currents on surface waves in chapters 3 and 4. The results from chapter 2 suggest that EM-APEX profiling floats could be applied as useful tools in future field campaigns targeted at understanding wave-current interactions. Chapters 3 and 4 suggests that inertial currents can play an important role in the modulation of surface waves, and that the time variability of these currents causes the physics of these modulations to differ from the steady and tidal cases that have been more extensively studied. Furthermore, through both modeling and observations, this work indicates that inertial motions with spatial scales on the order of $O(100km)$ in the mid-latitudes can have a generally small, but potentially important, impact on surface wave heights and slopes.

The observational evidence for impacts of inertial currents on surface waves in this work was limited to two Waverider buoys in the North Pacific that had co-located wave, wind and current measurements. Therefore, while this analysis indicates that inertial currents may play an important role in modifying waves at these locations, a valuable extension of this analysis would be to identify additional locations with measurements of both waves and currents in lower latitude regions with longer inertial periods, and therefore larger typical values of $c_g T/L$. This would be useful in determining if the effects of currents on waves are dependent on the inertial period in ways suggested by the results of Chapter 3.

Previous work has demonstrated that surface waves can play an important role in modifying wind power input into inertial motions in the ocean (Liu et al., 2017). This dissertation suggests that interactions between near-inertial currents and waves, and their modification of Hs and mss could play an important feedback role in this process, modifying the wind power input to mixed layer inertial motions. Future extensions of this work should target this feedback mechanism, and determine to what extent the modification of waves by inertial currents impacts wind input to inertial motions. A few downstream implications of inertial-current wave-modulation that should be explored in future work include investigating the impact on wave forecast accuracy in regions with significant inertial currents, and determining if and how modifications of both wave height and breaking may modulate near-surface wave-driven mixing.

Additionally, this work adds to a growing body of literature, such as the work of Ho et al. (2023); Papandreou et al. (2026), indicating that considering the time rate of change of ocean currents can result in wave modifications that are perhaps unexpected when viewed from a framework of the results of wave-current interaction studies that have considered only steady or more slowly varying currents. The last decade or so has shown an continual increase in evidence that ocean currents can impart a rich spatial structure to the surface wave field than was previously unexpected, and this work contributes to the continuation of that trend, with the added contribution that time-variability of currents can add additional spatial and temporal variability to the wave-field. While future work, especially that making use of the new high spatial resolution surface wave measurements from the SWOT satellite (Bôas et al., 2025), will continue to investigate the impacts of current spatial variability on surface waves, it will be important to remember that time variability of currents also are important for making accurate predictions of surface waves.

Appendix A
DATA AVAILABILITY

Data used in Chapter 2 is available at at https://doi.org/10.5061/dryad.4qrfj6qhr. Software for calculating EM-APEX float surface wave measurements is also available `https://github.com/jjstadler/EMAPEX_WAVES`.

All the code and steps for running the simulations and generating the figures and results presented in this Chapter 3 are freely available at `https://github.com/jjstadler/inertial-current-wavewatch-simulations`

Appendix B

EM-APEX WAVE MEASUREMENT MODEL

In order to characterize the lower limit of significant wave-heights that are able to be measured by the EM-APEX float, a model of the EM-APEX float sampling procedure was created to simulate the wave-height the float would measure for a given surface-wave field and 1Hz velocity noise level. The model configuration is schematized in figure B.1.

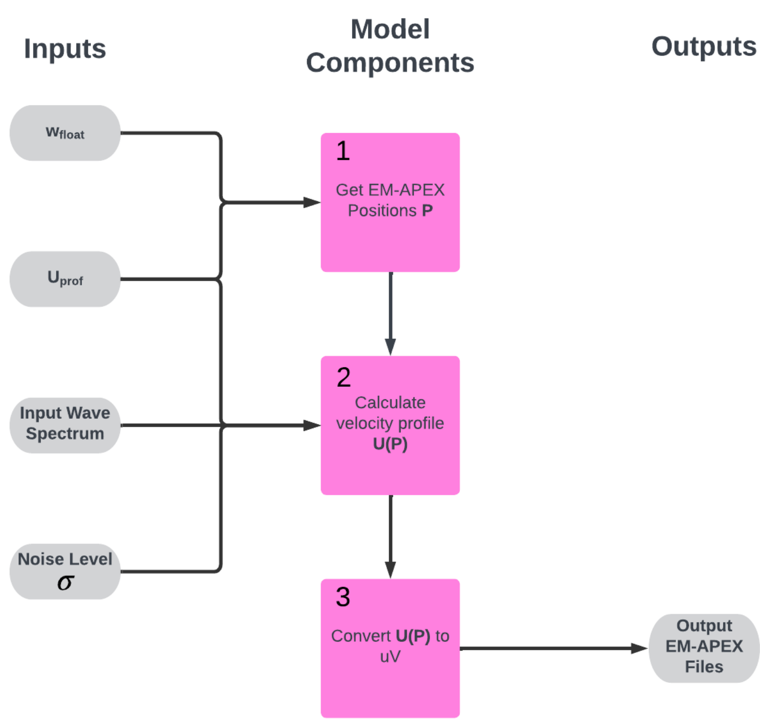

Figure B.1: Schematic of model used to simulate EM-APEX measurements

The position and angular orientation of the float in space at each point in time $(P(x,t)$ is determined in model component 1 based on the vertical profiling speed of the float, it's rotation rate, and the horizontal advection of the float by the mean current profile. The second component calculates the velocities at the positions $P(x, \theta, t)$ based off any prescribed velocity profile ($\mathbf{U}_{prof}$) and any prescribed surface wave energy density spectrum $S(f)$. Based on any prescribed surface wave spectrum, the $u(P)$ velocities are given by:

$$\mathbf{u}(\mathbf{P}) = \mathbf{U}_{prof} + \int_f [2\pi a f \cos(k_x x_p + k_y y_p - 2\pi f t_p + \phi) e^{k z_p}] * (\cos(\theta_w)\hat{\imath} + \sin(\theta_w)\hat{\jmath}) df \quad \text{(B.1)}$$

where $x_p, y_p, z_p, t_p \in \mathbf{P}$, the integral is taken over the frequency range of the wave spectrum $S(f)$, a is the amplitude of wave at each frequency, θ_w is the angle of wave propagation at each frequency, and ϕ is a phase-shift that can be arbitrarily modified.

The velocity "measured" by the float at each depth would then be:

$$u_{measured}(P) = u(P) + u_{noise}(P) \quad \text{(B.2)}$$

Where each element $(u_{noise}, v_{noise}) \in u_{noise}(P)$ is drawn from the normal distribution $\mathcal{N}(0, \sigma)$, where $sigma$ is the standard deviation of the 1Hz velocity errors. Since the input spectrum contains no information about the relative phase of the waves, the phase of the waves at each frequency is randomized, and then a number of iterations of the simulation are performed with different random phases. For the analysis in this paper, 50 different phase-randomized realizations of each input spectra are run. Additionally, a tune-able white noise is added to each 1Hz residual-velocity measurement to allow for the modeling of the fitting uncertainty discussed above. This procedure is similar to that used by D'Asaro (2015) to simulate mixed-layer float wave measurements.

These velocities are then converted into EM-APEX voltage values using the relationships defined in equations 2 and 3. Sets of EM-APEX data files are then generated and saved, which can then be processed using the EM-APEX wave processing workflow and algorithm.

Simulations were run for over range of 1Hz noise levels and input surface wave-spectrum significant wave heights. 10 noise levels were used, ranging from $0.001 - 0.035 m/s$, and 17 significant wave heights ranging from $0.03 - 3m$. For each noise - H_s combination, 50 simulations were run with the phases of each surface-wave frequency randomized. Following the same procedure as with the real EM-APEX data, spectra and significant wave heights can then be calculated from this simulated data, as well as bootstrapped 95% confidence intervals. For each noise level, the minimum detectable H_s was defined as the lowest H_s for which the input surface wave spectra H_s was contained within the 95% C.I. of the simulated H_s. The results of these simulations were used to make Figure 2.9.

Appendix C

IMPACTS OF EM-APEX INERTIA ON WAVE MEASUREMENTS

Due to the EM-APEX float's inertia, at surface wave frequencies the float may not exactly follow the motion of the water, and the water may have some relative motion around the float. To investigate the impact of the float's inertia we constructed a simple quadratic drag model of the float's horizontal motion in a surface-wave velocity field. The velocity of the float is modeled as

$$\frac{du_f}{dt} = \frac{C_d * A * \rho}{M_f} * (u_w - u_f) * |u_w - u_f| \tag{C.1}$$

where here C_d is the drag coefficient, A is the cross-sectional area of the float, M_f is the mass of the float, ρ is the density of water, u_w is the water velocity and u_f is the float velocity. Here we assume realistic values of the constants for the EM-APEX float ($A = .209m^2$, $C_d = 1$, $\rho = 1000\,\mathrm{kg\,m^{-3}}$, and $M_f = 28\,\mathrm{kg}$). Prescribing a sinusoidal water velocity $u_w = 2\pi a f \sin(2\pi f t)$, where a is the surface wave amplitude, we then solve for u_f in equation C.1 as a function of time. We find that the impact of the float's inertia is to damp the amplitude of the float's horizontal motions compared to the water, and that the percent reduction in the float's velocity compared to that of the water is dependent on wave amplitude C.1. This suggests that if the float's electrodes measure the velocity of the float, then the inertial damping of the float's motion may reduce the estimate wave amplitude.

However, Sanford et al. (1978) demonstrated that depending on the geometry of the instrument and where the electrodes are located, non-water-following behavior can cause the electrode velocity measurement to respond to the water motion, the instrument motion, or something in between. Let us call the amplitude of the water's sinusoidal velocity a_w, the amplitude of the float's sinusoidal velocity a_f, and the amplitude of the electrode-measured sinusoidal velocity a_m. Sanford et al. (1978) considered the relationships among a_w, a_f,and a_m in three cases. In the case where the float is an infinitely long cylinder with electrodes located directly on the body of the float, the electric currents generated by the relative motion of the water past the float directly compensates for any difference between the float and water velocity—resulting in $a_m = a_w$. In a second case where the electrodes are located at a great distance from the float, *e.g.*, attached to it on long arms, then the electrodes directly measure the float velocity and $a_m = a_f$. In the third case where the float is a prolate spheroid and the electrodes are located near or on the float, the scenario which most closely matches the geometry of the EM-APEX float, Sanford et al. (1978) demonstrated that

$$\left(1 - \frac{a_m}{a_w}\right) = \left(1 - \frac{a_f}{a_w}\right)\left(\frac{1 + C_3}{1 + C_1}\right) \tag{C.2}$$

Where C_1 and C_3 are constants determined by the geometry of the float and the position of the electrodes. For the EM-APEX float, previous tests of the electrode measurement's response to an imposed electric current in a saltwater tank have indicated that $C_1 = 0.5$, and while we do not have measurements of C_3, we expect that $-0.5 < C_3 < -0.3$. If we define $\epsilon_m = \left(1 - \frac{a_m}{a_w}\right)$ as the fractional error in the measured velocity amplitude and $\epsilon_f = \left(1 - \frac{a_f}{a_w}\right)$ as the fractional error in the float's velocity amplitude, then we can write this more clearly as:

$$\epsilon_m = \epsilon_f \left(\frac{1 + C_3}{1 + C_1}\right) \tag{C.3}$$

We ran the quadratic drag model for a range of wave amplitudes and C_3 values and plotted ϵ_f and ϵ_m in figure C.1. This figure indicates that due to the float's inertia, there is a $5 - 13\%$ reduction in the amplitude of float's velocity compared to the surface wave amplitude, but that the C_3 factor reduces the discrepancy between the measured wave amplitude and the actual wave amplitude to between $2 - 6\%$. While this model is very simple, it suggests that the impacts of the floats inertia may result in about a $2 - 6\%$ error in the EM-APEX wave height measurements.

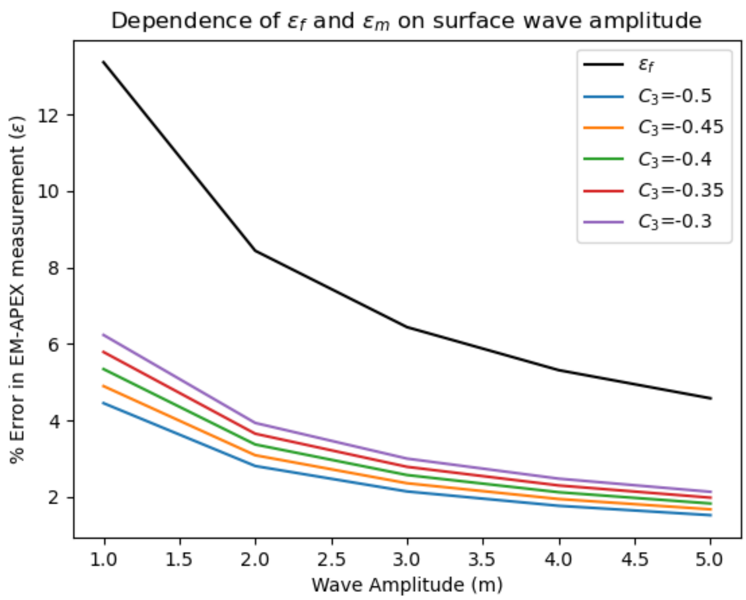

Figure C.1: The fractional difference between the float and water velocity amplitudes due to the inertia of the EM-APEX float is shown in black. The resulting impact in the % error of the actual measured wave amplitudes for a range of plausible C_3 values are shown in the colored lines.

Appendix D

WAVEWATCHIII CONFIGURATION

Our WavewatchIII models used in Chapter 3 were compiled with the following switches:

NOGRB DIST MPI PR3 UQ FLX0 LN1 ST4 STAB0 NL1 BT4 DB1 TR0 BS0 IC0 IS0 REF0 WNT2 WNX1 RWND CRT2 CRX1 O0 O1 O2 O3 O4 O5 O6 O7

Model time steps were set to: CFL: 600s, DTXY:300s, DTMIN: 5s. Models were run with shorter time-steps and no impact was found on the results presented here was found. Wave spectra were modeled with 30 frequency bins and 24 directional bins. Directional bins were evenly spaced in 15° increments, and frequency bins were defined such that the lowest frequency was $f_{min} = 0.04118\ Hz$, with an increment factor of 1.1, such that $f_n = 1.1 * f_{n-1}$. The model grid had an x and y spacing of 13.9 km. A few tests were run with higher spatial and spectral resolutions, but for the results were comparable to the analyses presented here. Thus, to save computation time the lower-resolution models were used for the full suite of model runs. Note that for much more narrow-banded directional spectra, such as for spreading coefficients $s \approx 50$, the directional spectral resolution used here was insufficient and resulted in some numerical instabilities, so to replicate these model runs with a more narrow-banded wave spectra the directional resolution used must be increased.

In order to turn off different components of the wave-action equation as described in Chapter 3, we modify the RUN namelist inside the *ww3_grid.nml* file for each run. For example, for a run with only advection, this section of the *ww3_grid.nml* would appear as the following:

&RUN_NML

RUN%FLCX = T

RUN%FLCY = T

RUN%FLCTH = F

RUN%FLCK = F

```
RUN%FLSOU = F
/
```

Where the FLCX & FLCY parameters control advection in the x & y direction, FLCTH controls the refraction term, and FLCK the wavenumber shift term, in the wave action equation. FLSOU=F turns off the source terms of the right hand side of equation 2.1, which we leave off for all model runs to simplify analysis, as in (Villas Boas et al., 2020).

BIBLIOGRAPHY

Alford, M. H., Cronin, M. F., and Klymak, J. M. (2012). Annual Cycle and Depth Penetration of Wind-Generated Near-Inertial Internal Waves at Ocean Station Papa in the Northeast Pacific. *Journal of Physical Oceanography*, 42(6):889–909.

Antcil, F., Donelan, M. A., Forristall, G., Steele, K., and Ouellet, Y. (1993). Deep-water field evaluation of of the ndbc-swade 3-m discus directional buoy. *Journal of Atmospheric and Oceanic Technology*, 10:97–112.

Arbic, B. K., Elipot, S., Brasch, J. M., Menemenlis, D., Ponte, A. L., Shriver, J. F., Yu, X., Zaron, E. D., Alford, M. H., Buijsman, M. C., Abernathey, R., Garcia, D., Guan, L., Martin, P. E., and Nelson, A. D. (2022). Near-Surface Oceanic Kinetic Energy Distributions From Drifter Observations and Numerical Models. *Journal of Geophysical Research: Oceans*, 127(10):e2022JC018551.

Ardhuin, F. (2024). *Ocean Waves in Geoscienes*.

Ardhuin, F., Chapron, B., and Elfouhaily, T. (2004). Waves and the Air–Sea Momentum Budget: Implications for Ocean Circulation Modeling. *Journal of Physical Oceanography*, 34(7):1741–1755.

Ardhuin, F., Gille, S. T., Menemenlis, D., Rocha, C. B., Rascle, N., Chapron, B., Gula, J., and Molemaker, J. (2017). Small-scale open ocean currents have large effects on wind wave heights. *Journal of Geophysical Research: Oceans*, 122(6):4500–4517.

Ardhuin, F., Roland, A., Dumas, F., Bennis, A.-C., Sentchev, A., Forget, P., Wolf, J., Girard, F., Osuna, P., and Benoit, M. (2012). Numerical Wave Modeling in Conditions with Strong Currents: Dissipation, Refraction, and Relative Wind. *Journal of Physical Oceanography*, 42(12):2101–2120.

Ardhuin, F., Stopa, J. E., Chapron, B., Collard, F., Husson, R., Jensen, R. E., Johannessen, J., Mouche, A., Passaro, M., Quartly, G. D., Swail, V., and Young, I. (2019). Observing sea states. *Frontiers in Marine Science*, 6.

Banner, M. L. and Peirson, W. L. (2007). Wave breaking onset and strength for two-dimensional deep-water wave groups. *Journal of Fluid Mechanics*, 585:93–115.

Bretherton, F. (1969). Wavetrains in inhomogeneous moving media. *Proceedings of the Royal Society A: Mathematical, Physical and Engineering Sciences*, 302:529–554.

Bôas, A. B. V., Marechal, G., and Bohé, A. (2025). Observing Interactions Between Waves, Winds, and Currents from SWOT. *Geophysical Research Letters*, 52.

Chelton, D. B., deSzoeke, R. A., Schlax, M. G., El Naggar, K., and Siwertz, N. (1998). Geographical Variability of the First Baroclinic Rossby Radius of Deformation. *Journal of Physical Oceanography*, 28(3):433–460.

Coastal Data Information Program, S. (2013). Directional wave measurements, sea surface temperatures, and additional ocean surface parameters recorded by the Scripps Institution of Oceanography's Coastal Data Information Program network of Datawell Waverider buoys since September 1991.

Collins, C. O., Dickhudt, P., Thomson, J., de Paolo, T., Otero, M., Merrifield, S., Terrill, E., Schonau, M., Braasch, L., Paluszkiewicz, T., and Centurioni, L. (2024). Performance of moored gps wave buoys. *Coastal Engineering Journal*, 66:17–43.

D'Asaro, E. (1985). The Energy Flux from the Wind to Near-Inertial Motions in the Surface Mixed Layer. *Journal of Physical Oceanography*, 15:1043–1059.

D'Asaro, E. (2015). Surface wave measurements from subsurface floats. *Journal of Atmospheric and Oceanic Technology*, 32:816–827.

D'Asaro, E. A. (1989). The decay of wind-forced mixed layer inertial oscillations due to the effect. *Journal of Geophysical Research: Oceans*, 94(C2):2045–2056.

D'Asaro, E. A. (2003). Performance of autonomous lagrangian floats. *Journal of Atmospheric and Oceanic Technology*, 20:896–911.

D'Asaro, E. A., Thomson, J., Shcherbina, A. Y., Harcourt, R. R., Cronin, M. F., Hemer, M. A., and Fox-Kemper, B. (2014). Quantifying upper ocean turbulence driven by surface waves. *Geophysical Research Letters*, 41:102–107.

Davis, J. R., Thomson, J., Houghton, I. A., Doyle, J. D., Komaromi, W. A., Fairall, C. W., Thompson, E. J., and Moskaitis, J. R. (2023). Saturation of Ocean Surface Wave Slopes Observed During Hurricanes. *Geophysical Research Letters*, 50(16).

Drennan, W. M., Graber, H. C., Hauser, D., and Quentin, C. (2003). On the wave age dependence of wind stress over pure wind seas. *Journal of Geophysical Research: Oceans*, 108(C3):2000JC000715.

Etienne, H., Ubelmann, C., Ardhuin, F., and Dibarboure, G. (2025). Temporal and spatial scales of Near-Intertial Oscillations inferred from surface drifters. *EGUsphere*, 2025:1–16.

Ewing, J. and Laing, A. K. (1987). Directional Spectra of Seas near Full Development. *Journal of Physical Oceanography*, 17:1696–1706.

Feddersen, F., Amador, A., Pick, K., Vizuet, A., Quinn, K., Wolfinger, E., MacMahan, J. H., and Fincham, A. (2024). The wavedrifter: a low-cost imu-based lagrangian drifter to observe steepening and overturning of surface gravity waves and the transition to turbulence. *Coastal Engineering Journal*, 66(1):44–57.

Flexas, M. M., Thompson, A. F., Torres, H. S., Klein, P., Farrar, J. T., Zhang, H., and Menemenlis, D. (2019). Global Estimates of the Energy Transfer From the Wind to the Ocean, With Emphasis on Near-Inertial Oscillations. *Journal of Geophysical Research: Oceans*, 124(8):5723–5746.

Frye, D. E., Pond, S., and Elliott, W. P. (1972). Note on the Kinetic Energy Spectrum of Coastal Winds. *Monthly Weather Review*, 100(9):671–673.

Gemmrich, J. and Garrett, C. (2012). The signature of inertial and tidal currents in offshore wave records. *Journal of Physical Oceanography*, 42(6):1051–1056.

Gill, A. (1984). On the Behavior of Internal Waves in the Wakes of Storms. *Journal of Physical Oceanography*, 14:1129–1151.

Gill, A. E. (1982). *Atmosphere-Ocean Interactions.* Academic Press, San Diego, CA.

Girton, J., Whalen, C., Ren-Chieh, L., and Kunze, E. (2024). Coherent Float Arrays for Near-Inertial Wave Studies. *Oceanograhy*, 37(4):58–67.

Gold, E. (1908). *Barometric gradient and wind force. Report ot the director of the Meteorological Office on the calculation of wind velocity from pressure distribution and on the variation of meteorolgical elements with altitude.* Number 44 p. in [Gt. Brit.] M[eteorological] o[ffice. Official publication]no. 190. Printed for H. M. Stationery Off., by Darling & Son ltd., London.

Grare, L., Statom, N. M., Pizzo, N., and Lenain, L. (2021). Instrumented wave gliders for air-sea interaction and upper ocean research. *Frontiers in Marine Science*, 8.

Grigorieva, V. G., Badulin, S. I., and Gulev, S. K. (2022). Global validation of swim/cfosat wind waves against voluntary observing ship data. *Earth and Space Science*, 9.

Halsne, T., Benetazzo, A., Barbariol, F., Christensen, K. H., Carrasco, A., and Breivik, (2024). Wave Modulation in a Strong Tidal Current and Its Impact on Extreme Waves. *Journal of Physical Oceanography*, 54(1):131–151.

Hauser, D., Tison, C., Amiot, T., Delaye, L., Corcoral, N., and Castillan, P. (2017). Swim: the first spaceborne wave scatterometer. *IEEE Transactions on Geoscience and Remote Sensing*, in press.

Hayne, G. (1980). Radar altimeter mean return waveforms from near-normal-incidence ocean surface scattering. *IEEE Transactions on Antennas and Propagation*, 28(5):687–692.

Hegermiller, C. A., Warner, J. C., Olabarrieta, M., and Sherwood, C. R. (2019). Wave–current interaction between hurricane matthew wave fields and the gulf stream. *Journal of Physical Oceanography*, 49(11):2883–2900.

Herbers, T. H., Jessen, P. F., Janssen, T. T., Colbert, D. B., and MacMahan, J. H. (2012). Observing ocean surface waves with gps-tracked buoys. *Journal of Atmospheric and Oceanic Technology*, 29:944–959.

Herman, A., Dragan-Górska, A., and Markuszewski, P. (2026). Close Relationship Between Whitecapping-Related Wave Energy Dissipation and Ambient Sound in the Open Ocean. *Geophysical Research Letters*, 53(1):e2025GL120342.

Hersbach, H., Bell, B., Berrisford, P., Biavati, G., Horanyi, A., Sabater, J. M., Nicolas, J., Peubey, C., Radu, R., Rozum, I., Schepers, D., Simmons, A., Soci, C., Dee, D., and Thepaut, J.-N. (2023). Era5 hourly data on signle levels from 1940 to present. *Copernicus Climate Change Service (CS3) Climate Data Store (CDS)*.

Ho, A., Merrifield, S., and Pizzo, N. (2023). Wave–Tide Interaction for a Strongly Modulated Wave Field. *Journal of Physical Oceanography*, 53(3):915–927.

Holthuijsen, L. H. (2007). *Waves in Oceanic and Coastal Waters*. Cambridge University Press, Cambridge.

Hsu, J.-Y. (2021). Observing surface wave directional spectra under typhoon megi (2010) using subsurface em-apex floats. *Journal of Atmospheric and Oceanic Technology*, 38:1949–1966.

Huyer, A. (1977). Seasonal variation in temperature, salinity, and density over the continental shelf off oregon. *Limnology and Oceanography*, 22(3):442–453.

Iyer, S., Thomson, J., Thompson, E., and Drushka, K. (2022). Variations in Wave Slope and Momentum Flux From Wave-Current Interactions in the Tropical Trade Winds. *Journal of Geophysical Research: Oceans*, 127(3).

Janssen, P. A. (1989). Wave-Induced Stress and the Drag of Air Flow over Sea Waves. *Journal of Physical Oceanography*, 19:745–754.

Kim, S. Y. and Kosro, P. M. (2013). Observations of near-inertial surface currents off Oregon: Decorrelation time and length scales: Scales of Near-Inertial Surface Currents. *Journal of Geophysical Research: Oceans*, 118(7):3723–3736.

Kundu, P. K. and Cohen, I. M. (2008). *Fluid mechanics*. Academic Press, Amsterdam ; Boston, 4th ed edition.

Large, W. and Pond, S. (1981). Open Ocean Momentum Flux Measurements in Moderate to Strong Winds. *Journal of Physical Oceanography*, 11:324–336.

Li, Q., Reichl, B. G., Fox-Kemper, B., Adcroft, A. J., Belcher, S. E., Danabasoglu, G., Grant, A. L., Griffies, S. M., Hallberg, R., Hara, T., Harcourt, R. R., Kukulka, T., Large, W. G., McWilliams, J. C., Pearson, B., Sullivan, P. P., Roekel, L. V., Wang, P., and Zheng, Z. (2019). Comparing ocean surface boundary vertical mixing schemes including langmuir turbulence. *Journal of Advances in Modeling Earth Systems*, 11:3545–3592.

Liu, G., Perrie, W., and Hughes, C. (2017). Surface wave effects on the wind-power input to mixed layer near-inertial motions. *Journal of Physical Oceanography*, 47(5):1077–1093.

Longuet-Higgins, M., Cartwright, D., and Smith, N. (1963). Observations of the directional spectrum of sea waves using the motions of a floating buoy. *Proc. Conf. Ocean Wave Spectra*, pages 111–132.

Longuet-Higgins, M. S. and Stewart, R. W. (1964). Radiation stresses in water waves; a physical discussion, with applications. *Deep-Sea Research*, 11:529–562.

Ma, B., D'asaro, E., Sanford, T., and Thomson, J. (2020). Lc-dri field experiment and data calibration report.

Marechal, G. and Ardhuin, F. (2021). Surface currents and significant wave height gradients: Matching numerical models and high-resolution altimeter wave heights in the agulhas current region. *Journal of Geophysical Research: Oceans*, 126.

Marechal, G. and De Marez, C. (2022). Variability of surface gravity wave field over a realistic cyclonic eddy. *Ocean Science*, 18(5):1275–1292.

McWilliams, J. C. and Fox-Kemper, B. (2013). Oceanic wave-balanced surface fronts and filaments. *Journal of Fluid Mechanics*, 730:464–490.

Mcwilliams, J. C. and Restrepo, J. M. (1999). The Wave-Driven Ocean Circulation. *Journal of Physical Oceanography*, 29:2523–2540.

Melville, W. K. (1996). The role of surface-wave breaking in air-sea interaction.

Middleton, J. F. (1985). Drifter spectra and diffusivities. *Journal of Marine Research*, 43:37–55.

Munk, W. H. (1944). Proposed uniform procedure for observing waves and interpreting instrument records.

NOAA PMEL, Cronin, M., Anderson, N., Zhang, D., Berk, P., Wills, S., Serra, Y., Kohlman, C., Sutton, A., Honda, M., Kawai, Y., Yang, J., Thomson, J., Lawrence-Slavas, N., Eyre, J., and Meinig, C. (2023). PMEL Ocean Climate Stations as Reference Time Series and Research Aggregate Devices. *Oceanography*.

Olbers, D. and Eden, C. (2016). Revisiting the generation of internal waves by resonant interaction with surface waves. *Journal of Physical Oceanography*, 46:2335–2350.

O'Reilly, W. C., Olfe, C. B., Thomas, J., Seymour, R. J., and Guza, R. T. (2016). The california coastal wave monitoring and prediction system. *Coastal Engineering*, 116:118–132.

Papandreou, A., Ginis, I., and Hara, T. (2026). Impact of Ocean Currents on Surface Waves Generated by Tropical Cyclone. *Journal of Physical Oceanography*, 56(2):355–369.

Phillips, O. M. (1966). *The Dynamics of the Upper Ocean.* Cambridge University Press.

Phillips, O. M. (1985). Spectral and statistical properties of the equilibrium range in wind-generated gravity waves. *Journal of Fluid Mechanics*, 156:505–531.

Pollard, R. (1970). On the generation by winds of inertial waves in the ocean. *Deep Sea Research and Oceanographic Abstracts*, 17(4):795–812.

Pollard, R. and Millard, R. (1970). Comparison between observed and simulated wind-generated inertial oscillations. *Deep Sea Research and Oceanographic Abstracts*, 17(4):813–821.

Pollard, R. and Thomas, K. (1989). Vertical Circulation Revealed by Diurnal Heating of the Upper Ocean in Late Winter. Part I: Observations. *Journal of Physical Oceanography*, 19.

Polton, J. A. and Belcher, S. E. (2007). Langmuir turbulence and deeply penetrating jets in an unstratified mixed layer. *Journal of Geophysical Research: Oceans*, 112(9).

Program, N. I. S. C. and Center, N. N. D. B. (2015). Near-real-time surface ocean velocities derived from HF-radar stations located along coastal waters of North Slope Alaska, Gulf of Alaska, Puerto Rico/Virgin Islands, eastern U.S./Gulf of America, Hawaii, Great Lakes, and western U.S..

Quilfen, Y. and Chapron, B. (2019). Ocean Surface Wave-Current Signatures From Satellite Altimeter Measurements. *Geophysical Research Letters*, 46(1):253–261.

Rascle, N., Ardhuin, F., Queffeulou, P., and Croizé-Fillon, D. (2008). A global wave parameter database for geophysical applications. Part 1: Wave-current–turbulence interaction parameters for the open ocean based on traditional parameterizations. *Ocean Modelling*, 25(3-4):154–171.

Sanford, T. B., Drever, R. G., and Dunlap, J. H. (1978). A velocity profiler based on the principles of geomagnetic induction. *Deep-Sea Research*, 25:183–210.

Sanford, T. B., Dunlap, J. H., Carlson, J. A., Webb, D. C., and Girton', J. B. (2005). Autonomous velocity and density profiler: Em-apex. *Proceedings of the IEEE Working Conference on Current Measurement Technology*, pages 152–156.

Sanford, T. B., Price, J. F., and Girton, J. B. (2011). Upper-ocean response to hurricane frances (2004) observed by profiling em-apex floats. *Journal of Physical Oceanography*, 41:1041–1056.

Sanford, T. B., Price, J. F., Girton, J. B., and Webb, D. C. (2007). Highly resolved observations and simulations of the ocean response to a hurricane. *Geophysical Research Letters*, 34.

Smeltzer, B. K., Æsoy, E., and Ellingsen, S. A. (2019). Observation of surface wave patterns modified by sub-surface shear currents. *Journal of Fluid Mechanics*, 873:508–530.

Stadler, J., Girton, J., and Ma, B. (2025). Validation of Surface Wave Spectral Measurements from Velocity Profiling Floats. *Journal of Atmospheric and Oceanic Technology*, 42(5):449–462.

Sullivan, P. P. and McWilliams, J. C. (2010). Dynamics of winds and currents coupled to surface waves. *Annual Review of Fluid Mechanics*, 42:19–42.

Suzuki, N. and Fox-Kemper, B. (2016). Understanding Stokes forces in the wave-averaged equations. *Journal of Geophysical Research: Oceans*, 121(5):3579–3596.

Thomson, J. (2012). Wave breaking dissipation observed with "swift" drifters. *Journal of Atmospheric and Oceanic Technology*, 29:1866–1882.

Thomson, J., D'Asaro, E. A., Cronin, M. F., Rogers, W. E., Harcourt, R. R., and Shcherbina, A. (2013). Waves and the equilibrium range at Ocean Weather Station P. *Journal of Geophysical Research: Oceans*, 118(11):5951–5962.

Thomson, J., Girton, J. B., Jha, R., and Trapani, A. (2018). Measurements of directional wave spectra and wind stress from a wave glider autonomous surface vehicle. *Journal of Atmospheric and Oceanic Technology*, 35:347–363.

Thomson, J., Moulton, M., de Klerk, A., Talbert, J., Guerra, M., Kastner, S., Smith, M., Zippel, S., and Nylund, S. (2019). A new version of the swift platform for waves, currents, and turbulence in the ocean surface layer.

Van Sebille, E., Aliani, S., Law, K. L., Maximenko, N., Alsina, J. M., Bagaev, A., Bergmann, M., Chapron, B., Chubarenko, I., Cózar, A., Delandmeter, P., Egger, M., Fox-Kemper, B., Garaba, S. P., Goddijn-Murphy, L., Hardesty, B. D., Hoffman, M. J., Isobe, A., Jongedijk, C. E., Kaandorp, M. L. A., Khatmullina, L., Koelmans, A. A., Kukulka, T., Laufkötter, C., Lebreton, L., Lobelle, D., Maes, C., Martinez-Vicente, V., Morales Maqueda, M. A., Poulain-Zarcos, M., Rodríguez, E., Ryan, P. G., Shanks, A. L., Shim, W. J., Suaria, G., Thiel, M., Van Den Bremer, T. S., and Wichmann, D. (2020). The physical oceanography of the transport of floating marine debris. *Environmental Research Letters*, 15(2):023003.

Villas Boas, A. B., Cornuelle, B. D., Mazloff, M. R., Gille, S. T., and Ardhuin, F. (2020). Wave–Current Interactions at Meso- and Submesoscales: Insights from Idealized Numerical Simulations. *Journal of Physical Oceanography*, 50:3483–3500.

Villas Bôas, A. B. and Pizzo, N. (2021). The geometry, kinematics, and dynamics of the two-way coupling between wind, waves, and currents. *US CLIVAR Variations*, 19(1).

Vrećica, T., Pizzo, N., and Lenain, L. (2022). Observations of strongly modulated surface wave and wave breaking statistics at a submesoscale front. *Journal of Physical Oceanography*, 52:289–304.

Wagner, G. L., Chini, G. P., Ramadhan, A., Gallet, B., and Ferrari, R. (2021). Near-inertial waves and turbulence driven by the growth of swell. *Journal of Physical Oceanography*, 51:1337–1351.

Wang, H., Villas Bôas, A. B., Vanneste, J., and Young, W. R. (2025). Scattering of surface waves by ocean currents: the U2H map. *Journal of Fluid Mechanics*, 1005:A12.

Wang, H., Villas Bôas, A. B., Vanneste, J., and Young, W. R. (2026). The U2H Map Explains the Effect of (Sub)Mesoscale Currents on Significant Wave Height Statistics. *Journal of Physical Oceanography*, 56(5):945–955.

Wang, P. and Sheng, J. (2016). A comparative study of wave-current interactions over the eastern Canadian shelf under severe weather conditions using a coupled wave-circulation model. *Journal of Geophysical Research: Oceans*, 121(7):5252–5281.

Wang, W. and Huang, R. X. (2004). Wind Energy Input to the Surface Waves*. *Journal of Physical Oceanography*, 34(5):1276–1280.

WAVEWATCH III Development Group (2016). User manual and system documentation of wavewatch iii version 5.16. Technical report, NOAA/NWS/NCEP/MMAB Tech. Note 329.

WAVEWATCH III Development Group (2019). User manual and system documentation of wavewatch iii version 6.07. Technical Report Tech. Note 333, NOAA/NWS/NCEP/MMAB, College Park, MD, USA.

Welch, P. (1967). The use of fast Fourier transform for the estimation of power spectra: A method based on time averaging over short, modified periodograms. *IEEE Transactions on Audio and Electroacoustics*, 15(2):70–73.

Weller, R. A. and Price, J. F. (1988). Langmuir circulation within the oceanic mixed layer. *Deep Sea Research Part A. Oceanographic Research Papers*, 35(5):711–747.

Wunsch, C. (2004). Vertical Mixing, Energy, and the General Circulation of the Oceans. *Annual Review of Fluid Mechanics*, 36(1):281–314.

Young, I. (1999). *Wind Generated Ocean Waves*. Elsevier, 1st edition.

Young, I. R. (1995). The determination of confidence limits associated with estimates of the spectral peak frequency. *Ocean Engineering*, 22:669–686.

Yu, X., Ponte, A. L., Elipot, S., Menemenlis, D., Zaron, E. D., and Abernathey, R. (2019). Surface Kinetic Energy Distributions in the Global Oceans From a High-Resolution Numerical Model and Surface Drifter Observations. *Geophysical Research Letters*, 46(16):9757–9766.

Yuan, S., Yan, X., Zhang, L., Pang, C., and Hu, D. (2024). Observation of Near-Inertial Waves Induced by Typhoon Lan in the Northwestern Pacific: Characteristics, Energy Fluxes and Impact on Diapycnal Mixing. *Journal of Geophysical Research: Oceans*, 129(2):e2023JC020187.

Zeiden, K., Thomson, J., Shcherbina, A., and D'Asaro, E. (2024). Observations of Elevated Mixing and Periodic Structures Within Diurnal Warm Layers. *Journal of Geophysical Research: Oceans*, 129(11):e2024JC021399.

Zheng, Z., Harcourt, R. R., D'Asaro, E. A., and Shcherbina, A. Y. (2025). Scaling Near-Surface Observations of Turbulent Vertical Velocity in the Ocean. Part I: Surface Layer. *Journal of Physical Oceanography*, 55(10):1889–1903.